Solid State Structure-Reactivity Studies on Bixbyites, Fluorites and Perovskites Belonging to the Vanadate, Titanate and Cerate Families

By

Shahid P. Shafi

A Thesis submitted to the Faculty of Graduate Studies of

The University of Manitoba

in partial fulfilment of the requirements of the degree of

Doctor of Philosophy

Department of Chemistry

University of Manitoba

Winnipeg

Abstract

This thesis primarily focuses on the systematic understanding of structure – reactivity relationships in two representative systems: bixbyite and related structures as well as indium doped CeO_2. Topotactic reaction routes have gained significant attention over the past two decades due to their potential to access kinetically controlled metastable materials. This has contributed substantially to the understanding of solid state reaction pathways and provided first insights into mechanisms. Contrary to the widely used ex-situ methods, in – situ techniques including powder x-ray diffraction and thermogravimetric – differential thermal analysis have been employed extensively throughout this work in order to follow the reaction pathways in real time.

Detailed analysis of the AVO_3 (A = In, Sc) bixbyite reactivity under oxidative conditions has been carried out and a variety of novel metastable oxygen defect phases have been identified and characterized. The novel metastable materials have oxygen deficient fluorite structures and consequently are potential ion conductors. Structural aspects of the topotactic vs. reconstructive transformations are illustrated with this model system. The structure – reactivity study of AVO_3 phases was extended to AVO_3 perovskite family.

Based on the research methodologies and results from AVO_3 bixbyite reactivity studies a generalized mechanistic oxidation pathway has been established with a non-vanadium phase, $ScTiO_3$ bixbyite. However, there is stark contrast in terms of structural stability and features beyond this stability limit during AVO_3 and $ScTiO_3$ bixbyite

reaction pathways. A series of complex reaction sequences including phase separation and phase transitions were identified during the investigation of $ScTiO_3$ reactivity.

The two-step formation pathway for the fluorite – type oxide ion conductor $Ce_{1-x}In_xO_{2-\delta}$ ($0 \leq x \leq 0.3$) is being reported. The formation of the $BaCe_{1-x}In_xO_{3-\delta}$ perovskites and the subsequent CO_2-capture reaction with the formation of $Ce_{1-x}In_xO_{2-\delta}$ ($0 \leq x \leq 0.3$) has been investigated in detail. The two-step formation pathway is contrasted with the unsuccessful direct method. The stability and the extent of In – doping for the CeO_2 fluorite phases that can be achieved through this CO_2 – capture method are reported. The necessity and strategies for the selection of appropriate intermediate precursors for the preparation of doped CeO_2 are also reported.

Acknowledgements

I would like to thank foremost my supervisor Prof. Mario Bieringer for his guidance, support, encouragement and the enormous amount of time and effort provided throughout my Ph. D. program.

Thanks to my advisory committee members Prof. Peter Budzelaar, Prof. Frank Hawthorne, Prof. Sean Cadogan and Prof. Georg Schreckenbach for their constructive inputs.

I would like to express my gratitude to Lachlan M. D. Cranswick for the powder neutron diffraction data collection on many of my samples. Thanks to Ron Donaberger at NRC, Chalk River and Thomas Hansen at the ILL, Grenoble.

I would like to thank Prof. Miguel Alario-Franco and Dr. Elizabeth Castillo-Martinez for the collaboration during a high pressure project. Thanks to Prof. Venkataraman Thangadurai and his group for conductivity measurements and assistance during a collaborative project. I would like to thank Prof. Holger Kleinke and Jackie Xu for the synthesis of some of my precursor samples.

I would like to acknowledge Prof. Scott Kroeker, Dr. Vladimir K. Michaelis and John E. C. Wren for solid state NMR measurements as well as Prof. Johan van Lierop and Ryan Desautels for access to and assistance with the SQUID magnetometer.

Thanks to the past and present members of the Bieringer research group: Matt Kotyk, Mitch Hancock, Jiasheng Lu, Brad Hernden, Ela Tabaku and Joey Lussier.

I am extremely thankful to the generous funding I have received including the University of Manitoba Graduate Fellowship, Faculty of Science Scholarship, International Graduate Student Entrance Scholarship, Department of Chemistry awards (Ernst and Ingrid Bock, Walter and Elizabeth Rodewald, Anderson, Centennial, Betts etc.) and various travel support received from the Department of Chemistry, Faculty of Graduate Studies, Faculty of Science, Graduate Students Association and Chemistry Graduate Students Association.

Last but not least, my sincere thanks to my parents, brother, my wife Hima, all the other family members and friends for their unconditional love and support.

Table of Contents

List of Tables

List of Figures

Chapter 1: Introduction – Part I

Background Literature & Focus of the Project

1.1. The Importance of Solid State Materials

Materials have always played a vital role in the evolution of civilizations. About two million years ago during the Stone Age, useful materials (stones) were selected and shaped as tools. During the Bronze Age, materials were modified by workable metals and alloying metals thus the fundamental properties of the materials were improved. Most of those modifications were likely based on experience and followed empirical concepts. This was followed by the Iron Age which greatly facilitated better opportunities for trade and communications with the common use of coins.[1] Modern materials science is an applied science concerned with the interplay between structure, properties, processing and performance of materials. The primary concept is to understand the materials' structure at the atomic level and relate this to their properties. Such an understanding allows tailoring novel materials with appropriate changes to the structure. Over the years, different types of materials such as ceramic, molecular and polymer materials gained significant attention due to their potential applications. There has always been strong interconnection between the topics of interest in materials science and the global needs. The recent topics of interest in materials science include ionic, magnetic, semiconducting and optical properties. These materials directly address energy demands and waste recovery. Modern materials science has a large impact on our daily life. Materials science covers a wide range of applications observed in our daily life such as mechanical (abrasives, alloys, piezoelectrics), environmental (gas sensors, catalysts), wireless

communication (microwave dielectrics), data storage (hard drives) and energy (batteries, solid oxide fuel cells, thermoelectrics, photocatalysts, solar cells). The progress of materials science is significant to many industrial sectors including electronic, telecommunications, aerospace, automotive and energy. For example, the continued miniaturization of components in computers, cell phones and televisions is enabled by the advance in semiconducting and magnetic materials.

According to a recent report from the U.S. Department of Energy (DOE), the global energy demand is expected to double by 2050.[2] The conventional and primary resources for energy are non-renewable fossil fuels.[3] The excessive use of fossil fuels is concerning because of the associated CO_2 emissions and the expected climate changes. The finite availability of fossil fuels and the threatening global warming has called for clean and sustainable alternative energy resources. Thermoelectrics,[4,5] batteries, photovoltaics and fuel cells can be used for waste energy recovery, energy conversion and energy storage. These approaches are advantageous due to their ability to make use of the energy which might be wasted otherwise such as heat in thermoelectrics and sunlight in photovoltaics. The field of energy storage materials is still evolving. In order to develop more efficient materials for the conversion and storage of energy, advances in materials processing and a deeper understanding of their fundamental functions are required. Consequently good model systems capable of mimicking those materials need to be explored during the first stage and the gained understanding can be applied to more complex materials at a later stage.

Solid state materials science is a vibrant area of research with a continuous search for novel materials with technological applications. This requires a comprehensive

understanding of the interplay between synthetic methods, structures, properties and materials' performance. Such an understanding would prominently enhance the ability to tailor materials with desired applications. On many occasions, the properties of a material arise as a response to external stimuli including magnetic fields and electric fields. The properties are strongly correlated with its composition and structure. Consequently, a good understanding of structure and composition can lead to the design of better materials.

1.2. Transition Metal Oxides

The large structural diversity of transition metal oxides lends itself to systematic structure – property studies. In particular the valence *d* electrons and the wide variety of accessible oxidation states permit the physical properties to be controlled by means of redox processes. The diverse properties and phenomena exhibited by transition metal oxides are covered extensively in the literature.[6-8] Transition metal oxides are widely used and have seen very significant performance increases in applications such as heterogeneous catalysis[9,10] for pollution abatement, colossal magnetoresistance for data storage devices and ion conduction for fuel cells.[11] Continued development of these materials requires the systematic understanding of structure – property relationships. Investigation of structure – property relationships using simple model systems is very relevant.

Extended solids with simple compositions such as ABO_3 can result in complex structural changes due to doping. Consider substitution of the A^{2+} cation in a hypothetical model system $A^{2+}B^{4+}O_3$ (B = transition metal) with small amounts of $(A')^{3+}$ cations

which is of similar size. A variety of simple structural changes can be expected after successful doping including an increase in the oxygen stoichiometry for charge balancing or reduction of required amounts of B^{4+} so as to maintain the oxygen stoichiometry and more complicated charge ordering and orbital ordering. Each of these changes to the structure influences the physical properties differently. Comprehensive understanding of structure – property relationships gets more difficult with the increase in compositional complexity. The investigation of the interplay between structure, reactivity and properties using simple structural models benefits from the lack of such compositional complexities.

1.3. Solid State Synthesis Methods and Metastable Phases

The structure of materials is strongly correlated with the synthesis route applied. A large variety of synthetic methods including high temperature ceramic method, topochemical reactions, ion exchange method, electrochemical method, high pressure method, sol-gel method and *chimie douce* or soft chemistry method are employed for making solid state materials.[8] Conventional solid state synthesis relies on the ceramic method where thoroughly ground mixtures of oxide, carbonate or oxalate powders are treated at high temperatures often resulting in thermodynamically controlled products.

Molecular chemists have developed well-established reaction mechanisms over the years by virtue of kinetic control during the synthesis which allows them to synthesize intricate structures through step wise transformation of the precursors. The primary reasons for this are twofold: firstly the reactions are carried out in solution so there is no diffusion barrier, secondly the reactions are controlled by the functional groups and the bonding in the rest of the molecule is intact.[12] Contrary to molecular

science, the mechanisms in solid state reactions are not well understood. Synthesis of solid state materials can be achieved through a rational approach through already established structure-reactivity relationships; however there is always a possibility for surprise. An interesting example for the rational synthesis is the fast Na^+ ion conductor $Na_3Zr_2PSi_2O_{12}$ prepared by Goodenough et al.[8,13] They approached the synthesis on the basis of the anticipated cation preferences and nature of the oxide network formed. Because of the lack of mechanistic details solid state reactions are often guided by experience and intuition.

A better understanding of solid state reaction mechanisms could allow the rational design of novel exotic materials. The first step towards this goal is to monitor reaction pathways and explore reactivity trends. Currently, the trend is to remain aloof from the brute force method so as to access the kinetically controlled metastable compositions and structures which otherwise are difficult to prepare. Metastable phases have higher free energies than the corresponding thermodynamically stable phase analogues. When a solid is synthesized (e.g., by quenching a melt, crystallizing from a solution), there are numerous thermodynamically allowed pathways available for structure evolution including the one corresponding to the most stable structure.[14] During kinetically controlled structural evolution, the correlation between atomic positions and motions is small. Consequently, when the parent system is far from equilibrium, nucleation of a metastable phase is favored.[14] Metastable materials include a variety of compounds including inorganic/organic nanocomposites, high-*Tc* cuprates, pillared layered materials and zeolites.[14] The mechanistic approach for solid state synthesis is limited to the low temperature regime. One of the early attempts to overcome the diffusion barrier was by

thin film deposition of the solid reactants and heating at low temperatures.[14-17] The topochemical method is a promising route to synthesize metastable phases and is very relevant to the focus of this thesis.

1.3.1. Topochemical Reaction Routes

Solid state structural transformations can be classified as reconstructive or topotactic. During a reconstructive process, ions are required to migrate to different sites and consequently the lattice topology is drastically changed. During topochemical/topotactic reactions, significant atomic connectivity of the reactant is retained in the final product. The topology of the ions are conserved during topochemical reactions as there is only very little ion migration in the lattice. This fact was recognized long ago,[18-20] and has gained significant attention since then due to the potential for synthesizing a wide variety of metastable materials. The two primary topotactic methods are redox soft chemistry involving intercalation and deintercalation and acido-basic processes. The early intercalation chemistry was primarily focused on graphite intercalation compounds[21] including the intercalation of strongly electropositive metals such as alkali and alkaline earth metals between the carbon sheets of graphite.[22] This was followed by molecular intercalates of layered silicates and intercalation of molecular and ionic entities into layered dichalcogenides.[23,24] In 1978, the potential application of layered chalcogenides as cathode materials provided a boost to the development of this field[25] and the method is currently covering a wide range of materials including layered perovskites, zeolites and transition metal phosphates.

A recent review by Wiley and coworkers extensively covered the topochemical reaction strategies employed for the perovskite family as a model system.[26] The reaction methods used in topochemical manipulations include insertion, deinsertion and substitution. A typical example for the topochemical substitution method is ion exchange. The ion exchange reaction between $Tl_2Ti_4O_9$ and AgCl results in $Ag_2Ti_4O_9$ and TlCl through a monovalent cation substitution[26,27] as shown in Eq. 1.l. The intercalation method involves insertion of cationic, anionic (redox process) or neutral species into the host lattice. Fluorination of $LaSrMnO_4$ as shown in Eq. 1.2, is an example of a staged insertion reaction.[26,28] During deintercalation, cations or anions are removed from the parent structure by chemical or electrochemical methods.[26,29,30] $Li_{1-x}CoO_2$ can be prepared by the electrochemical extraction of lithium from $LiCoO_2$ (Eq. 1.3).[26] Deintercalation of oxide anions from $CaMnO_3$ results in the formation of $CaMnO_{2.5}$ (Eq. 1.4) with ordered oxygen vacancies.[26,31]

$Tl_2Ti_4O_9 + 2AgCl \rightarrow Ag_2Ti_4O_9 + 2TlCl$ (Ion Exchange Method) (Eq. 1.1)

$LaSrMnO_4 + ½\ F_2 \rightarrow LaSrMnO_4F$ (Oxidative insertion) (Eq. 1.2)

$LiCoO_2 \rightarrow Li_{1-x}CoO_2 + x\text{Li}.$ (Oxidative deinsertion) (Eq. 1.3)

$CaMnO_3 + ½\ H_2 \rightarrow CaMnO_{2.5} + ½\ H_2O$ (Reductive deinsertion) (Eq. 1.4)

Two examples involving layer extraction and reductive deinsertion are discussed below. Gönen and coworkers demonstrated the reversible cation/anion extraction from the Ruddlesden-Popper (R-P) phase $K_2La_2Ti_3O_{10}$ resulting in the formation of $KLa_2Ti_3O_{9.5}$ and $La_2Ti_3O_9$.[32] The Ruddlesden-Popper phase which has a general formula $A_2[A'_{n-1}B_nO_{3n+1}]$ is a layered perovskite and has the ability to undergo ion exchange,

intercalation and pillaring reactions.[32] Reacting $K_2La_2Ti_3O_{10}$ with tetraphenyl phosphonium bromide (PPh_4Br) or tetrabutyl phosphonium bromide (PBu_4Br) permits the topochemical extraction of potassium oxide from the parent structure. The amount of phosphonium salt can be controlled such that one equivalent $KO_{0.5}$ or two equivalents of $KO_{0.5}$ can be removed from the host structure forming $KLa_2Ti_3O_{9.5}$ and $La_2Ti_3O_9$ respectively[32] as shown in Eq. 1.5 and 1.6.[26]

$$K_2La_2Ti_3O_{10} + PPh_4Br \rightarrow KLa_2Ti_3O_{9.5} + KBr + \tfrac{1}{2}\, PPh_3O + \tfrac{1}{2}\, PPh_3 + \tfrac{1}{2}\, Ph_2 \qquad \text{(Eq. 1.5)}$$

$$K_2La_2Ti_3O_{10} + 2PPh_4Br \rightarrow La_2Ti_3O_9 + 2KBr + PPh_3O + PPh_3 + Ph_2 \qquad \text{(Eq. 1.6)}$$

The structural variations during the reaction pathway are shown in figure 1.1. In the host Ruddlesden – Popper phase $K_2La_2Ti_3O_{10}$, the neighboring perovskite layers are arranged in a staggered fashion. Removal of one equivalent of $KO_{0.5}$ results in the formation of $KLa_2Ti_3O_{9.5}$ Dion – Jacobson (D-J) phase which has the general formula $A[A'_{n-1}B_nO_{3n+1}]$. Note that during this structural transformation, perovskite layers readjust as the adjacent perovskite layers in the D – J phase (figure 1.1) are not staggered as in the parent R – P structure. Removal of second equivalent of $KO_{0.5}$ resulting in the formation of $La_2Ti_3O_9$ is accompanied by the arrangement of perovskite layers reverting back to the staggered orientation.[26,32]

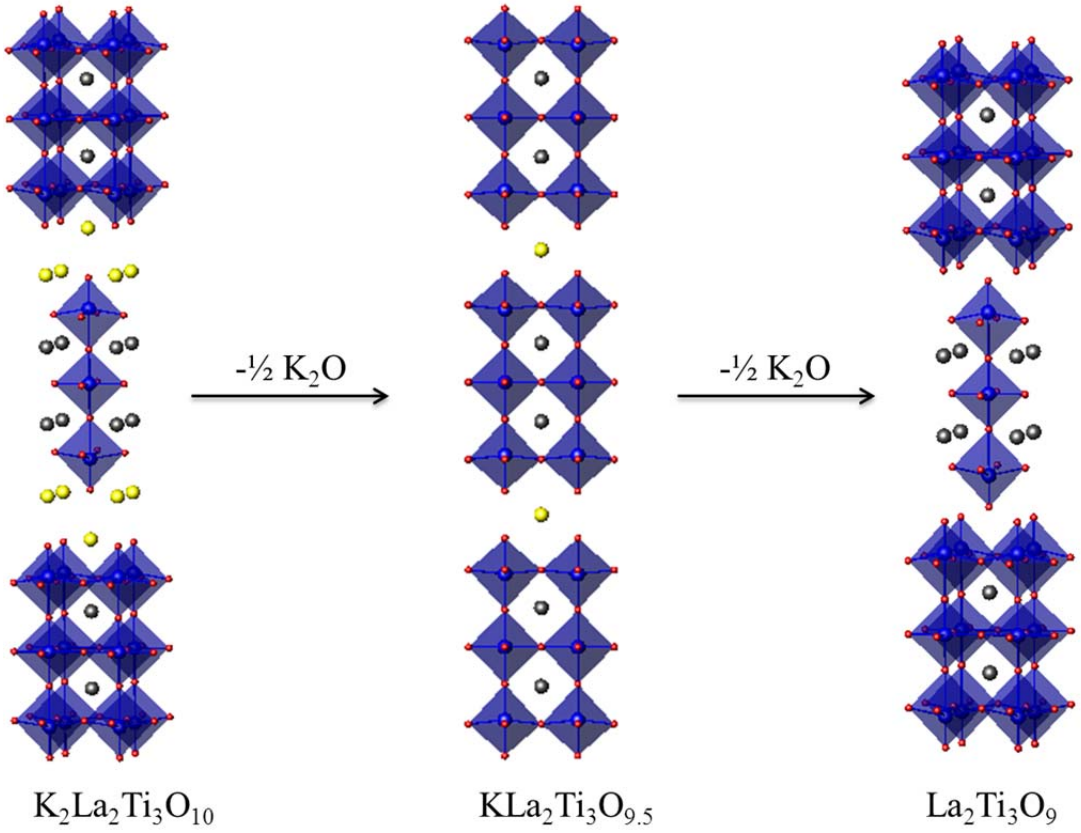

Figure 1.1. Structural changes during the cation/anion extraction from $K_2La_2Ti_3O_{12}$ with PPh_4Br or PBu_4Br. K – yellow spheres, La – gray spheres, TiO_6 – blue octahedral and O – red spheres.[26]

Over the years reductive deintercalation methods have been employed for oxygen removal from a variety of metal oxides.[26] Initially, topochemical reductive deintercalation for oxygen removal was carried out using reducing agents such as dilute hydrogen or ammonia.[26,33,34] A more recent approach to oxygen deintercalation is the use of solid reductants such as CaH_2 and NaH originally developed by Hayward and coworkers.[35] A significant advantage of these solid hydride reductants is the feasibility for hydride ion insertion.[36]

The structural changes during the reduction of $SrFeO_3$ by CaH_2 were reported by Tsujimoto and coworkers in 2007.[37] The structural changes occurring during this reaction are shown in figure 1.2. The reduction of perovskite $SrFeO_3$ to $SrFeO_2$ proceeds through a brownmillerite – type intermediate $SrFeO_{2.5}$. During the reaction pathway oxide layers are removed by the reductant CaH_2. The common coordination environments adopted by Fe in metal oxides are octahedral and tetrahedral.[38] The $SrFeO_2$ structure has high spin Fe^{2+} ions exhibiting square – planar coordination and the structure is analogous to infinite layer cupric oxides.[37]

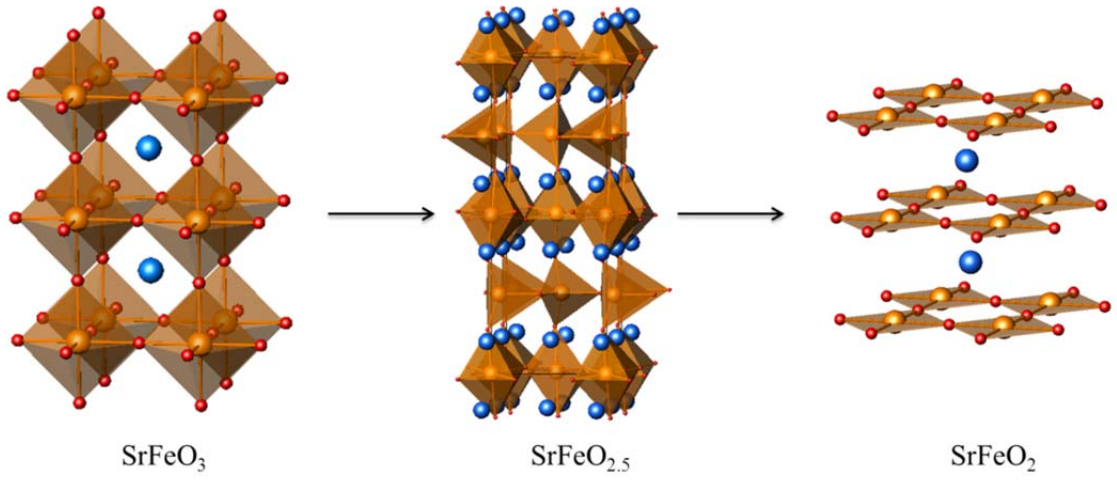

Figure 1.2. Oxygen deintercalation of $SrFeO_3$ resulting in the formation of $SrFeO_{2.5}$ brownmillerite and $SrFeO_2$ with square planar Fe layers. Blue spheres – Sr, Orange polyhedral – Fe coordination environment, Red – Oxygen.

The prime focus of this project is to study the structure – reactivity relationship using model systems. A variety of novel metastable oxygen defect phases have been prepared and characterized during the course of various projects. In-situ techniques were employed for the study as ex-situ methods often would not allow for a complete

understanding of the reaction pathways since significant intermediates could be overlooked due to poorly chosen reaction conditions. The following section provides a brief overview of the relevant structures used during this project.

1.4. AVO_4 (A = RE, Sc, In) Vanadate Structures

Vanadium oxide based materials cover a wide range of crystallographic structures owing to the multiple oxidation states of vanadium thereby assisting the systematic investigation of interplay between structure and reactivity. The primary focus of this thesis is to understand vanadate redox chemistry for composition AVO_x (x = 3, 3.5 and 4) where the A cation is trivalent. Note that the A cations chosen for this study are diamagnetic and therefore vanadium is the only paramagnetic cation in the oxidation states V^{3+} (d^2 ions, $S = 1$) and V^{4+} (d^1 ions, $S = ½$).

Though the discovery of AVO_4 rare earth orthovanadates dates back to the early 1950s, there has been a recent renaissance of these materials due to their potential for photocatalytic water splitting. In addition to this, AVO_4 (A = Rare Earth or RE-like) compounds have been investigated for their magnetic, luminescent and electronic properties.[39,40] These materials are also found to have applications such as waste disposal materials[41] and x-ray as well as γ-ray scintillators for medical imaging.[42] The catalytic properties of rare earth orthovanadates cover a wide range of applications including oxidative dehydrogenation of propane,[43] methanol oxidation,[44] formaldehyde decomposition[45] and photocatalytic water splitting.[46] As mentioned briefly in the introduction, alternative renewable energy resources are required to overcome the current threatening energy and environmental issues. The photocatalytic water splitting method

resulting in the production of hydrogen gas which can be utilized as a storable energy source is gaining significant attention. There are only very few reports in the literature on defect zircon structures such as $RE_{0.9}CrO_{3.85}$ (RE = Gd, Yb, Y).[47] This defect zircon structure has simultaneous A-cation and anion deficiencies, consequently there is no change in the B – cation oxidation state.

AVO_4 orthovanadates crystallize in the zircon-type structure with the space group $I4_1/amd$.[48] The zircon structure shown in figure 1.3 consists of VO_4 tetrahedra and AO_8 bisdisphenoids. Alternating edge-sharing VO_4 and MO_8 fragments form extended structures parallel to the *c* axis and are connected perpendicularly by edge-sharing MO_8 units. MO_8 bisdisphenoids are connected in a zigzag fashion parallel to the *a* axis. The unit cell volumes of the AVO_4 phases scale with the size of A^{3+} cations and a systematic decrease in the V-O distance with increasing A^{3+} cation size is observed.[48] The zircon-type vanadates are found to transform to denser scheelite structures under a few kilobars pressures and temperatures below 600 °C, consequently they are used as model systems for the investigation of polymorphism among ABO_4-type compounds.[48]

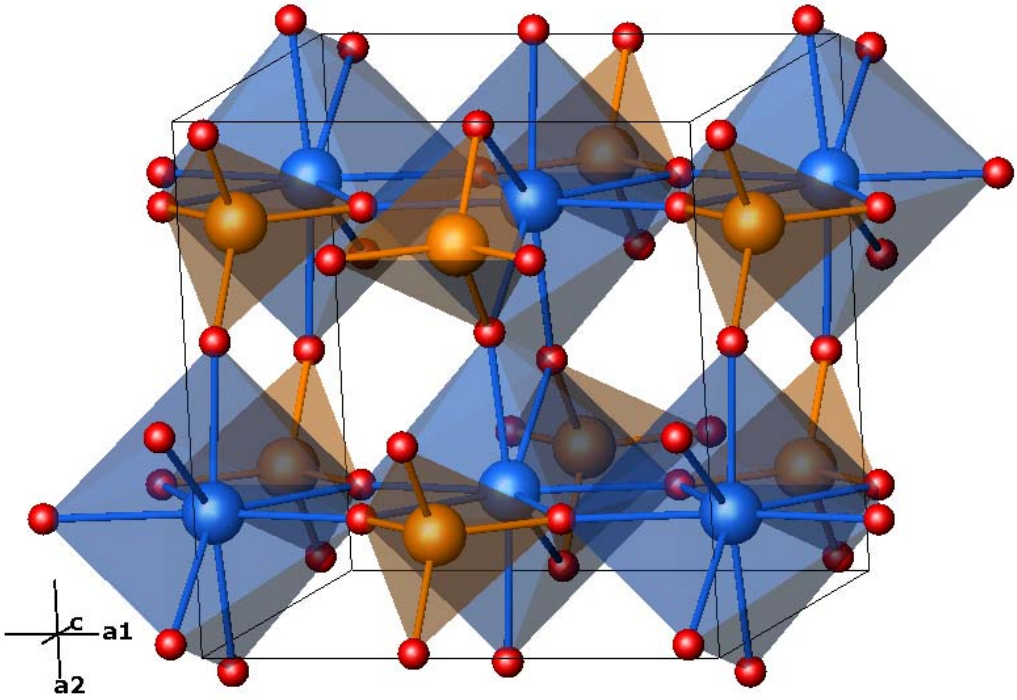

Figure 1.3. AVO_4 zircon structure with AO_8 bisdisphenoids (blue) and VO_4 tetrahedra (orange). Oxygen atoms are shown as red spheres.

The two primary compositions relevant to this thesis are $ScVO_4$ and $InVO_4$. $ScVO_4$ crystallizes in the zircon type structure discussed above. The two most common phases of $InVO_4$ are the high temperature orthorhombic (*Cmcm*, space group #63) structure and low temperature monoclinic (*C12/m1*, space group #12) form. Both phases have open structures which can facilitate lithium ion intercalation.[49] The structure used in this project is the orthorhombic $InVO_4$ phase which comprises chains of InO_6 octahedra linked together by VO_4 tetrahedra[50] as shown in figure 1.4. In monoclinic $InVO_4$ there are In_4O_{16} groups formed by four edge-sharing InO_6 octahedra linked to each other by VO_4 tetrahedra.[51] Due to high lithium ion intercalation capacity and good cyclability $InVO_4$ is a potential candidate for anode materials in lithium ion secondary batteries.[52] Another

important application of the $InVO_4$ phase is in photocatalysis. Decomposition of water which is highly preferred for solar energy storage is viable in the visible range (λ = 600 nm) with the vanadium based photocatalyst $InVO_4$ while most of the other photocatalysts can work only in the UV region (<420 nm).[53] $InTaO_4$ and $InNbO_4$ have shown the potential to be catalytically active in the visible region up to a wavelength of 500 nm.[54] The experimental band gap observed for $InVO_4$ is 1.9 eV. This band gap is much narrower in comparison to that of the two other photocatalysts $InNbO_4$, $InTaO_4$ (2.5 and 2.6 eV respectively).[55] A linear decrease in the photocatalytic potential with respect to increasing wavelength was observed thus proving that the catalyst is active over a wide range of wavelengths. It was suggested by Oshikiri et al.[53] that keeping a large separation between V –V might be one of the keys for a good photocatalyst. TiO_2 is the commonly used photocatalyst for the degradation of organics, but the application of this material is limited to the ultra violet region due to its relatively wide band gap of 3.2 eV. The increasing demand for the photocatalytic degradation of organic pollutants using solar energy resulted in the discovery of Ag and $InVO_4$ co-doped TiO_2 photocatalytic thin films.[56] These thin films can perform visible light induced photo-catalytic degradation of aqueous methyl orange and gaseous formaldehyde. Also, $InVO_4$/acac films showed high electrochemical stability and a charge capacity up to 40 $mCcm^{-2}$, making them potential candidates for counter-electrode applications in electrochromic devices.[57]

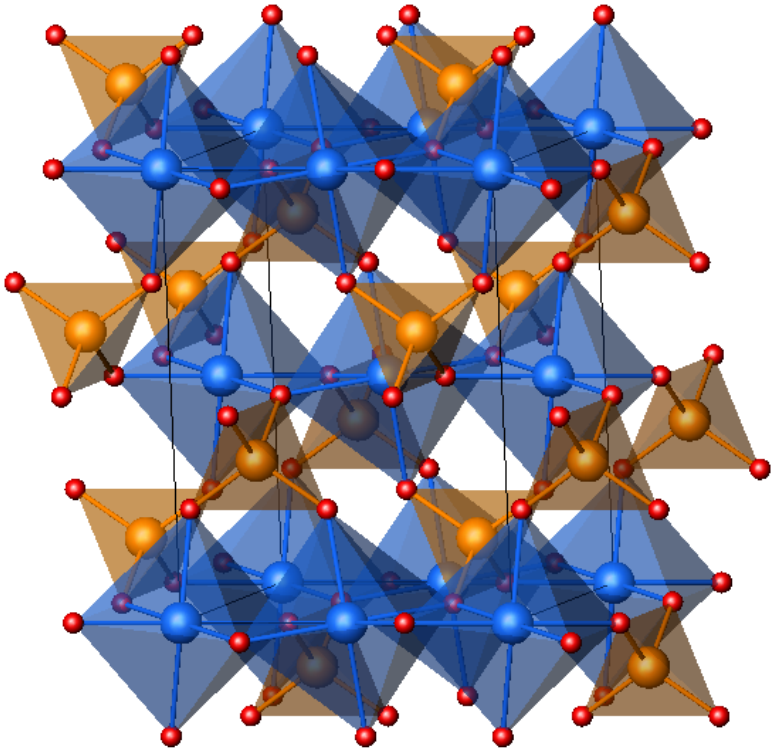

Figure 1.4. Orthorhombic $InVO_4$ structure where chains of InO_6 octahedra (blue) are linked together by VO_4 tetraheda (orange). Oxygen atoms are shown as red spheres.

1.5. AVO_3 (A = RE, In, Sc) Structures

The AVO_3 (A = La – Lu) series encompass a wide range of diverse crystallographic varieties and associated physical properties such as simultaneous crystallographic and magnetic transitions, canted-spin antiferromagnetism with orbital ordering[58,59] and magnetic field dependent as well as temperature induced spin reversal.[60-62] These properties are inherently related to the structural flexibility of the perovskite structure. The perovskite structure with general formula ABX_3 is named after the mineral $CaTiO_3$.[63] The ideal perovskite structure is cubic with the space group $Pm\bar{3}m$. In the ideal perovskite structure, A cations are surrounded by 12 anions in cubo-

octahedral coordination and B cations are surrounded by 6 anions in octahedral coordination as shown in figure 1.5.a. The perovskite structure has great versatility in adopting unmatched A-O and B-O bond lengths; this would lead to deviation from the ideal cubic structure due to structural distortions. The majority of the perovskites do not form the cubic structure; they crystallize in structures with lower symmetries[64] such as the orthorhombic $GdFeO_3$ – type structure shown in figure 1.5.b. In order to accommodate various A-cation sizes, the structure can tolerate octahedral distortions, cation substitution, orbital ordering and has the ability to undergo cooperative octahedral tilting.

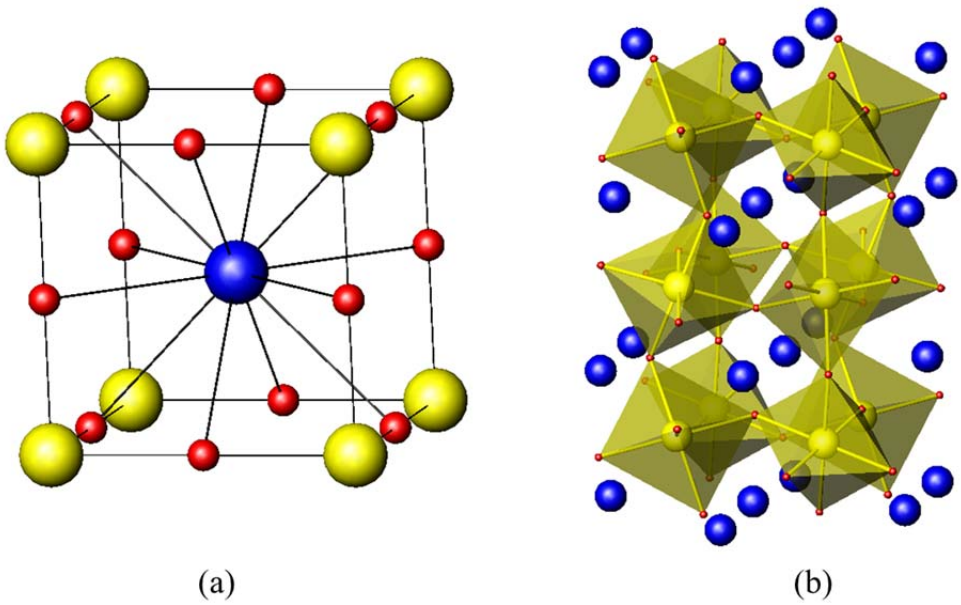

Figure 1.5. (a) Ideal cubic perovskite structure with the A cation in the 12-fold coordination. (b) Distorted orthorhombic perovskite structure. A and B cations are represented with blue and yellow spheres respectively.

The AVO_3 rare earth orthovanadates display an increased mismatch between the size of the A^{3+} cation and the vanadium oxide octahedral network for heavier rare earth

cations. The size of the A^{3+} cation decreases moving from La - Lu, consequently there is an increase in the octahedral tilting which affects the corresponding perovskite stability. The stability of the perovskite structure can be predicted using the Goldschmidt tolerance factor, G_t,[65] shown in Eq. 1.7 where A-O and B-O are respective cation-oxygen bond lengths. For ideal perovskite structures, G_t is unity and the perovskite family is found to cover the tolerance factor range of $0.78 < G_t < 1.05$.[65,66] $G_t > 1$ implies that the A cation is too large and this in turn affects the B-cation octahedral environment resulting in distortion and B-cation displacement whereas $G_t < 1$ indicates that the B cation is too large for an ideal cubic structure and this results in buckling of the B cation octahedral network in order to account for A-cation bonding. The distortion of the octahedra and cation displacements is driven by electronic instabilities such as Jahn-Teller distortion of the octahedral metal cation.[64] An interesting example of the effect of electronic instability on cation displacement is the ferroelectric displacement of titanium in $BaTiO_3$.[64,67]

$$G_t = \frac{(A-O)}{\sqrt{2}\,(B-O)} \qquad \text{(Eq. 1.7)}$$

The structure of AVO_3 phases is primarily determined by the size of the A^{3+} cations. A^{3+} cations smaller than Lu^{3+} such as Sc^{3+} and In^{3+} adopt the bixbyite structure[68-70] rather than the perovskite structure. At ambient pressure, $ScVO_3$ and $InVO_3$ crystallize in the cubic bixbyite structure which is analogous to the c – Mn_2O_3 structure in space group $Ia\bar{3}$. The bixbyite structure consists of edge and corner sharing (A/V) – O_6 octahedra as shown in figure 1.6. There are two distinct metal sites, *8b* and *24d*, in the bixbyite structure and the cations A^{3+} and V^{3+} are distributed randomly over these two

metal positions. The *8b* site forms a regular octahedron while the *24d* site forms a distorted octahedron.

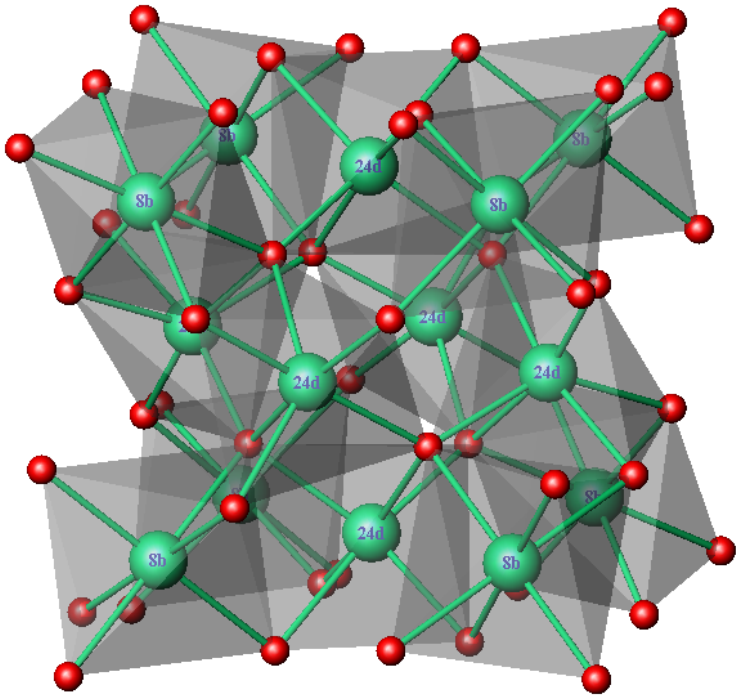

Figure 1.6. AVO_3 cubic bixbyite crystal structure in space group $Ia\bar{3}$. The cations are randomly distributed over the two octahedral sites *8b* and *24d*. Green spheres = cation positions, red spheres = oxygen position.

1.6. $BaCeO_3$ Perovskite Structure

This section is relevant to Chapter 6. Indium doped $BaCeO_3$ was used as a precursor for the synthesis of metastable In – doped CeO_2. During the last two decades doped $BaCeO_3$ perovskites gained significant attention due to their proton conductivity property which finds application in solid state electrochemical devices such as fuel cells, gas sensors etc. Perovskite type lanthanum doped $BaCeO_3$ were originally studied by Virkar and Maiti.[71] Knight carried out extensive studies[72,73] on the temperature dependent

behavior of $BaCeO_3$. At room temperature $BaCeO_3$ crystallizes in the orthorhombic structure in *Pnma* (space group #62). Knight identified three structural phase transitions for $BaCeO_3$ between room temperature and 1273 K using high temperature powder neutron diffraction. The structural phase transitions observed were orthorhombic (*Pnma*) to orthorhombic (*Imma*, space group #74) at 563 K, orthorhombic *Imma* to rhombohedral *R-3c* (space group #167) at 673 K and rhombohedral *R-3c* to cubic *Pm-3m* (space group #221) at 1173 K. The respective structures are shown in figure 1.7.

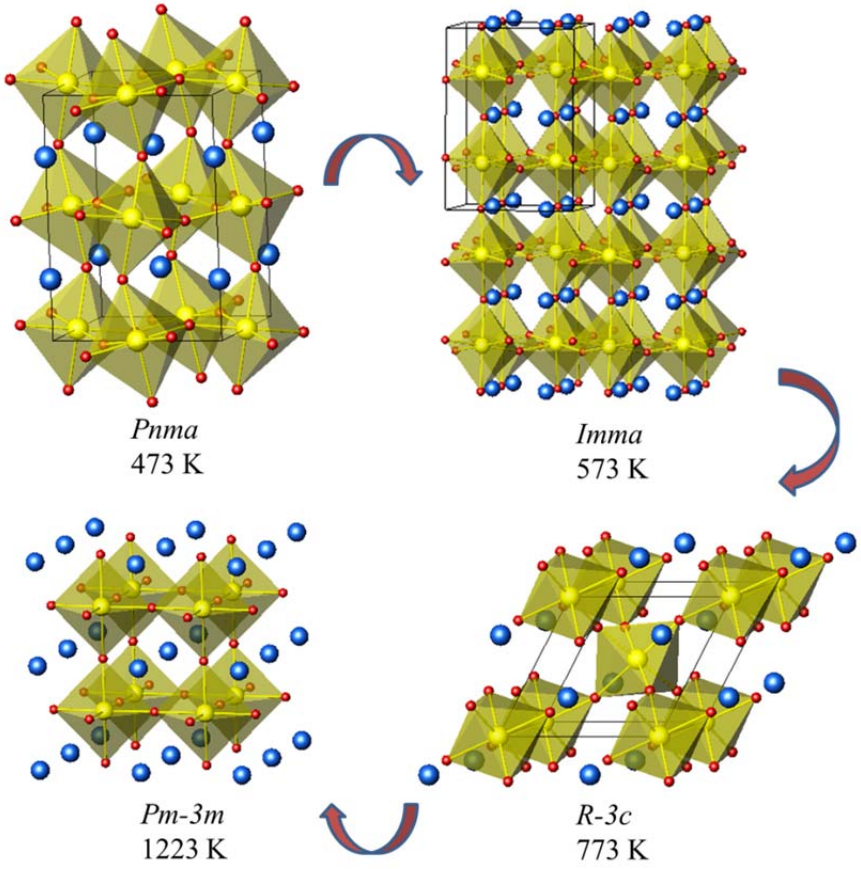

Figure 1.7. The crystal structures of four $BaCeO_3$ phases existing between room temperature and 1223 K. The phase transition sequence is *Pnma* ➔ *Imma* ➔ *R-3c* ➔ *Pm-3m* as shown by the curved arrows in the figure. Blue spheres – Ba^{2+}, yellow octahedra – CeO_6, red spheres – oxygen.

Introduction – Part II

1.7. Diffraction

Diffraction is a widely used analytical technique for probing the atomic arrangement in materials, especially for characterizing crystalline solids. The atoms and ions of crystalline solids are distributed in space in an ordered and repetitive manner; consequently they exhibit long range ordering. However, not all solids are crystalline, many solids lack long range periodicity and are termed "amorphous". In addition, many solids are periodic only in one or two dimensions and some do not have any periodic structures such as quasicrystals and solids with incommensurately modulated structures. Diffraction relies on the interaction of radiation or particles with materials. In crystalline solids the interatomic spacings are of the order of Angstroms (10^{-10} m). Diffraction takes place only when the wavelength of the incident wave is of the same order of magnitude as the spacing of the 'grating'. The commonly used diffraction techniques involve application of x-rays, neutrons or electrons. X-ray diffraction is the primary technique used for the characterization of crystalline materials due to the widespread availability of x-ray diffractometers in laboratory settings. Furthermore, synchrotron sources provide brighter x-rays and permit tuning the wavelength. Neutron diffraction can be used to characterize both the crystallographic and magnetic structures of materials. Compared to x-rays, neutrons interact weakly with matter and usually provide smaller fluxes; consequently larger samples are required for neutron diffraction. Often, neutron and x-ray diffraction are used as complementary techniques. Electrons can also be used for diffraction; however they interact strongly with matter resulting in multiple scattering events which cause complications during the structural analysis. Low energy electrons

can be used for surface structure determination as they do not penetrate deeply into the specimen. Electrons have the advantage that they can also be used for imaging of direct space.

1.8. Powder X-ray Diffraction

X-rays interact weakly with matter and consequently x-ray diffraction is limited to single scattering (x-rays do not get scattered more than once) which is termed the kinematic approximation.[74] X-ray diffraction from crystallographic planes can be explained using Bragg's law which establishes a fundamental relationship between the wavelength, diffraction angle and interplanar spacing. The Bragg condition for diffraction of x-rays by a crystal is illustrated in figure 1.8. All the crystallographic planes with identical Miller indices are parallel to each other with equal spacing. These imaginary planes which include atoms of the crystal lattice are marked as a set of parallel planes with Miller indices (*hkl*) and interplanar spacing d_{hkl} in figure 1.8. A large number of sets (*hkl*) of planes exist in each crystal system and these planes are classified according to their interception with the unit cell axes. Figure 1.8 shows an incident wavefront forming an angle θ with the crystallographic planes (*hkl*) and the reflected wavefront also forms an angle θ with all the planes. It can also be noted from the figure that the lower incident and reflected beams travel longer distances compared to the corresponding upper beams. The path difference (Δ) introduced between a pair of incident and reflected beam is related to the interplanar distance (d_{hkl}) such that $\Delta = d_{hkl}\sin\theta$. Consequently the total path difference is $2\Delta = 2\, d_{hkl}\sin\theta$. For constructive interference to take place the path difference must be equal to an integer (*n*) multiple of the wavelength (λ). Hence according to Bragg's law:

$$n\lambda = 2d_{hkl}\sin\theta \qquad \text{(Eq. 1.8)}$$

Diffraction peaks are generated when constructive interference between the reflected beams takes place and the diffracted beams which do not follow Bragg's law will result in destructive interference. Diffraction data are usually presented as a function of 2θ and as a consequence of Bragg's law the diffraction peaks corresponding to the larger d_{hkl} spacing will appear at lower 2θ and vice versa.

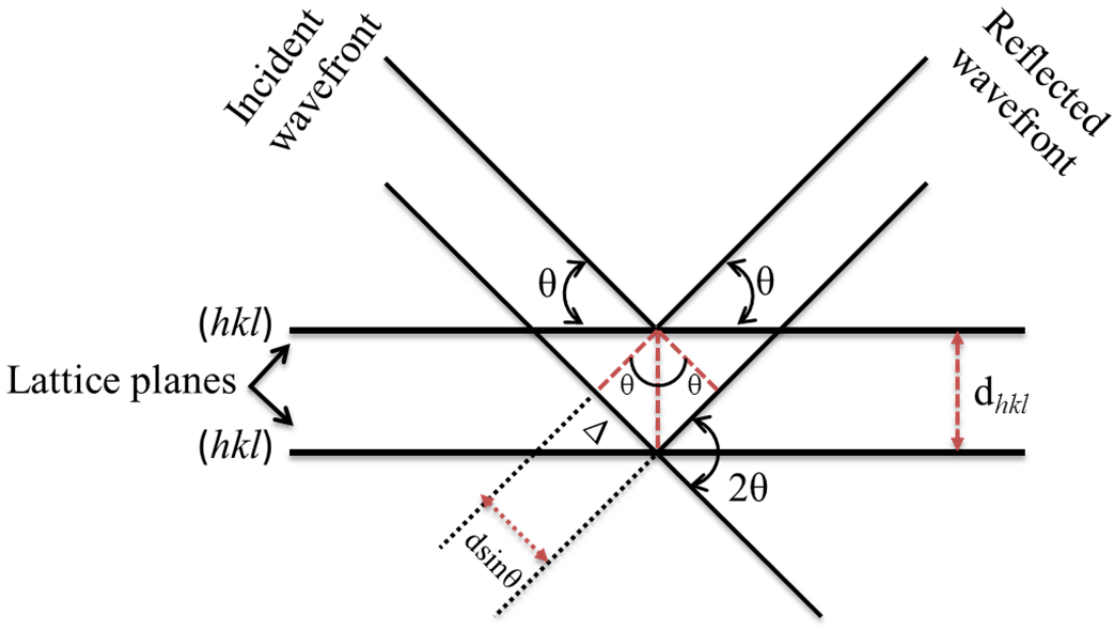

Figure 1.8. Schematic illustration of Bragg's law.

The characteristic wavelengths produced by typical anode materials in x-ray tubes range from 0.5 to 2.3 Å.[75] The two most commonly used anode materials are Cu (Kα ≈ 1.54 Å) in powder and Mo (Kα ≈ 0.71 Å) in single crystal diffractometry.

1.8.1. Origin of Diffraction Pattern

1.8.1.1. Reciprocal Lattice and Ewald's Sphere

The concept of the reciprocal lattice facilitates the understanding of both periodic structures and diffraction geometry.[74] The elementary translations **a**, **b** and **c** in a three dimensional direct lattice are related to those in the reciprocal lattice according to Eq. 1.9 to 1.11.[75] The dot product of two vectors, which is equal to the product of the absolute values of the two vectors and the cosine of the angle between them, is a scalar quantity. On the other hand the cross product of two vectors, which is equal to the product of the absolute values of the two vectors and the sine of the angle between them, is a vector quantity. The length of this vector is equal to the area of the parallelogram formed and its direction is perpendicular to the parallelogram.[75]

$$\mathbf{a}^* = (\mathbf{b} \times \mathbf{c})/V \qquad \text{(Eq. 1.9)}$$

$$\mathbf{b}^* = (\mathbf{c} \times \mathbf{a})/V \qquad \text{(Eq. 1.10)}$$

$$\mathbf{c}^* = (\mathbf{a} \times \mathbf{b})/V \qquad \text{(Eq. 1.11)}$$

where **a**, **b** and **c** are elementary translational vectors of the direct lattice, **a***, **b*** and **c*** are elementary translations of the reciprocal lattice and V is the volume of the unit cell in the direct lattice. The volume of the unit cell is a scalar quantity. Consequently **a*** is perpendicular to both **b** and **c; b*** is perpendicular to both **a** and **c;** and **c*** is perpendicular to both **a** and **b**. The interplanar distance $\mathbf{d}^*_{hkl}$ in the reciprocal lattice is perpendicular to the corresponding set of real space d_{hkl} planes and its length is inversely proportional to d_{hkl}.[75]

$$\left| \mathbf{d^*_{hkl}} \right| = 1/d_{hkl} \qquad \text{(Eq. 1.12)}$$

As a consequence of Eq. 1.12, each set of crystallographic planes in the direct lattice can be represented by a $\mathbf{d^*}_{hkl}$ vector or a point at the end of that vector in the reciprocal lattice. The symmetry of the direct lattice is retained in the reciprocal lattice.

Diffraction can be visually better represented using Ewald's sphere.[75] The following description of diffraction is for a single crystal. Consider an incident beam with propagation vector **k**, a wavelength λ and the length of $\left| \mathbf{k} \right| = 1/\lambda$. As the wavelength remains the same during elastic scattering, the scattered wavevector **k′** will have the same length as **k** such that $\left| \mathbf{k} \right| = \left| \mathbf{k'} \right| = 1/\lambda$. The angle between **k** and **k′** is 2θ. The two wavevectors are superimposed with the reciprocal lattice such that the end of **k** coincides with the origin of the reciprocal lattice as shown in figure 1.9. Then as shown by Ewald, constructive diffraction in the direction of **k′** only occurs if its end coincides with a reciprocal lattice point.[75] Since **k** and **k′** have equal lengths independent of the direction of **k′** (related to the incident angle), the possible orientations of **k′** will result in a sphere in three dimensions which is called Ewald's sphere. Bragg's law can be derived using simple geometry from figure 1.9.

$$\left| \mathbf{d^*} \right| \mathbf{/2} = \left| \mathbf{k} \right| \sin\theta = \left| \mathbf{k'} \right| \sin\theta \qquad \text{(Eq. 1.13)}$$

Recalling $\left| \mathbf{d^*} \right| = 1/d$ and $\left| \mathbf{k} \right| = \left| \mathbf{k'} \right| = 1/\lambda$, Eq. 1.13 implies

$$(1/\lambda)\sin\theta = (1/\lambda)\sin\theta = 1/2d \Rightarrow 2d\sin\theta = \lambda \qquad \text{(Eq. 1.14)}$$

The end of k is fixed at the origin of the reciprocal lattice as can be seen in figure 1.9 and therefore the surface of Ewald's sphere will symbolize all the possible endings of

k′ in different directions. The lattice points coinciding with the surface of Ewald's sphere can give a diffraction peak.

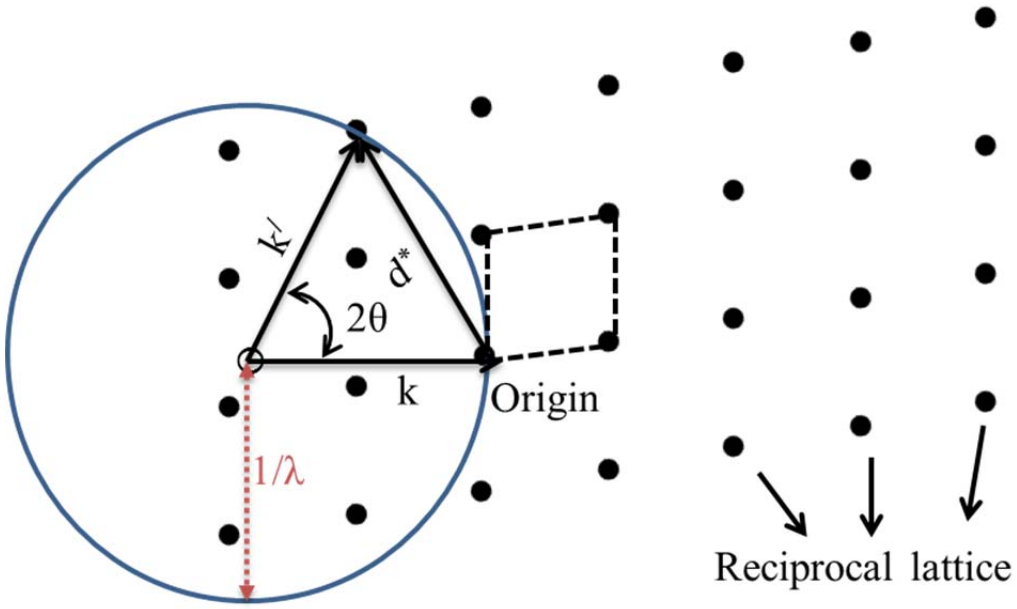

Figure 1.9. Ewald's sphere construction in 2 dimensions to find the directions in which constructive interference can be observed. The reciprocal lattice points are shown as black solid circles. The arrows labeled **k** and **k′** are incident and scattered wavevectors respectively.

In the case of powder diffraction, a large number of crystallites with random orientations are exposed simultaneously to the x-ray beam. Hence there can be a large number of identical d* reciprocal lattice vectors and they will form a circle on the surface of Ewald's sphere. The scattered wavevectors **k′** corresponding to the reciprocal lattice vectors d* will in turn produce a cone shape. Thus the scattered wavevectors from an infinite number of randomly oriented crystallites form rings called Debye rings on the area detector. Several such Debye rings with different diameters and intensities will be formed, each corresponding to certain d^*_{hkl} reciprocal lattice vectors.[75]

1.8.2. Atomic Form Factor and Structure Factor

The strength of the x-ray scattering depends upon the electron density of the constituents in the crystal lattice. The x-ray scattering power of a single atom is called the form factor and is denoted by $f_j(2\theta)$. The scattering factor depends on the diffraction angle θ and the x-ray wavelength. The scattering factor is equal to the number of electrons of the atom at $(\sin\theta/\lambda) = 0$. Figure 1.10 shows the scattering factors for H, O, V and V^{5+}. As can be seen from the figure the form factors gradually decay with increasing diffraction angle, this is due to the radial distribution of core electrons in an atom.[75] Hence it will be challenging to obtain reliable positional coordinates for light elements and to distinguish between atoms with similar electron counts. Note that the form factors for V and V^{5+} differ considerably only at lower diffraction angles.

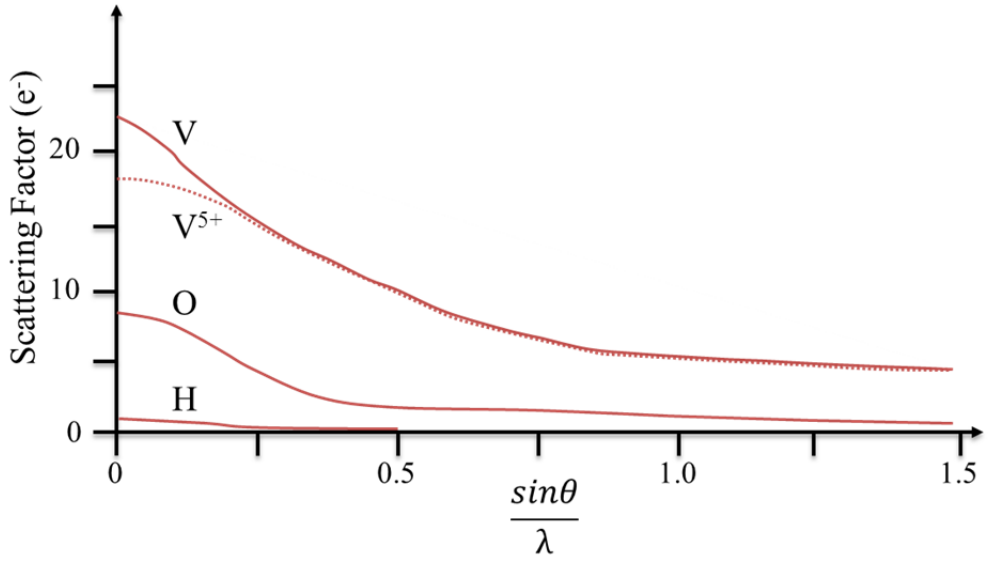

Figure 1.10. Illustration of form factors for H, O, V and V^{5+} as a function of $\sin\theta/\lambda$. For Cu Kα, $\sin\theta/\lambda \approx 0.25$ corresponds to $2\theta \approx 45°$.

The structure factor $F_{(hkl)}$ describes how a crystalline material scatters incident radiation and is defined as the resultant of all scattered waves by all the atoms in the unit cell in the direction of the *hkl* reflection. Eq. 1.15 represents the structure factor $F_{(hkl)}$ where f_j is the form factor of the atom located at (x_j, y_j, z_j) mentioned in the previous section, g_j is the occupation factor and b_j is the temperature factor of the j^{th} atom. The summation is carried out over all *n* atoms in the unit cell.

$$F_{(hkl)} = \sum_{j=1}^{n} g_j b_j f_j\,(2\theta)\exp[2\pi i(hx_j + ky_j + lz_j)] \qquad \text{(Eq. 1.15)}$$

One of the parameters affecting the structure factor is the thermal motion of the atoms about their equilibrium positions which increases with the increase in temperature. The thermal motion causes a change in the electron cloud distribution and consequently a change in the scattering. This parameter is called the atomic displacement parameter or temperature factor *B* and is defined as $B = 8\pi^2\bar{u}^2$ where *u* is the atomic displacement (Å). Therefore the unit of B is $Å^2$ and high values of B results in the decrease of the structure amplitude at higher Bragg angles.[75]

The integrated intensities of the Bragg peaks are related to the corresponding structure factors such that $I_{(hkl)} \propto {F_{(hkl)}}^2$ (Eq. 1.16)

The integrated intensity of Bragg peaks depends on multiple factors[75] as shown in Eq. 1.17.

$$I_{(hkl)} = K \times p_{(hkl)} \times L_\theta \times P_\theta \times A_\theta \times T_{(hkl)} \times E_{(hkl)} \times \left|F_{(hkl)}\right|^2 \qquad \text{(Eq. 1.17)}$$

Each component of the equation 1.17 is briefly discussed here.[75] *K* is the scale factor which is the multiplier used to normalize the experimental integrated intensity to

the calculated intensity and is very significant during the powder diffraction data analysis through Rietveld method. $p_{(hkl)}$ is the multiplicity factor which accounts for the scattering from multiple equivalent reciprocal lattice vectors at the identical Bragg angles in the powder x-ray diffraction pattern. L_θ is the Lorentz factor and is defined by the geometry of the diffraction. L_θ accounts for geometrical effects such as the density of reciprocal lattice points resting on the surface of the Ewald's sphere. P_θ is the polarization factor and it accounts for the partial polarization of the scattered x-ray beam. Absorption effects depend on both the geometry and properties of the sample and the focusing method. Absorption has a significant influence on the scattered intensity from a specimen in transmission geometry. A_θ , the absorption factor, accounts for the absorption of the incident and scattered beams. Another important factor to consider in powder diffraction is the shape of the crystallites. For example, anisotropic crystallite shapes such as platelet-like or needle-like often result in non-random orientations of the crystallites. Such a non-random particle orientation is called preferred orientation. The correction factor T_{hkl} accounts for the preferred orientation. Extinction factor $E_{(hkl)}$ accounts for the secondary or tertiary scattering (re-reflection) of the x-rays. Extinction can cause deviation from the kinematic approximation of diffraction; however in powder specimens the extinction effect is negligibly small.

1.9. Powder Neutron Diffraction

Neutron diffraction is another important method used for crystallographic studies. The limited availability of neutron sources makes this a less commonly used technique. Neutron diffraction has two distinct advantages over x-ray diffraction. Firstly, the

interaction strength of neutrons with light atoms is stronger in comparison to x-rays. Neutrons interact with the nuclei rather than with the electrons. In contrast to x-ray scattering, neutron scattering experiments provide excellent contrast for neighboring elements because the neutron scattering lengths, *b*, do not scale with the atomic number. Secondly, neutrons carry a magnetic moment which interacts with the magnetic moments in the solid. Thus, information regarding the magnetic structure of materials can be attained using neutron diffraction.

Neutrons can be generated by two methods. The first method is by the nuclear fission of ^{235}U with thermal neutrons in nuclear reactors. A continuous flux of neutrons is produced in fission reactors. The second method is based on the spallation process, where a heavy element target is bombarded with high energy charged particles such as protons. The energy of the neutrons released from the neutron sources is of high energy, on the order of MeV. For scattering experiments, neutrons with energies in meV are required.[76] Moderators are used to slow down the high velocity neutrons produced by the two methods. The commonly used moderators are H_2O and D_2O.[76] The Maxwellian distribution shown as Eq.1.18 correlates the distribution of wavelength to the mass (*m*) and wavelength (λ) of the neutrons and the moderator temperature.[76] Depending upon the temperature of the moderator, the wavelength distribution varies. A moderator kept at room temperature gives rise to a maximum peak flux for a neutron wavelength $\lambda \approx 1$ Å.[76]

$$\Phi(\lambda) \propto \frac{1}{\lambda^3} \exp\left(-\frac{h}{2kTm\lambda^2}\right) \qquad \text{(Eq. 1.18)}$$

1.9.1. Interaction of Neutrons with Nuclei

During an elastic scattering event, the incident (**k**) and scattered (**k′**) beam vectors can be related to the wavelength as shown in Eq. 1.19.

$$\lambda = \frac{2\pi}{|k|} = \frac{2\pi}{|k'|} \qquad \text{(Eq. 1.19)}$$

The neutron scattering vector **Q** can be defined in terms of the incident (**k**) and scattered (**k′**) beam vectors as shown in Eq. 1.20.

$$\mathbf{Q} = \mathbf{k} - \mathbf{k'} \qquad \text{(Eq. 1.20)}$$

From Eq. 1.19 and Eq. 1.20, the following equation (Eq. 1.21) relating the neutron scattering vector **Q**, wavelength λ and scattering angle θ can be derived.

$$Q = \frac{4\pi sin\theta}{\lambda} \qquad \text{(Eq. 1.21)}$$

Schematic illustrations of the elastic scattering process and the relationship between the three participating vectors are shown in figure 1.11.

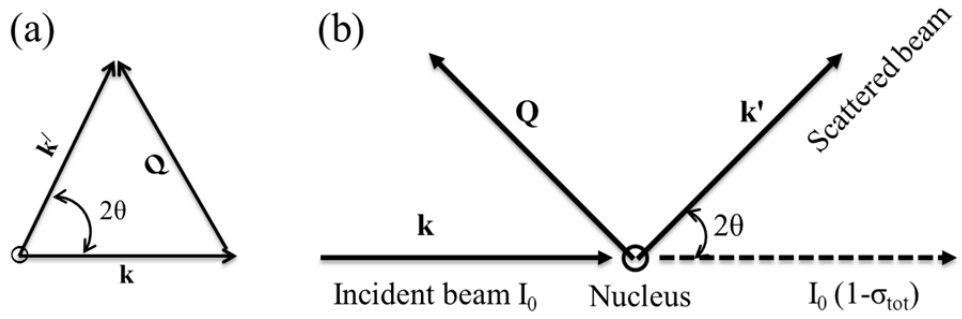

Figure 1.11. (a) Schematic illustration of the relationship between neutron scattering vector **Q** and the incident **k** and scattered **k′** beam wavevectors. (b) Schematic representation of an elastic neutron scattering event.

Two important terms associated with neutron scattering are the scattering cross section σ and the scattering length *b*.[77] As neutrons are chargeless, they penetrate deeply into the atoms and interact with the nucleus. The cross section σ is related to the probability of interaction between the nucleus and the incident beam of neutrons and the interaction can result in either absorption or scattering. The scattering cross section σ is related to the scattering length *b* as shown in Eq. 1.22. The scattering length *b* is independent of the diffraction angle θ; consequently diffraction peaks with good intensity can be observed even at high angles in neutron diffractograms. Also, note that the isotopes of a given element have different scattering lengths *b*, therefore distinction between different isotopes can be achieved through neutron diffraction. The structure factor for neutron diffraction can be expressed as shown in Eq. 1.23.

$$\sigma = 4\pi b^2 \qquad \text{(Eq. 1.22)}$$

$$F_{(hkl)} = \mathbf{\Sigma}^{n}_{j=1} b_j \exp[2\pi i(hx_j + ky_j + lz_j)] \qquad \text{(Eq. 1.23)}$$

1.10. Data Analysis

1.10.1. Rietveld Method

The most commonly employed technique for refining crystallographic structures from powder diffraction data is the Rietveld method. The Rietveld method requires a reliable structural model which would give a calculated diffraction profile resembling the experimental pattern. Crystal structure determination requires crystallographic parameters of this model and the instrumental parameters to be refined against the experimental powder diffraction data and the resulting final refined structure should be reasonable from both physical and chemical perspectives. The Rietveld refinement is based on non-linear least squares minimization of the residuals between the experimental and calculated profiles. The residual Φ can be expressed in terms of observed intensity (Y_{oi}), calculated intensity (Y_{ci}) and a weighting factor (w_i) as shown in Eq. 1.24.[75] Y_{oi} and Y_{ci} are the observed and calculated intensity of the i^{th} point of the powder diffraction profile respectively. The weighting factor w_i is related to the photon counting statistics such that $w_i = \frac{1}{Y_{oi}}$.

$$\Phi = \sum_i^n w_i \ (Y_{oi} - Y_{ci})^2 \qquad \text{(Eq. 1.24)}$$

The initial structural model is refined step by step until the difference between observed and calculated profiles is minimal. Good agreement between observed and calculated profiles requires refinement of both structural and instrument parameters. The frequently refined parameters are unit cell parameters, atomic coordinates, Debye-Waller factor (temperature factor), site occupancy factor, profile background, scale factor, zero

point, sample displacement, peak shape function, instrumental resolution function and peak asymmetry. Caglioti's equation[78] can be used to model the instrumental resolution function. Eq. 1.25 represents the Caglioti equation where *H* is the full width at half maximum intensity of the reflection at an angle θ and U, V and W are refinable parameters.

$$H^2 = \mathrm{U}\tan^2\theta + \mathrm{V}\tan\theta + \mathrm{W} \qquad \text{(Eq. 1.25)}$$

The quality and reliability of the Rietveld fit is determined according to numerical figures of merit shown below.[75] The agreement factors are R_p (profile residual), R_{wp} (weighted profile residual), R_{exp} (expected profile residual), χ^2 (goodness of fit) and R_{Bragg} (Bragg factor). *n* is the number of data points and *p* is the number of refined parameters.

$$\text{Profile residual, } R_p = \frac{\sum_{i=1}^{n} |Y_{oi} - Y_{ci}|}{\sum_{i=1}^{n} Y_{oi}} \times 100\% \qquad \text{(Eq. 1.26)}$$

$$\text{Weighted profile residual, } R_{wp} = \left[\frac{\sum_{i=1}^{n} w_i\,(Y_{oi} - \mathrm{Y}_{ci})^2}{\sum_{i=1}^{n} w_i (Y_{oi})^2}\right]^{\frac{1}{2}} \times 100\% \qquad \text{(Eq. 1.27)}$$

$$\text{Expected profile residual, } R_{exp} = \left[\frac{n-p}{\sum_{i=1}^{n} w_i (Y_{oi})^2}\right]^{\frac{1}{2}} \times 100\% \qquad \text{(Eq. 1.28)}$$

$$\text{Goodness of fit, } \chi^2 = \frac{\sum_{i=1}^{n} w_i\,(Y_{oi} - \mathrm{Y}_{ci})^2}{n-p} = \left[\frac{R_{wp}}{R_{exp}}\right]^2 \qquad \text{(Eq. 1.29)}$$

$$\text{Bragg factor, } R_{Bragg} = \frac{\sum_{i=1}^{m} |I_{oi} - I_{ci}|}{\sum_{i=1}^{m} I_{oi}} \times 100\% \qquad \text{(Eq. 1.30)}$$

There are no absolute values or threshold values for the profile residuals to determine the quality of the fit. In the profile residual R_p, observed and calculated intensities are compared directly whereas in R_{wp} a weighting scheme w_i is applied. The quality of the fit is usually estimated using χ^2 which correlates R_{wp} and R_{exp} as shown in Eq. 1.27. R_{exp} can be used as a measure of quality of experimental data as a large denominator in Eq. 1.28 requires good counting statistics. A graphical representation of the experimental, calculated and difference plot surpasses the numerical figures of merit in determining the quality of the fit. The difference plot can give hints to the origin of the problems in getting a proper refinement. Errors originating due to various factors including phase contamination, lattice parameters, scale factors and zero offsets can be identified using the difference plot. Note that both R_p and R_{wp} have contributions from the background. An increase in background would result in a large denominator value (Eq. 1.26 and 1.27) giving excellent values for R_p and R_{wp} even when the model or fit does not seem reasonable.

1.10.2. Bond Valence Method

The bond valence method is commonly used to confirm the reliability of a refined crystallographic structure.[79,80] Consider the case where there are inequivalent bonds from an atom j to atoms i. The bond valence, S_{ij}, is defined as a quantity whose sum over each atom is equal to the oxidation state, V_j, of the atom. The bond valence sum should consider the entire coordination sphere.

$$V_j = \sum_i S_{ij} \qquad \text{(Eq. 1.31)}$$

The bond valence is correlated with the bond length as shown in Eq. 1.32.[79] Note that bond valence is inversely related to the corresponding bond distances, Eq. 1.32. R_0 is the bond length of unit valence, R_{ij} is the actual bond length and B is the slope of the correlation curve. The values of R_0 for the majority of the common bonds obtained from already well-established crystal structures are reported by Brown and Altermatt.[81] They also showed that the value of the parameter B can be set to 0.37 Å for most bonds.[81] All these parameters can be accessed easily and the bond valence calculations can be carried out using the program VaList.[82]

$$S_{ij} = \exp(\frac{R_0 - R_{ij}}{B}) \qquad \text{(Eq. 1.32)}$$

Combining Eq. 1.31 and Eq. 1.32, the following expression (Eq. 1.33) can be derived for the oxidation state V_j. The index i in this expression is summed over all bonds in the coordination sphere of the atom.

$$V_j = \sum_i \exp(\frac{R_0 - R_{ij}}{B}) \qquad \text{(Eq. 1.33)}$$

Bond valences have a variety of uses such as identifying errors in the crystallographic structure determination, determining partial occupancies of atomic sites and assigning oxidation states. If there is significant difference between the calculated V_j and anticipated V_j then the structural model used should be reconsidered. Incorrect space groups, missing bonds or atoms etc. may cause large discrepancy. Another important term associated with the bond valences is the Global Instability Index,[83] *GII*, which compares the anticipated oxidation state with the calculated bond valence sums in the formula unit as expressed with Eq. (1.34). The summation is carried out over all N atoms

j. Due to the geometric constraints, the bonding in many structures including perovskites is found to be strained, consequently bonds are either compressed or elongated. Hence, bond valence sums for cations can be either too large (compressed bonds) or small (elongated bonds). The Global Instability Index can be used to study the degree of strain in the structure. If *GII* is greater than 0.2, then the structure obtained is considered incorrect.[83]

$$GII = \sqrt{\frac{\sum_j^N \left\{ \left(\sum_j s_{ij} - v_j \right)^2 \right\}}{N}} \qquad \text{(Eq. 1.34)}$$

The occupancies of two disordered ions on a single crystallographic site can be determined using the following expression[84] where *x* and *y* are occupancies of *m* and *n* respectively. The occupancies *x* and *y* can be calculated since $x + y = 1$ for a fully occupied site.

$$x \sum S_m + y \sum S_n = xV_m + yV_n \qquad \text{(Eq. 1.35)}$$

1.11. Thermal Analysis

Characterization of physical and chemical properties such as enthalpy, heat capacity and mass changes can be achieved through thermal analysis and the measurements are carried out as a function of temperature.[85] Thermal analysis aids in understanding solid state reactions including thermal decomposition, phase transitions and understanding phase diagrams. Thermogravimetric analysis (TGA), differential thermal analysis (DTA) and differential scanning calorimetry (DSC) belong to the class of thermal analysis techniques. In TGA, the mass change of a sample is monitored as a function of temperature or time. The sample (typically milligrams) is heated at a constant

rate and the change in mass is monitored throughout the process. The change in mass can be used for the quantitative calculation of the changes in composition. Note that reaction temperatures depend upon the heating rate, the reaction atmosphere inside the furnace etc. In DTA the difference in temperature between the sample and an inert standard (reference) is measured during a programmable heating or cooling cycle. DTA is used for qualitative measurements whereas DSC allows for quantitative measurement such as enthalpy changes. In a DTA set up, the sample and the reference are placed in crucibles on a heating block and are connected to each other via identical thermocouples. As long as there is no thermal process occurring, the temperatures of both the sample and reference remain the same; consequently the net output of the pair of thermocouples is zero. A temperature difference arises with the onset of a thermal process resulting in a net output voltage of the thermocouples. The temperature of the heating block on which the sample and the reference are placed is measured using another thermocouple.[85] The difference in temperature measured in ° C or μV is plotted against the temperature. If the temperature of the sample is lower than that of the reference, the thermal process is endothermic and if the sample temperature is higher the thermal process is exothermic in nature. A schematic illustration of the Linseis L81 thermal analyzer is shown in figure 1.12 (the instrument can carry out TGA/DTA measurements simultaneously). The main components of this thermal analyzer are sample head, furnace, fulcrum, two electromagnets and two counterweights. The design of the instrument is based on a compensation balance. The mass change during the measurement is compensated by regulating the current to the electromagnets so that all the components remain stationary. The current is amplified to produce the TGA signal.

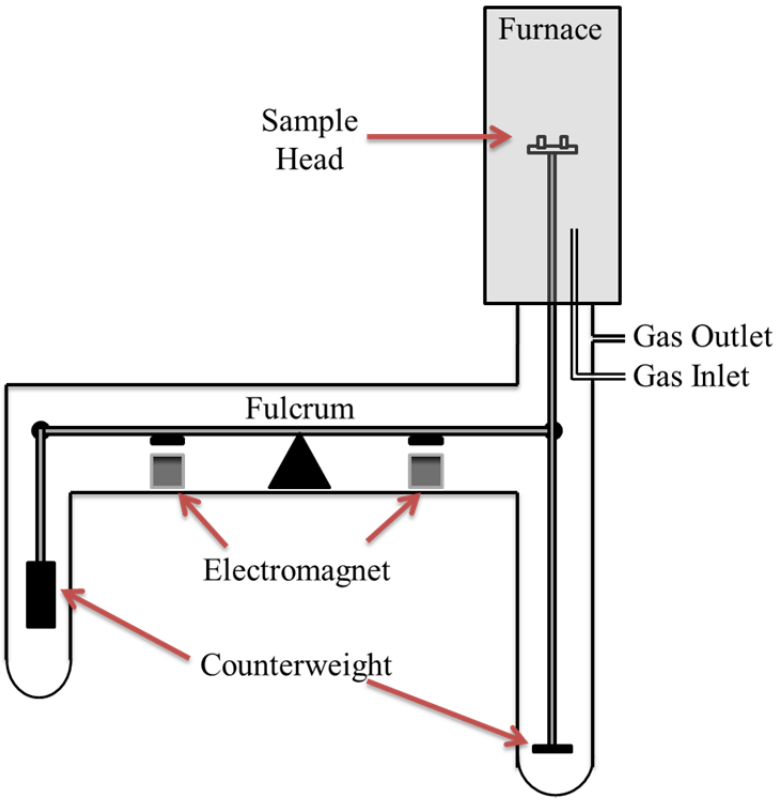

Figure 1.12. Schematic illustration of Linseis L81 thermo balance.

1.12. Magnetism

1.12.1. Paramagnetism and Diamagnetism

Paramagnetism exists only in those materials in which the atoms or molecules have permanent magnetic moments.[86] Paramagnetism originates from the spin angular momentum of the unpaired electrons and the orbital angular momentum. However, the atoms or ions do not interact with each other and therefore no net magnetic moment is observed. The total magnetic moment, μ, can be defined as Eq. 1.36 where g is the Landé splitting factor (Eq. 1. 37), J is the total angular momentum quantum number and μ_B is the Bohr magneton. For 3d transition metal elements, the orbital angular momentum contribution is quenched, consequently only spin angular momentum contributes to the

magnetic moment. The quenching of orbital angular momentum is primarily due to the restriction of the orbital motion of electrons due to interaction with the crystal field of surrounding atoms or ions. On the contrary, for lanthanides both spin and angular momentum contribute to the total magnetic moment.

$$\mu = -gJ\mu_B \qquad \text{(Eq. 1.36)}$$

$$\text{Landé splitting factor } g = \frac{3J(J+1)+S(S+1)-L(L+1)}{2J(J+1)} \qquad \text{(Eq. 1.37)}$$

L is the total orbital momentum ($L = \Sigma m_l$), S is the total spin momentum ($S = \Sigma m_s$) and J is the total angular momentum which can be calculated from L and S by applying Hund's rules. The Landé g factor = 2 for free electrons.

The magnetic property of a material is classified according to its response to an applied magnetic field H. Such a response χ, the magnetic susceptibility, can be related to the magnetization M and H as shown in Eq. 1. 38.

$$M = \chi H \qquad \text{(Eq. 1.38)}$$

Diamagnetism is caused by the paired electrons and therefore atoms or molecules with closed shell electrons are diamagnetic. These materials have a very small temperature independent negative molar susceptibility of the order of -1 to -100 x 10^{-6} e.m.u./mol.[87] Note that the susceptibility is negative and therefore the induced magnetic moment is in the opposite direction to the applied magnetic field.

Dilute magnetic systems show paramagnetism with no cooperative magnetic interaction. For paramagnetic materials the susceptibility is positive and temperature

dependent. Since the susceptibility is positive the induced magnetic moment is along the direction of the magnetic field. The susceptibility is of the order of 10^{-2} e.m.u./mol at room temperature[86] and is inversely proportional to the temperature. There are two competing effects taking place in paramagnets: the applied field tending to orient the magnetic moments along the field direction and the thermal energy opposing this by randomizing these magnetic moments. The interplay between susceptibility (applied field effect) and temperature (thermal randomization) can be described using the Curie Law (Eq. 1.39)

$$\chi = \frac{C}{T} \qquad \text{(Eq. 1.39)}$$

where the Curie constant, $C = \frac{Ng^2\mu_B^2 J(J+1)}{3k}$, N is Avogadro's number. The calculated values of the Curie constant agree very well with the experimental values for materials containing rare earth ions. However, the agreement is less promising for 3d transition metal compounds because of the quenched orbital contribution. For the spin-only magnetic moment, $C = \frac{Ng^2\mu_B^2 S(S+1)}{3k}$ and $\mu_{eff} = g\sqrt{S(S+1)}\mu_B$. Hence the effective magnetic moment can be calculated with Curie's Law using the Eq. 1.40.

$$C = \frac{N\mu_{eff}^2}{3k} = \frac{\mu_{eff}^2}{8} \Rightarrow \mu_{eff} = 2.828\sqrt{C} \qquad \text{(Eq. 1.40)}$$

For experimental data diamagnetic corrections are applied to paramagnetic susceptibilities to account for contributions from the paired core electrons.

1.12.2. Cooperative Magnetism

Spontaneous interaction between neighboring spins may result in cooperative magnetism. Ferromagnetism, antiferromagnetism and ferrimagnetism belong to this category. Parallel alignment of magnetic moments is observed in ferromagnetic states whereas in antiferromagnetic states the magnetic moments are aligned in antiparallel fashion. Therefore there is a large net magnetization for ferromagnets whereas this is zero for antiferromagnets. In ferrimagnets the opposing magnetic moments do not cancel and a net magnetic moment results. Ferrimagnetism can occur when atoms with different magnetic moments interact with each other. Depending upon the length scale of spin ordering, magnetic interactions can be classified as short range ordered and long range ordered. Interaction between the magnetic moments in the paramagnetic state for ferro and antiferromagnetic materials can be described by introducing the Weiss temperature θ in the Curie law as shown in Eq. 1.41 which is called the Curie-Weiss law.[85]

$$\chi = \frac{C}{T-\theta} \qquad \text{(Eq. 1.41)}$$

Magnetic susceptibility measurements can be used to identify materials with cooperative magnetism. Typical χ vs. T and χ^{-1} vs. T plots are shown in figure 1.13 (a) and (b) respectively. As expected the χ vs. T plot shows a straight line with zero slope for a diamagnet since the susceptibility is temperature independent. When there is cooperative behavior, temperature dependence is observed. The transition from independent to cooperative behavior is associated with a characteristic temperature. Below the transition temperature, ferromagnets (T_C: Curie temperature) show an increase in susceptibility and antiferromagnets (T_N: Néel temperature) show a decrease in

magnetic susceptibility during cooling. Above the transition temperature, both ferro- and antiferromagnets obey the Curie-Weiss law (figure 1.13.b). Hence χ^{-1} vs. T plot shows a linear fit for the high temperature regime for ferro and antiferromagnets. The slope of this linear fit is C^{-1} and the extrapolated T-intercept is the Weiss temperature (θ) which is positive for ferromagnetic and negative for antiferromagnetic overall interaction.[85]

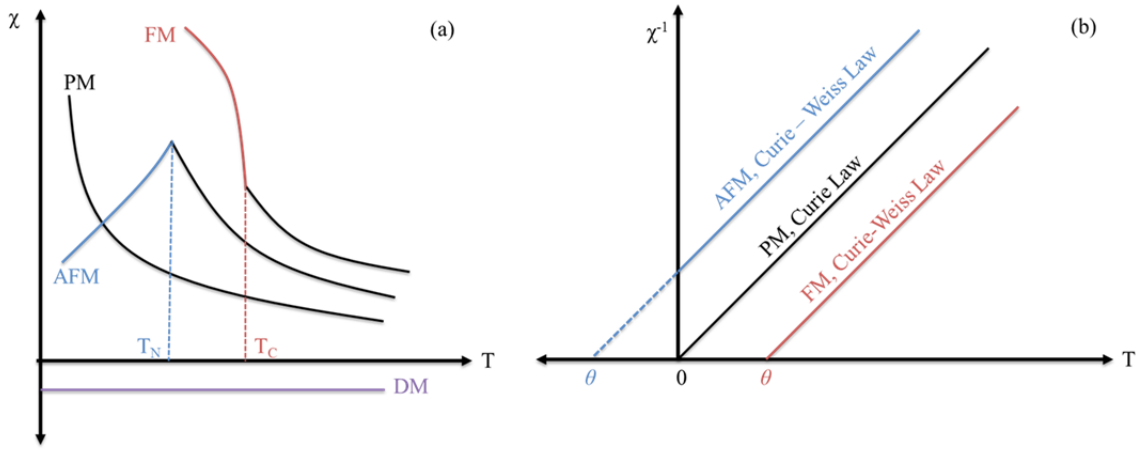

Figure 1.13. (a) Typical χ vs. T plots for a paramagnet (PM), diamagnet (DM), ferromagnet (FM) and antiferromagnet (AFM). The characteristic transition temperature T_N for an antiferromagnet and T_C for a ferromagnet is shown. (b) Representative χ^{-1} vs. T plots for a paramagnet (PM), ferromagnet (FM) and antiferromagnet (AFM). The Weiss temperature θ is shown for ferromagnet (positive) and antiferromagnet (negative).

Magnetic ordering is not due to dipole – dipole interactions of the magnetic moments. Instead, the magnetic moment alignment is the result of an exchange interaction which is due to the combination of Coulomb interaction and the Pauli principle.[74] In cooperative magnetic systems two types of interactions can occur: cation – cation (direct interaction) or cation – anion – cation (indirect interaction).[88] In some cases cation-anion-anion-cation interactions are observed.[88] As the names suggest, cation – cation or direct interactions are due to the orbital overlap of magnetic ions and cation –

anion – cation or indirect interactions stem from the coupling of two cations mediated through a non-magnetic anion. The indirect mechanism was first proposed by Kramers in 1934.[88,89] Qualitative prediction of the signs of the coupling constants can be established using the Kanamori and Goodenough rules.[88,90] The two main types of indirect cation – anion – cation interactions are double exchange[91-93] and superexchange. [88,90,94,95] Only a brief introduction to magnetism is provided here as a detailed discussion is beyond the scope of this thesis.

Chapter 2: Experimental Methods

2.1. Synthesis of Materials

2.1.1. Synthesis of $AVO_{3.5}$ (A = Sc, In)

The precursor material AVO_3 bixbyite (A = Sc, In) was prepared by two-step synthesis via AVO_4 zircon. A stoichiometric mixture of In_2O_3 (Alfa Aesar, 99.995%) or Sc_2O_3 (Alfa Aesar, 99.995%) and NH_4VO_3 (CERAC, 99.9%) was ground in acetone and heated at 1000°C for 20 hours with one intermediate grinding according to Eq. 2.1. The $InVO_4$ samples prepared from the stoichiometric amounts of the starting materials showed trace amounts of In_2O_3. Vanadium might have been lost during the reaction process in the form of vapor or by leaching into the alumina boat. After the reaction, the alumina boats were orange-red colored which is characteristic of V_2O_5. Small amounts of vanadium oxide loss were compensated for with 2 mol% excess NH_4VO_3. The amount of In_2O_3 in the final product was reduced to ≈ 1 mass% through this method.

$$A_2O_3 + 2\ NH_4VO_3 \rightarrow 2\ AVO_4 + 2\ NH_3 + H_2O \qquad \text{(Eq. 2.1)}$$

The zircon type $InVO_4$ sample was cream colored. The bixbyite $InVO_3$ was synthesized by the reduction of $InVO_4$ under CO/CO_2 (1:1 volume ratio) atmosphere at 450°C for 12 hours according to Eq.2.2. The polycrystalline sample obtained after the reduction was black in color and contained approximately 1.5 weight% In_2O_3 impurity. The pale-yellow phase-pure zircon-type $ScVO_4$ was reduced under similar conditions at 1000°C to synthesize phase pure $ScVO_3$. AVO_3 bixbyite samples were dark brown in color.

$$AVO_4 + CO \rightarrow AVO_3 + CO_2 \qquad \text{(Eq. 2.2)}$$

Bulk samples of black polycrystalline $AVO_{3.5}$ were synthesized by the topotactic oxidation of AVO_3. $InVO_{3.5}$ was synthesized by the mild oxidation of a thin layer of $InVO_3$ (cast from an acetone slurry) under a CO_2 atmosphere at 350°C for 44 h according to Eq.2.3 whereas $ScVO_{3.5}$ was synthesized in air at 350°C according to Eq.2.4.

$$2\ InVO_3 + CO_2 \rightarrow 2\ InVO_{3.5} + CO \qquad \text{(Eq. 2.3)}$$

$$4\ ScVO_3 + O_2 \rightarrow 4\ ScVO_{3.5} \qquad \text{(Eq. 2.4)}$$

Bulk $InVO_{3.5}$ contained 2 mass% In_2O_3 impurity and $ScVO_{3.5}$ was phase pure.

2.1.2. Synthesis of $ScVO_{4-y}$

Bulk samples of polycrystalline $ScVO_{4-y}$ were prepared via four-step solid state synthesis. $ScVO_{3.5+x}$ was synthesized by the topotactic oxidation of $ScVO_3$ in air at 300°C for 4 hours according to Eq.2.5.

$$4\ ScVO_3 + (1 + 2x)\ O_2 \rightarrow 4\ ScVO_{3.5+x} \qquad \text{(Eq. 2.5)}$$

$ScVO_{3.5+x}$ was partially oxidized to $ScVO_{4-y}$ at 400°C under an oxygen flow for 12 hours according to Eq.2.6. The phase pure $ScVO_{4-y}$ was beige.

$$4\ ScVO_{3.5+x} + (1-2x-2y)\ O_2 \rightarrow 4\ ScVO_{4-y} \qquad \text{(Eq.2.6)}$$

2.1.3. Synthesis of $ScVO_3$ perovskite

The precursor bixbyite $ScVO_3$ for the high pressure synthesis of $ScVO_3$ perovskite was synthesized by the reduction of $ScVO_4$ under a H_2 atmosphere at 1100°C for 12 hours. Using a Belt press the bixbyite precursor was pressed in a 3 mm gold capsule, pressurized to 8 GPa and 5 minutes after pressure stabilization the sample was annealed at 800°C for 30 minutes. The sample was quenched to room temperature and

the pressure was slowly released. The phase pure black perovskite product showed a shinier luster than the starting material. The synthesis of $ScVO_3$ perovskite phase was performed by E. Castillo-Martinez at Universidad Complutense de Madrid in Madrid, Spain.

2.1.4. Synthesis of $ScTiO_{3.5}$ and $Sc_4Ti_3O_{12}$

Polycrystalline $ScTiO_{3.5}$ was synthesized by the topotactic oxidation of $ScTiO_3$. Bulk samples (≈ 2 g) of $ScTiO_3$ were synthesized from a stoichiometric mixture of Sc_2O_3 (Alfa Aesar, 99.99%), TiO_2 (Alfa Aesar, 99.995%) and Ti (Alfa Aesar, 99.99%) according to Eq.2.7. The mixture was ground in acetone, pelletized and heated at 1500°C under high vacuum ($p < 10^{-3}$ mbar) for 4 – 5 hours with one intermediate grinding. The bixbyite $ScTiO_3$ sample was black in color.

$$2\ Sc_2O_3 + 3\ TiO_2 + Ti \rightarrow 4\ ScTiO_3 \qquad \text{(Eq.2.7)}$$

The polycrystalline bulk sample of $ScTiO_{3.5}$ was synthesized by topotactic oxidation of $ScTiO_3$ at 800°C in air for 5 hours according to Eq.2.8. $ScTiO_{3.5}$ was white in color.

$$4\ ScTiO_3 + O_2 \rightarrow 4\ ScTiO_{3.5} \qquad \text{(Eq.2.8)}$$

Polycrystalline $Sc_4Ti_3O_{12}$ was prepared by heating stoichiometric amounts of Sc_2O_3 (Alfa Aesar, 99.99%) and TiO_2 (Alfa Aesar, 99.995%) in air at 1500°C for 12 hours according to Eq.2.9. The cubic $Sc_4Ti_3O_{12}$ was pale yellow in color.

$$2\ Sc_2O_3 + 3\ TiO_2 \rightarrow Sc_4Ti_3O_{12} \qquad \text{(Eq. 2.9)}$$

$Sc_4Ti_3O_{12}$ was reduced in a CO/Ar (1:3 ratio) atmosphere at 1500°C for 12 hours to form oxide defect phase $Sc_4Ti_3O_{12-x}$ according to Eq.2.10. The resulting oxide defect phase was black in color.

$$Sc_4Ti_3O_{12} + x\ CO \rightarrow Sc_4Ti_3O_{12-x} + x\ CO_2 \qquad \text{(Eq.2.10)}$$

The high pressure analogue of $Sc_4Ti_3O_{12}$ was synthesized using a Belt-type apparatus. The polycrystalline cubic $Sc_4Ti_3O_{12}$ synthesized at ambient pressure was used as the starting material. Using a 3 mm diameter gold capsule the sample was pressurized to 8 GPa at a constant rate and 5 minutes after pressure stabilization the sample was annealed at 1350°C for 30 minutes. Then the sample was quenched to room temperature and the pressure was slowly decreased. The product obtained was grayish white in color. The synthesis of high pressure $Sc_4Ti_3O_{12}$ phase was performed by Dr. M. Bieringer at Universidad Complutense de Madrid in Madrid, Spain.

2.1.5. Synthesis of $BaCe_{(1-x)}In_xO_{3-\delta}$ perovskites ($x \leq 0.4$) and $Ce_{(1-x)}In_xO_{2-d}$ ($x \leq 0.2$)

The bulk samples of polycrystalline $BaCe_{(1-x)}In_xO_{3-\delta}$ perovskite phases were prepared by conventional solid state synthesis of stoichiometric amounts of $BaCO_3$ (Alfa Aesar, 99.95%), CeO_2 (Alfa Aesar, 99.99%) and In_2O_3 (Alfa Aesar, 99.995%) at 1200°C for 6 hours in air according to Eq.2.11.

$$BaCO_3 + (1\text{-}x)\ CeO_2 + (x/2)\ In_2O_3 \rightarrow BaCe_{(1-x)}In_xO_{3-\delta}\ (\text{ where } \delta = x/2) + CO_2 \qquad \text{(Eq.2.11)}$$

Polycrystalline samples of $Ce_{(1-x)}In_xO_{2-\delta}$ were synthesized from the corresponding $BaCe_{(1-x)}In_xO_{3-\delta}$ perovskite phases through CO_2-capture reactions. The perovskite phases

were heated under a CO_2 flow at T = 700 - 800°C for 6 hours to synthesize $Ce_{(1-x)}In_xO_{2-\delta}$ according to Eq.2.12. The temperature used for the synthesis depended on the amount of indium in the sample, x. The CO_2 – capture reaction for $x \leq 0.2$ was carried out at 800°C while for $x > 0.2$, the synthesis temperature was reduced to 700°C.

$$BaCe_{(1-x)}In_xO_{3-\delta} + CO_2 \rightarrow Ce_{(1-x)}In_xO_{2-\delta} + BaCO_3 \qquad \text{(Eq.2.12)}$$

2.2. Room Temperature Powder X-ray Diffraction

Powder x-ray diffraction experiments on polycrystalline samples were carried out on a PANalytical X'Pert Pro diffractometer using Cu $K\alpha_{1,2}$ (λ_1 = 1.540598 Å, λ_2 = 1.544426 Å) radiation in Bragg-Brentano geometry. The diffractometer is equipped with a PreFIX (Pre-aligned fast interchangeable X-ray modules) system for modular exchange of functional components including the sample stage, incident beam optics such as Soller slits, mask, divergence slits and anti-scatter slits as well as the diffracted beam anti-scatter slits, Soller slits and K_β filter. The PreFIX concept allows for very reliable and fast instrument customization and "no system re-alignment" is required as long as the x-ray tube is correctly positioned with respect to the diffractometer center. The diffractometer is equipped with a diffracted beam Ni filter and X'Celerator detector. The X'Celerator is a RTMS (Real Time Multiple Strip) based ultra-fast x-ray detector with 128 detector strips offering direct detection of x-rays and has the ability to process high count rates without compromising resolution. The majority of the data collections were carried out using the standard spinner mode where the samples were mounted on a 30 mm obliquely cut zero background silicon holder. Samples were ground in acetone and mounted as a thin layer or were sprinkled on a thin film of grease which acts as an adherent. In a

standard measurement, the data were collected for $10° \leq 2\theta \leq 120°$ with a step size of 0.0167° using 1° divergence and 2° anti-scatter slits. Small air sensitive samples were measured in Debye-Scherrer geometry. Samples were filled in pyrex capillaries (0.3 mm diameter) and sealed with wax. Longer data acquisition times were required for capillary experiments as the diffraction region of the sample is very limited. Preliminary data analysis such as phase identification (PDF 2003), indexing and space group determination were carried out using X'Pert High Score Plus software (version 2.1.0). Detailed crystallographic structural analyses of the powder x-ray diffraction data were carried out using FullProf 2008[i] and GSAS[ii].

2.3. In-situ Powder X-ray Diffraction

In-situ high temperature powder x-ray diffraction experiments were carried out on the PANalytical X'Pert Pro diffractometer mentioned above, equipped with an Anton Paar HTK2000 high temperature chamber. The samples were ground into very fine powders in acetone and mounted directly on the platinum strip heating filament as a thin layer. The initial room temperature sample height adjustment was always carried out with respect to the corresponding room temperature spinner data by aligning the heating filament position manually. The temperature of the furnace is accurate to within at least 5°C between room temperature and 1300°C which is the maximum temperature used for the high temperature x-ray experiments for all the studies reported in this thesis. The temperature was increased in steps and x-ray diffraction data were collected at each

[i] Rodríguez-Carvajal, J. *FullProf. 2k* Vers. 4.40, 2008

[ii] Larson, A. C.; von Dreele, R. B. *General Structure Analysis System*; Los Alamos National Laboratory Report LAUR 86-748 (2004); Los Alamos National Laboratory: Los Alamos, NM, 2004

temperature, occasionally the data during cooling from high temperature to room temperature were also acquired in-situ. The temperature increment and the data acquisition period at each step were varied according to the experimental needs. Also, the atmospheric conditions (air, vacuum, CO, CO_2, inert gas such as He etc.) used depend on the experimental requirements.

2.4. Powder Neutron Diffraction

For various samples ($InVO_{3.5+x}$, $ScVO_{3.5+x}$, $ScVO_{4-y}$, $ScTiO_3$ and rhombohedral $Sc_4Ti_3O_{12}$) room temperature and/or low temperature powder neutron diffraction experiments for crystallographic and magnetic structural analysis respectively were carried out on the high resolution 800 wire diffractometer C2 operated by the National Research Council Canada in Chalk River. Diffractograms were measured using a cylindrical vanadium container. Either both or one of the neutron wavelengths $\lambda = 2.37$ Å (for $5° \leq 2\theta \leq 85°$) and $\lambda = 1.33$ Å (for $35° \leq 2\theta \leq 115°$) were used depending on the experimental requirements. Room temperature powder neutron diffraction data for $ScTiO_3$ and $Sc_4Ti_3O_{12}$ were collected on the high flux diffractometer D20 at the Institut Laue-Langevin (ILL) in Grenoble with $\lambda = 1.87$ Å ((115) reflection from a germanium monochromator at a take – off angle of 118°). Analysis of the diffraction data was carried out using FullProf 2008.

Combined Rietveld refinements were carried out for a variety of samples using powder x-ray and neutron diffraction data. Notably, the unit cell dimensions for the refined phases are constrained to be equal for the neutron and x-ray histograms. Since the x-ray wavelengths (Cu $K\alpha_{1,2}$) are fixed the x-ray data is used to refine the unit cell

parameters while the neutron wavelength is refined simultaneously. Consequently the neutron wavelength is refined against the fixed x-ray wavelengths via the common unit cell dimensions.

2.5. Thermogravimetric Analysis and Differential Thermal Analysis

Simultaneous thermogravimetric analysis (TGA) and differential thermal analysis (DTA) were carried out using a Linseis L81 thermobalance. Finely ground polycrystalline samples in alumina crucibles were heated from room temperature to the desired temperature under a variety of atmospheres such as air, oxygen, CO/Ar, CO_2 etc. depending on the experimental requirements. A typical experiment follows the reaction of an approximately 50 mg sample from 25°C to 1200°C with a linear heating rate of 10°C/min. but the conditions were varied depending on the experiment. The maximum temperature used with the instrument is 1400°C. Al_2O_3 (similar to the sample mass) was used as the reference and all the experiments were buoyancy corrected. The final products were always identified using powder x-ray diffraction.

2.6. Magnetic Measurements

Bulk d.c. magnetic susceptibility measurements were carried using a Quantum Design Magnetic Property Measurement System (MPMS). The samples (30 – 50 mg) were contained in gelatin capsules held in plastic straws. In a typical M vs. T experiment, Zero Field Cooled (ZFC) and Field Cooled (FC) data were measured from 2 K to 325 K using a magnetic field of 0.1 T. During the data collection 6 cm sample movement through the gradiometer coil was employed. All the measured data were corrected for core diamagnetism and the diamagnetic contribution from the gelatin capsules.

2.7. Solid State NMR[iii]

For $ScVO_{4-y}$ defect zircon, ^{51}V (157.8 MHz) and ^{45}Sc (145.7 MHz) NMR data were acquired on a Varian Inova 600 (14.1 T) spectrometer using a Varian-Chemagnetics MAS 3.2 mm double resonance X-H (F) probe. Finely ground samples (37 – 41 mg) were placed into a 3.2 mm (outer diameter) zirconia rotor (22 μL volume). ^{51}V MAS spectra were acquired using a single-pulse (Bloch) sequence spinning at 22000±5 Hz, collecting 256 co-added transients using a 22° tip angle (ν_{rf} = 54 kHz). ^{45}Sc MAS spectra were acquired as illustrated for vanadium using a 14° tip angle (ν_{rf} = 32 kHz). T_1 measurements were performed for ^{51}V using a saturation recovery sequence ($\{90°\}_n$-τ-90°) with a saturation comb of n = 24 pulses, spinning at 18000±3 Hz, using a 1.8 μs 90° pulse. The spectra were referenced to a 0.16 M solution of $NaVO_3$ (-574 ppm with respect to $VOCl_3$) and 0.1 M solution of $ScCl_3$ (0 ppm). Solid State NMR measurements were carried out by V. K. Michaelis.

[iii] Adapted with permission from 'Shafi, S. P.; Kotyk, M. W.; Cranswick, L. M. D.; Michaelis, V. K.; Kroeker, S.; Bieringer, M. Inorg. Chem. **2009**, 48, 10553-10559'. Copyright © 2009 American Chemical Society.

Chapter 3: Investigation of AVO_3 (A = Sc, In) Bixbyite Reactivity

The major part of the research work discussed in chapter 3: Results and Discussion-Part I encompasses the manuscript 'Formation, structure and magnetism of the metastable defect fluorite phases $AVO_{3.5+x}$ (A = In, Sc)' published in Journal of Solid State Chemistry, volume 180 (2007), pages 3333-3340.[iv]

All the experiments pertaining to this work except neutron powder diffraction data collection (by L. M. D. Cranswick) and magnetic measurements (by C. Bridges) were designed and conducted by S. P. Shafi. All the figures and manuscript drafts were prepared by S. P. Shafi and Dr. M. Bieringer. Dr. M. Bieringer and S. P. Shafi were responsible for the final editing of the manuscript.

The major part of the research work discussed in chapter 3: Results and Discussion-Part II encompasses the manuscript 'In Situ Powder X-ray Diffraction, Synthesis, and Magnetic Properties of the Defect Zircon Structure $ScVO_{4-x}$' published in Inorganic Chemistry, volume 48 (2009), pages 10553-10559.[v]

All the experiments except neutron powder diffraction data collection (by L. M. D. Cranswick) and magnetic measurements (by C. Bridges) were performed by S. P. Shafi and M. W. Kotyk. Solid state NMR experiments and data interpretation were

---

[iv] Based on "Journal of Solid State Chemistry, 180, Shafi, S. P.; Lundgren, R. J.; Cranswick, L. M. D.; Bieringer, M., Formation, structure and magnetism of the metastable defect fluorite phases $AVO_{3.5+x}$ (A = In, Sc), 3333-3340., Copyright © 2007, used with permission from Elsevier."

[v] Based on 'Shafi, S. P.; Kotyk, M. W.; Cranswick, L. M. D.; Michaelis, V. K.; Kroeker, S.; Bieringer, M. Inorg. Chem. **2009**, 48, 10553-10559'. Copyright © 2009 American Chemical Society.

carried out by V. K. Michaelis and Dr. S. Kroeker. All the figures except the one for solid state NMR (by V. K. Michaelis) were prepared by S. P. Shafi, M. W. Kotyk and Dr. M. Bieringer. S. P. Shafi and Dr. Bieringer were responsible for the manuscript draft preparations, revisions and final editing of the manuscript.

The chapter 3 contains additional data and expanded discussions. The electrical conductivity measurements were performed by Dr. V. Thangadurai.

Abstract

This chapter focuses on the investigation of AVO_3 bixbyite (A = In, Sc) reactivity under oxidative conditions and the identification as well as the characterization of the novel metastable phases observed. The entire reaction sequence regarding the bixbyite reactivity has been discussed in detail with emphasis on the structural modifications involved. The two step bixbyite oxidation pathway follows topotactic and reconstructive structural transitions. The reversibility of the oxidation – reduction cycle between AVO_3 bixbyite and AVO_4 zircon has been evaluated by means of in-situ techniques. The two novel metastable phases $AVO_{3.5+x}$ ($0.00 \leq x \leq 0.22$) defect fluorite and AVO_{4-y} defect zircon structures were identified and fully characterized. The structural and magnetic characteristics of these novel phases are discussed in detail.

3.1. Introduction

Understanding the solid state reaction pathways is important in order to probe the impact of structure on chemical reactivity. Chemical reactivity is often dictated by the structure as well as the constituent ions/atoms of the crystal structure. Such a feature is very prominent in the case of topotactic and topochemical reactions. Consequently, understanding the generalized chemical reactivity of structures allows one to tailor novel materials by altering the constituents accordingly. Investigation of bixbyite chemical reactivity under oxidation conditions is the major focus of Chapter 3. The study is prospective in terms of rational design of certain targeted compounds which are potential candidates for oxide ion conductivity. The candidates chosen for the study are AVO_3 (A = In, Sc) bixbyite structures. The A cations In^{3+} and Sc^{3+} are diamagnetic and hence V^{3+} is the only paramagnetic cation in the system. The wide range of possible oxidation states for vanadium allows access to a variety of structures which is highly beneficial for structure – reactivity studies and thereby for structure – property evaluations.

3.2. Results and Discussion – Part I

3.2.1. $InVO_3$ Bixbyite Reactivity under Oxidative Conditions

The AVO_3 perovskite series (A = Ln, Y) has been extensively studied over the years due to their intriguing structural and magnetic properties.[58-62] However, the AVO_3 bixbyite series is not so well understood compared to the perovskite series. $ScVO_3$ was first reported in 1967 by Reid and Sienko.[68] In 2004, Alonso et al. identified $ScVO_3$ bixbyite and the corresponding oxidation product $ScVO_{3.5}$ by means of ex-situ methods.[69] $InVO_3$ was not reported until 2006 which is surprising as the ionic radius of In^{3+} is

between Sc^{3+} and Lu^{3+} which is the end member of the perovskite AVO_3 series.[70] A previous report predicted $InVO_3$ to crystallize in a hexagonal structure with the space group *P6₃/mmc*.[96] The in-situ formation, strategy for the bulk synthesis and the magnetic properties of $InVO_3$ were reported in 2006 by Lundgren et al.[70] The synthesis of AVO_3 compounds except $InVO_3$ can be achieved through the high temperature reduction of the corresponding AVO_4 phases in H_2. $InVO_3$ cannot be synthesized through the high temperature reduction method due to the similar redox potential for $In \rightarrow In^{3+}$ and $V^{3+} \rightarrow V^{5+}$. During the reduction of $InVO_4$ under Ar/H_2 and Ar/CO atmospheres, $InVO_3$ was identified as a transient intermediate.[70] However, no phase pure $InVO_3$ was obtained under these conditions; both unreacted $InVO_4$ and over-reduced In metal were present in the reduction product.[70] The bulk synthesis strategy for $InVO_3$ was established by Lundgren, R. L. et al.[70] through in-situ x-ray diffraction experiments. They reported that the CO/CO_2 buffer gas provided a feasible atmosphere for pure $InVO_3$ synthesis. Bulk samples of $InVO_3$ can be synthesized by the reduction of $InVO_4$ under CO/CO_2 (1:1 ratio) at 450 °C for 12 hours. The in-situ powder x-ray diffraction experiments showed the onset of decomposition of metastable $InVO_3$ to In_2O_3 and V_2O_3 at 600 °C.[70]

The AVO_3 bixbyite phases crystallize in the cubic structure with space group $Ia\bar{3}$ (206) and the A^{3+}/V^{3+} cations occupy the *8b* and *24d* sites in a disordered fashion. $InVO_3$ bixbyite chemical reactivity during oxidation was followed using in-situ powder x-ray diffraction[97] from 25 to 800 °C in CO_2 and the temperature dependent contour plot is shown in figure 3.1. At T = 250 °C oxidation of $InVO_3$ occurs as indicated by the formation of new peaks and the diffraction peaks can be indexed on a cubic unit cell with space group $Fm\bar{3}m$. The peaks belonging to this phase persist till 450 °C with significant

shift to lower diffraction angles within this temperature range. The peak shifts are indicative of a large oxygen uptake and hence the composition of this phase is tentatively assigned as $InVO_{3.5+x}$. The formation of the fully oxidized $InVO_4$ zircon phase begins at 425 °C.

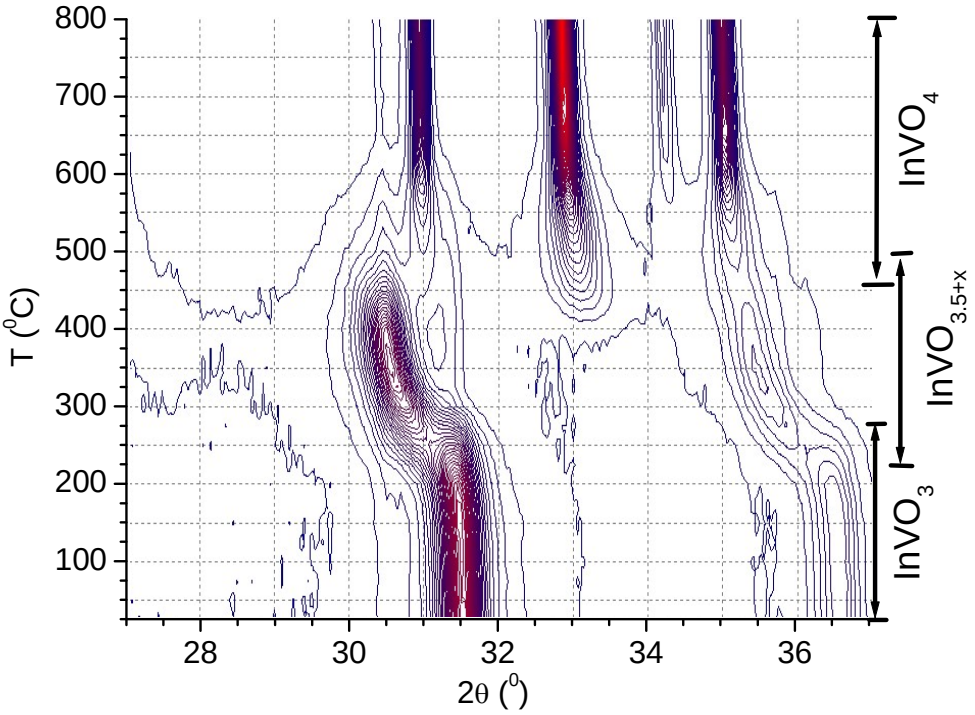

Figure 3.1. High temperature powder x-ray diffraction contour plot of $InVO_3$ oxidation in CO_2 from 25 to 800 °C with 25 °C increments. Intensities are shown as constant increment from lowest intensity blue to highest intensity red. Adapted from ref. 97.

Figure 3.2 shows the Rietveld refinement of the defect fluorite structure $InVO_{3.5+x}$ based on the powder x-ray diffraction data collected at 350 °C. The inset illustrates the fluorite structure with cations and anions represented by yellow and red spheres respectively. The peaks excluded in the refinement plot belong to the platinum strip

heater and the tiny shoulders on the high-angle side of the intense peaks are from the $InVO_3$ bixbyite starting material.

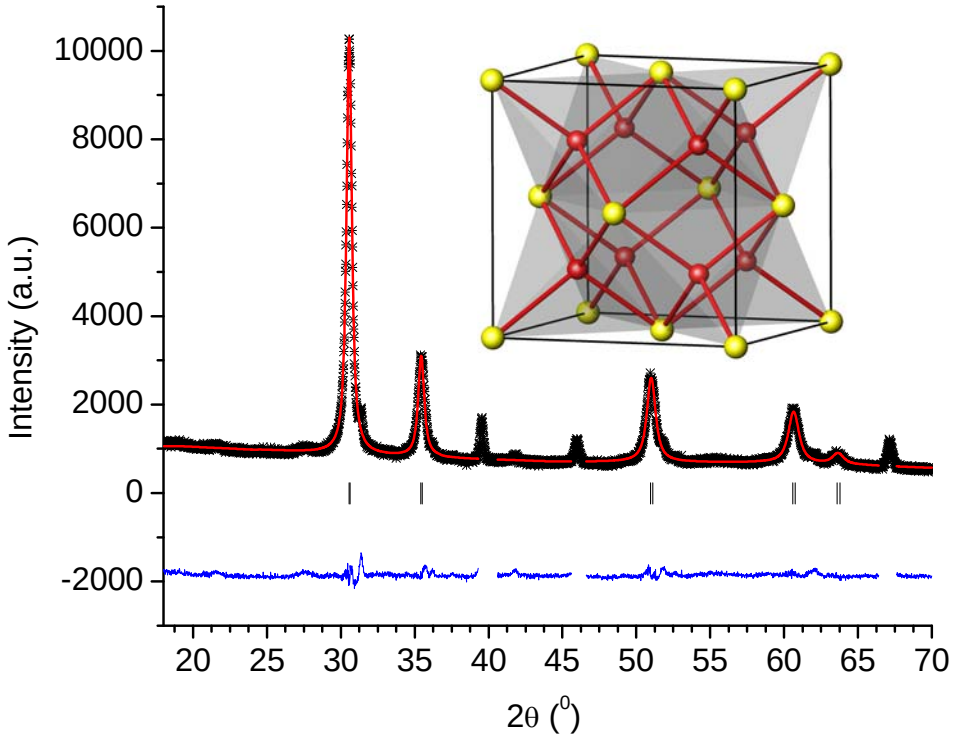

Figure 3.2. Rietveld plot of $InVO_{3.5+x}$ collected at 350 °C during the in-situ oxidation of $InVO_3$. Black symbols = experimental data, red line = best fit and blue line = difference. The Bragg peaks are represented by black solid tick marks and the excluded regions belong to platinum strip heater. The weak shoulders on the high 2θ angles of the intense peaks correspond to the unreacted starting material $InVO_3$. The inset shows the fluorite structure with the positions of cations and anions represented by yellow and red spheres respectively. Adapted from ref. 97.

The chemical reactivity of solids is closely linked to the presence of defects in the chemical structure. As a first approximation the defect fluorite structure $A^{3+}V^{4+}O_{3.5}$ comprises 12.5% of randomized oxide defects and the AVO_3 bixbyite structure can be considered as a fluorite structure with 25 % of ordered oxide defects. It is important to investigate the significance of these defects in determining the chemical reactivity of the

bixbyite and defect fluorite structures. The significant peak shifts to lower diffraction angles for the defect fluorite phase observed during the in-situ experiment were further explored with a control experiment. An in-situ x-ray diffraction experiment was conducted in dynamic vacuum (to avoid the oxidation of the defect fluorite phase) in order to probe the thermal expansion of $InVO_{3.54(1)}$. The unit cell parameters were determined through Rietveld refinements. The unit cell evolution of the $InVO_3$ (black solid triangles) and $InVO_{3.5+x}$ (blue hollow rectangles) phases during the in-situ oxidation of $InVO_3$ bixbyite as well as the thermal expansion of $InVO_{3.54}$ (red solid circles) are shown in figure 3.3 (lower panel) along with the $InVO_{3.5+x}$ phase fraction during the in-situ oxidation of $InVO_3$ bixbyite in figure 3.3 (upper panel).

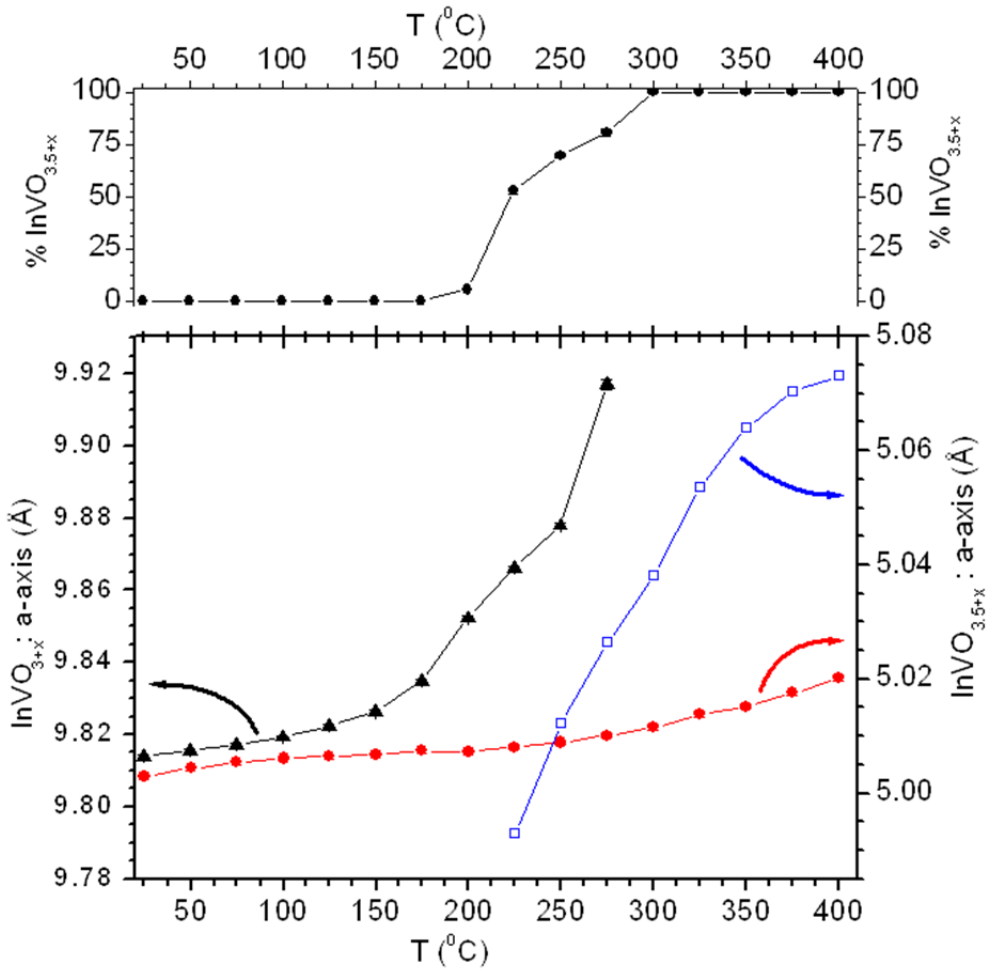

Figure 3.3. (LOWER PANEL) Unit cell parameter evolution of $InVO_3$ (black solid triangles) and $InVO_{3.5+x}$ (hollow blue squares) during the in-situ oxidation. The thermal expansion of $InVO_{3.54}$ conducted in dynamic vacuum is shown as solid red circles representing the unit cell evolution of $InVO_{3.54}$. (UPPER PANEL) The phase fraction of $InVO_{3.5+x}$ during in-situ oxidation of $InVO_3$.[97]

The unit cell evolution of $InVO_3$ up to T = 150 °C is almost linear suggesting thermal expansion in that temperature interval. The sudden increase in slope above 150 °C indicates oxygen uptake in the $InVO_3$ structure. The onset of the $InVO_{3.5+x}$ defect fluorite phase was first observed at 225 °C and the cubic unit cell lattice parameter increases substantially up to 400 °C. The slope of the unit cell parameter evolution of $InVO_{3.5+x}$ formed during the in-situ oxidation is considerably larger than that during the

thermal expansion of $InVO_{3.54}$ and reinforces our earlier prediction of large oxygen uptake. The uptake of a wide range of oxygen illustrates the significance of defects in the chemical reactivity of these structures. The filling of defects in turn governs the co-ordination environment of the cations, and consequently the structure and reactivity.

3.2.2. Synthetic Strategies Based on Bixbyite Reactivity and TGA – DTA Analysis

So far we have discussed the chemical reactivity of bixbyite, the in-situ formation of $InVO_{3.5+x}$ and the opportunity for controlling vanadium oxidation states through controlled oxygen uptake in the defect fluorite system. The following section discusses the strategies for the bulk synthesis of the $InVO_{3.5+x}$ defect fluorite structure. Bulk samples of $InVO_{3.5+x}$ can be prepared by the oxidation of $InVO_3$ under a CO_2 atmosphere at 350 °C. $InVO_3$ bixbyite in the form of a pellet under this condition did not give any appreciable amount of $InVO_{3.5+x}$. Successful oxidation was only observed when the starting material was reacted as a thin layer. Figure 3.4 compares the powder x-ray diffractograms of pristine $InVO_3$ and the oxidation products obtained from the pelletized and thin layer samples.

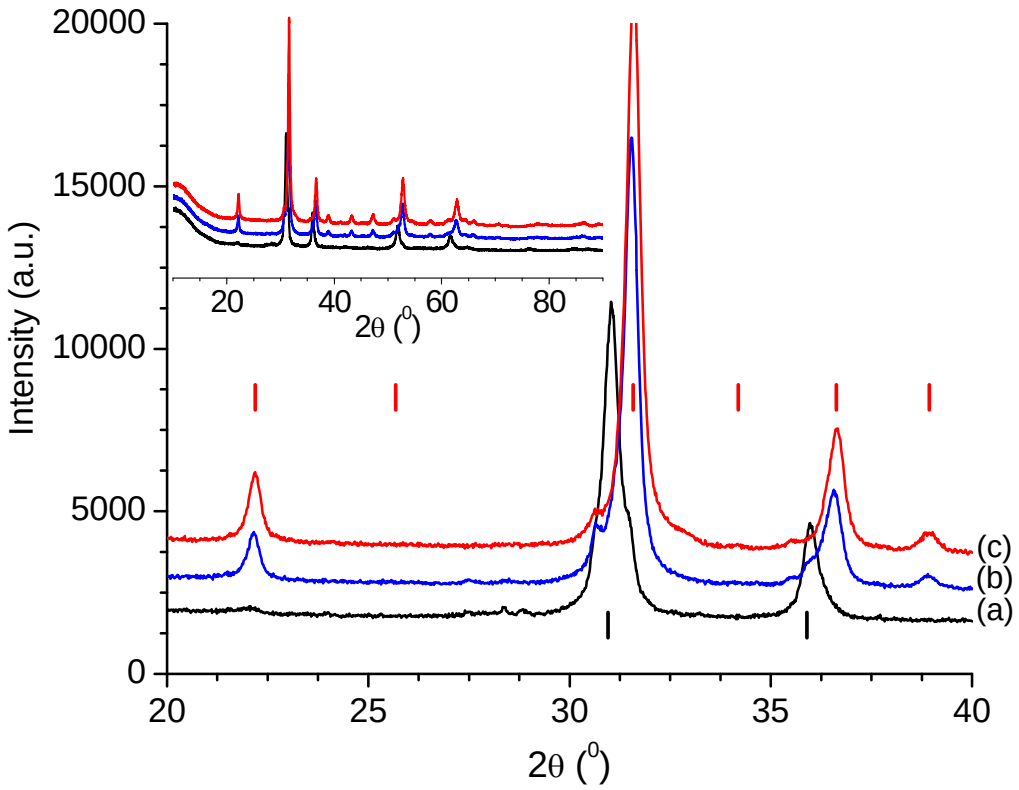

Figure 3.4. Powder x-ray diffractograms of (a) oxidation product of the thin layer $InVO_3$ sample, (b) oxidation product of pelletized $InVO_3$ and (c) unreacted $InVO_3$ bixbyite. The lower and upper tick marks belong to the $InVO_{3.5}$ and $InVO_3$ Bragg positions respectively. Adapted from ref. 97.

$InVO_3$ needs to be treated under mild oxidation conditions to form $InVO_{3.5}$. Oxidation in air or oxygen resulted in the formation of considerable amounts of fully oxidized $InVO_4$ impurities. There were considerable peak shifts among the different $InVO_{3.5+x}$ samples prepared which is consistent with the previously mentioned shift to the low diffraction angles of the defect fluorite peaks during the in-situ formation. Thermogravimetric analysis was carried out to estimate the oxygen stoichiometry in a variety of $InVO_{3.5+x}$ samples. Simultaneous thermogravimetric (TGA)/differential thermal (DTA) analysis of $InVO_3$ oxidation was carried out in an oxygen flow according to Eq. 3.1.

$2\ InVO_{3.5+x} + (½ - x)\ O_2 \rightarrow 2\ InVO_4$ (Eq.3.1)

Figure 3.5 shows the TGA and DTA traces as red and blue lines respectively. Two distinct peaks were observed in the DTA trace indicative of two oxidation steps, $InVO_3 \rightarrow InVO_{3.5+x}$ and $InVO_{3.5+x} \rightarrow InVO_4$. Similarly two strongly overlapping features were observed in the TGA trace with the first step significantly larger than the value expected for the formation of the defect fluorite phase. Note that the reaction was carried out in oxygen and previously we have seen that during the bulk synthesis in oxygen the product contained $InVO_4$ impurities. The results from the TGA experiments on thin sample layers under a CO_2 atmosphere were inconclusive due to the small sample mass.

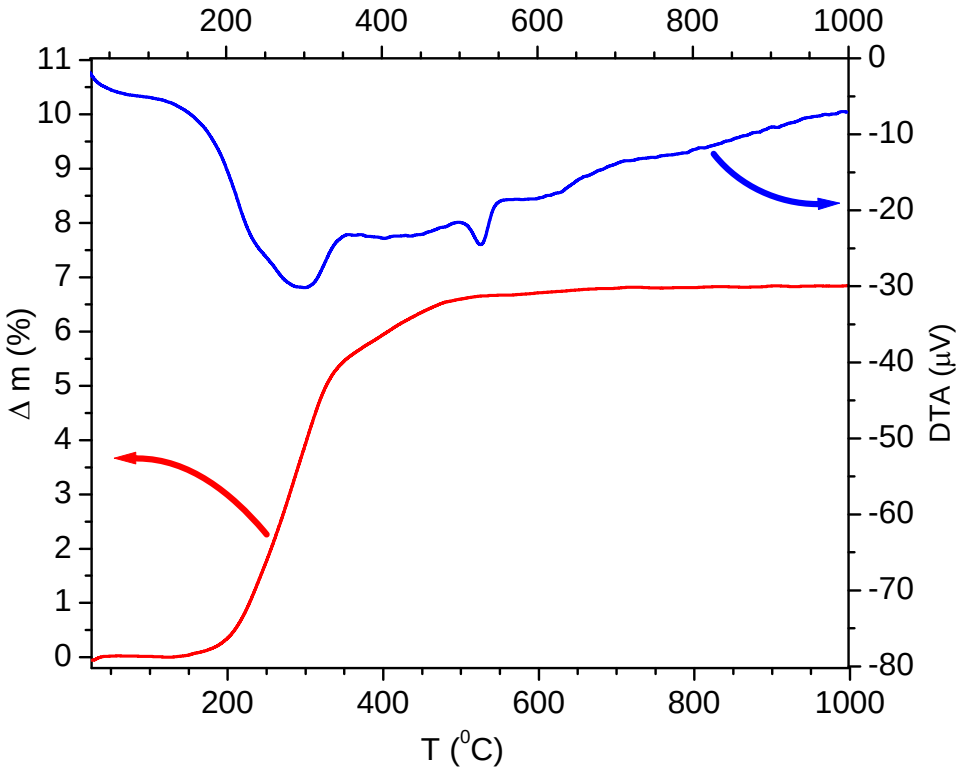

Figure 3.5. Thermogravimetric analysis (red) and differential thermal analysis (blue) traces of $InVO_3$ bixbyite oxidation using a heating rate of 10 °C/min. in oxygen. Adapted from ref. 97.

The experiments showed the possible range of oxygen stoichiometry for the defect fluorite structure $InVO_{3.5+x}$. The oxygen concentration for $InVO_{3.5+x}$ was found to vary from $InVO_{3.50(2)}$ to $InVO_{3.72(2)}$. The cubic unit cell parameter for $InVO_{3.5+x}$ increased monotonically with increasing oxygen content. The cubic unit cell parameter determined by the Rietveld refinements of the powder x-ray diffraction data is compared with the oxygen content in $InVO_{3.5+x}$ in figure 3.6.

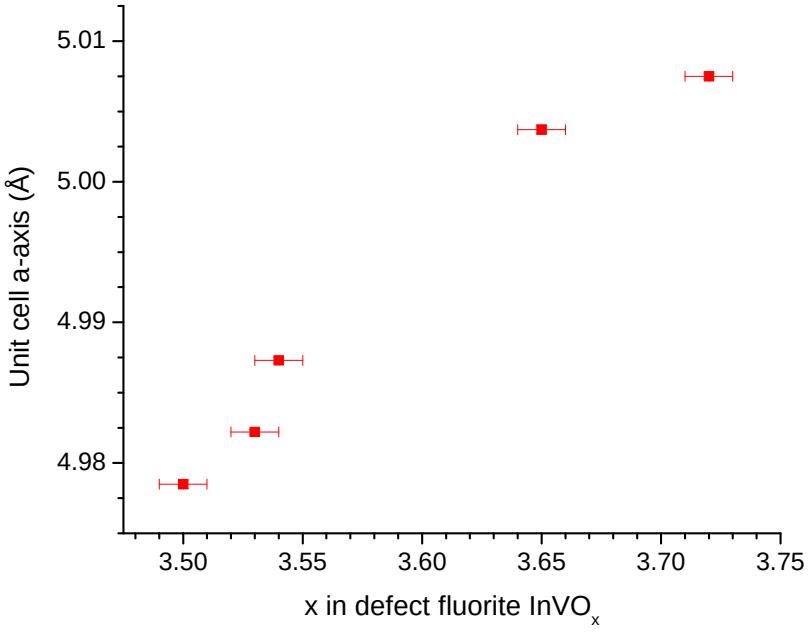

Figure 3.6. Cubic unit cell parameter of the defect fluorite phase $InVO_x$ as a function of oxygen stoichiometry x.

3.2.3. Structural Analysis of $InVO_{3.5+x}$

Investigation of the $InVO_3$ bixbyite reactivity yielded the identification of the novel metastable phase $InVO_{3.5+x}$. The detailed structure of $InVO_{3.5+x}$ was investigated by combined powder x-ray and neutron diffraction. Neutrons are far more sensitive than x-rays to oxygen and hence are a better probe for examining the oxygen sublattice. As mentioned previously $InVO_{3.5+x}$ crystallizes in the cubic structure in space group $Fm\bar{3}m$ (225) with In^{3+}/V^{4+} disorder on the *4a* (0,0,0) site. The oxygen anions are located on the *8c* (¼, ¼, ¼) site with the defect concentration varying from 12.5 to 7.5 % for $InVO_{3.5}$ and $InVO_{3.7}$ respectively. The oxygen content of the bulk samples used for the diffraction experiments was determined by thermogravimetric analysis. Rietveld refinements were carried out against one powder x-ray diffraction and one powder neutron diffraction data set collected at room temperature. A total of 14 parameters for $InVO_{3.54(1)}$ including neutron wavelengths, unit cell parameter, scale factor, zero points, peak shape parameters and Debye-Waller temperature factors were refined. During the initial cycles the backgrounds were fitted using a cubic spline and were fixed for the subsequent cycles. The room temperature Rietveld plots for $InVO_{3.54(1)}$ are shown in figure 3.7. The Rietveld refinement results are listed in table 3.1. A particularly large oxygen temperature factor of 16(2) $Å^2$ was observed for $InVO_{3.54(1)}$. This is due to the large oxygen defect concentration of 11.5 % for $InVO_{3.54(1)}$.

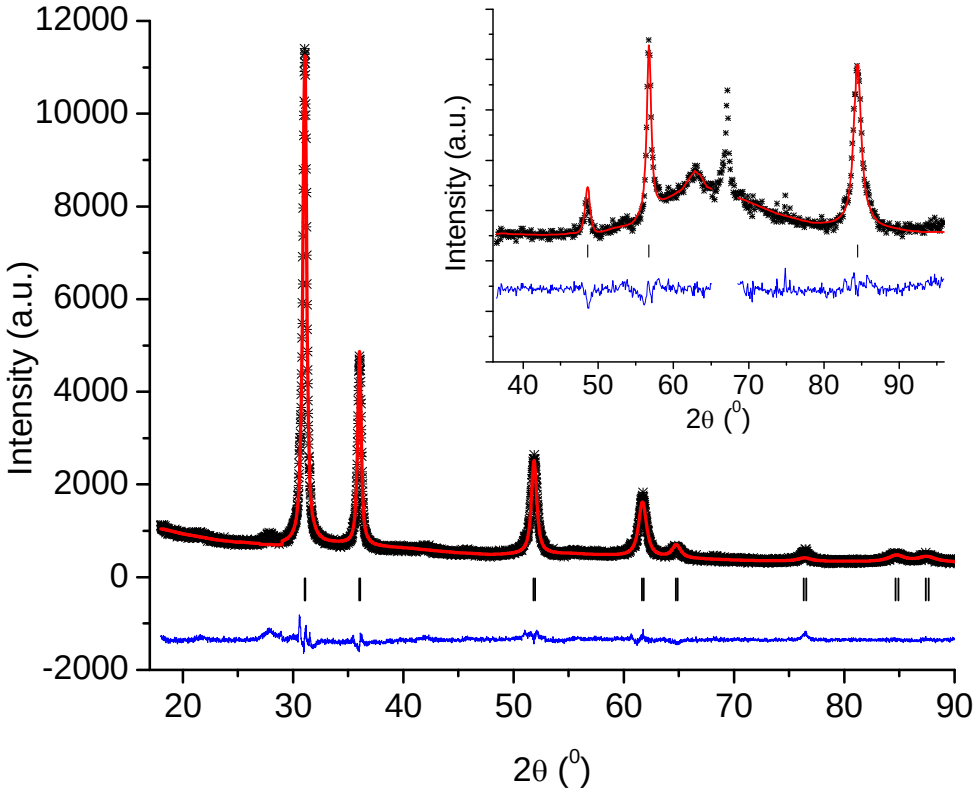

Figure 3.7. Rietveld plots of $InVO_{3.54(1)}$ based on Rietveld refinements against one x-ray and one neutron diffraction dataset. The powder x-ray diffraction data were collected with $CuK\alpha_{1,2}$ (λ = 1.540598, 1.544426 Å) radiation and the powder neutron data shown in the inset were collected with λ =2.3700(9) Å. The excluded region in the neutron diffraction data (inset) belongs to the (1 1 0) reflection from the vanadium sample container. Black symbols = experimental data, red line = best fit, blue line = difference, black tick marks = Bragg positions. Adapted from ref. 97.

Table 3.1. Crystallographic details for $InVO_{3.54}$ at room temperature from Rietveld refinements against one x-ray and one neutron diffractogram. XRD* = powder x-ray diffraction pattern with λ= 1.540598 Å, 1.544426 Å, weight in refinement = 0.6; NPD** = powder neutron diffraction data with λ = 2.3700 (9) Å, weight in refinement = 0.4.

space group		$Fm\bar{3}m$		
a (Å)		4.9863(5)		
V(Å^3)		123.99(2)		
Z		2		
	site	**frac. occ.**	**B_{iso}(Å^2)**	
A^{3+}	*4a*	½	2.9(2)	
V^{4+}	*4a*	½	2.9(2)	
O	*8c*	0.885	16(2)	
		R_p	**R_{wp}**	**χ^2**
XRD*		4.57	5.97	2.51
		4781 data points		
NPD**		2.46	3.42	7.17
		795 data points		
parameters			14	

The diffraction peaks were considerably broadened indicative of small crystalline domain sizes. It should be noted that the synthesis was carried out at low temperatures in order to avoid further oxidation. The crystalline domain sizes were calculated using the Scherrer equation (Eq. 3.2).

$$D = 0.9\,\lambda/B\cos\theta, \qquad \text{(Eq.3.2)}$$

where D is the crystalline domain size, λ the wavelength, B the integral breadth and θ the diffraction angle. The crystalline domain size for $InVO_{3.54(1)}$ was estimated to be 225 (50) Å. In addition, the defect fluorite phase $InVO_{3.54(1)}$ showed a broad background feature in the neutron powder diffraction data at $d \approx 2.13$ Å corresponding to domain sizes of 20 Å indicating a structural component with a fairly small coherence length. Note that such a feature was observed only in the neutron diffraction pattern and not in the x-ray diffraction pattern. We propose that this feature is representative of oxide defect clustering.

3.2.4. Magnetic Properties of the $InVO_{3.5}$ Defect Fluorite Phase

D.c. magnetic susceptibility measurements were carried out on the $InVO_{3.54}$ defect fluorite phase. The high temperature paramagnetic data regime was fitted with the Curie-Weiss law modified with a temperature independent term, Eq.3.3 where χ is the magnetic susceptibility, C the Curie constant, T the temperature, θ the Weiss temperature and α the temperature independent term. All the measured data were corrected for diamagnetism.

$$\chi = C/(T - \theta) + \alpha \qquad \text{(Eq.3.3)}$$

Figure 3.8 shows the χ vs. T and χ^{-1} vs. T plots for the magnetic data collected for $InVO_{3.54}$. Note that both the zero-field cooled (ZFC) and field cooled (FC) d.c. susceptibility data superimpose, indicating no phase transition. From the Curie-Weiss fit, a Curie constant of C = 0.355 (1) emu K mol^{-1} was obtained for $InVO_{3.54}$ which is consistent with the spin-only Curie constant of 0.374 emu K mol^{-1} for V^{4+}. The Curie constant for V^{3+} and V^{5+} in a 1:1 ratio would be C = 0.5 emu K mol^{-1}. The expected spin-

only magnetic moment for V^{4+} is 1.73 μ_B. The effective magnetic moment for V^{4+} in $InVO_{3.54}$ was calculated to be 1.75 (1) μ_B. The Weiss temperature was calculated to be -2.9(8) K indicating weak overall antiferromagnetic coupling. The near zero value for Weiss-constant indicates negligible spin-spin interactions or cancelling antiferromagnetic and ferromagnetic interactions.

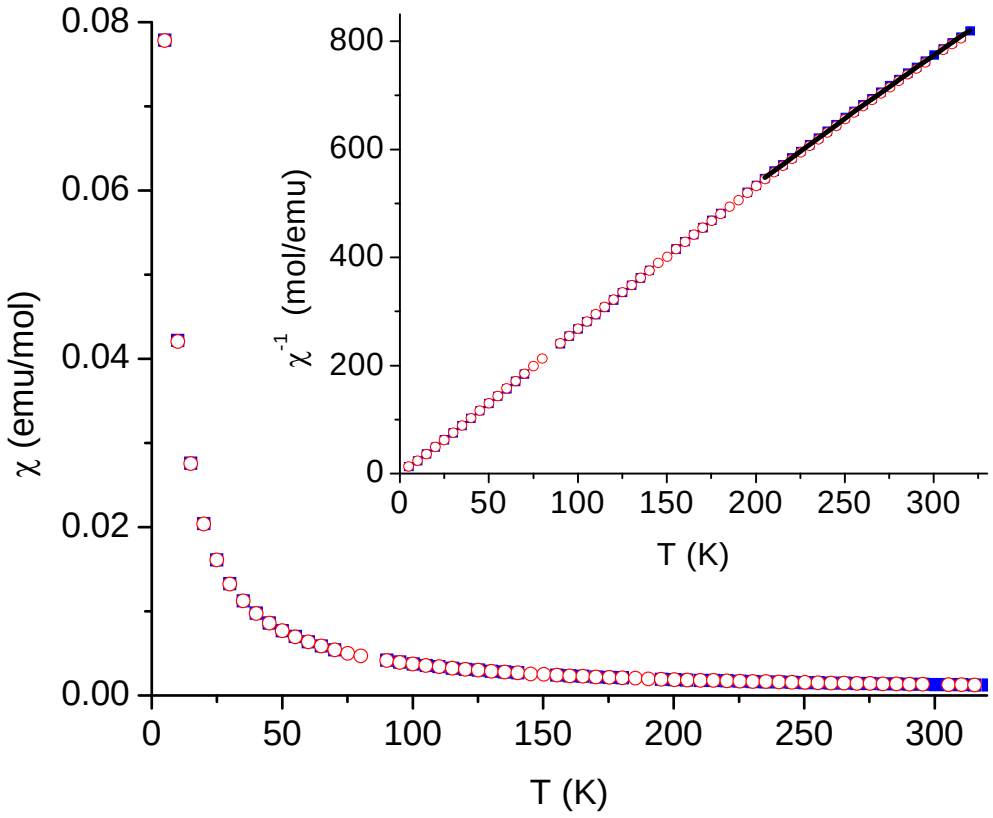

Figure 3.8. D.c. magnetic susceptibility data measured for $InVO_{3.5}$ at low temperature with a magnetic field of H = 0.1 T. Adapted from ref. 97.

Low temperature powder neutron diffraction data were collected for $InVO_{3.54(1)}$ and are compared with the room temperature data in figure 3.9. The low temperature data are consistent with the cubic unit cell with space group $Fm\bar{3}m$. The only features in the difference plot (black) are due to the unit cell contraction upon cooling. No peaks due to

magnetic long range ordering were observed at 3 K. $InVO_{3.5}$ contains V^{4+} ions with S = ½ and the structure shows bond disorder due to In^{3+}/V^{4+} disorder. Hence there is a possibility for a spin-glass or spin liquid ground state. However, no significant ZFC – FC divergence was observed for $InVO_{3.54}$. A more detailed investigation of the low temperature magnetic ground state is required. Heat capacity and a.c. susceptibility measurements can be used to further investigate the low temperature magnetic ground state for $InVO_{3.54}$.

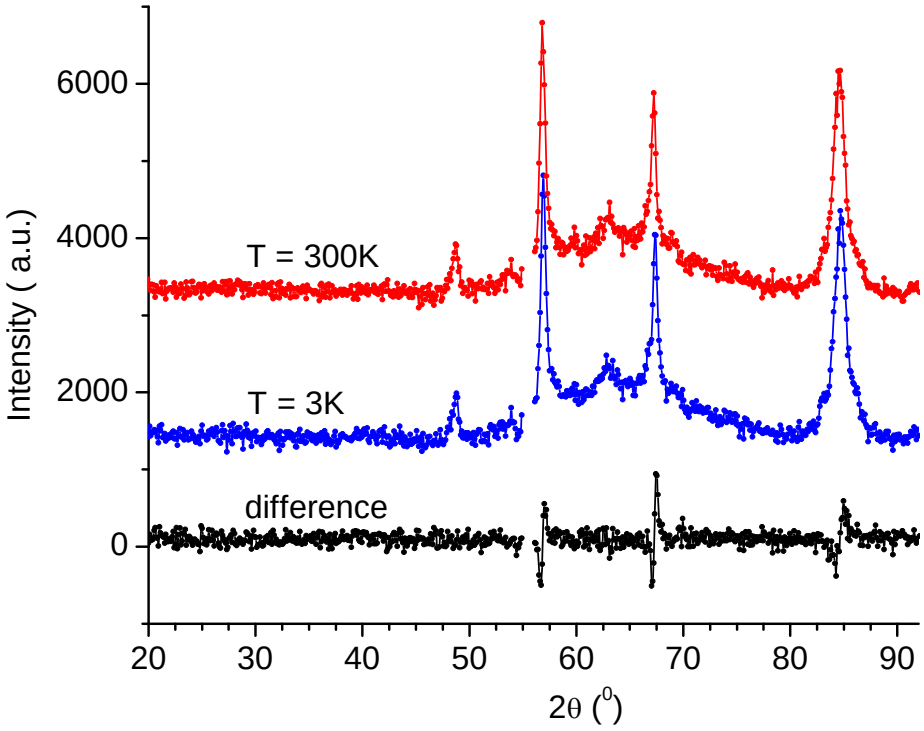

Figure 3.9. The powder neutron diffraction patterns of $InVO_{3.54}$ collected with a wavelength of λ = 2.37 Å at T = 300 K (red) and 3 K (blue). The black pattern at the bottom represents the difference (3 – 300 K). Adapted from ref. 97.

3.2.5. Structural Aspects of the Bixbyite Oxidation

The structural transformations occurring during the $InVO_3$ bixbyite oxidation pathway are very significant as the intermediate phases are of potential interest for oxide ion conductivity because of the oxide ion defects in the structure. The fragments of the oxide defect structures significant to this project are illustrated schematically in figure 3.10.

In the cubic fluorite structure the cations form a cubic close packed structure with anions occupying the tetrahedral interstitials. Removal of one out of the eight oxide ions in an ordered fashion would result in a pyrochlore structure (figure 3.10.b) and removal of two oxide anions across the body diagonal would result in a bixbyite structure (figure 3.10.c). The bottom panel in figure 3.10 compares the oxide defect structural fragments with the idealized fluorite structure analogues.

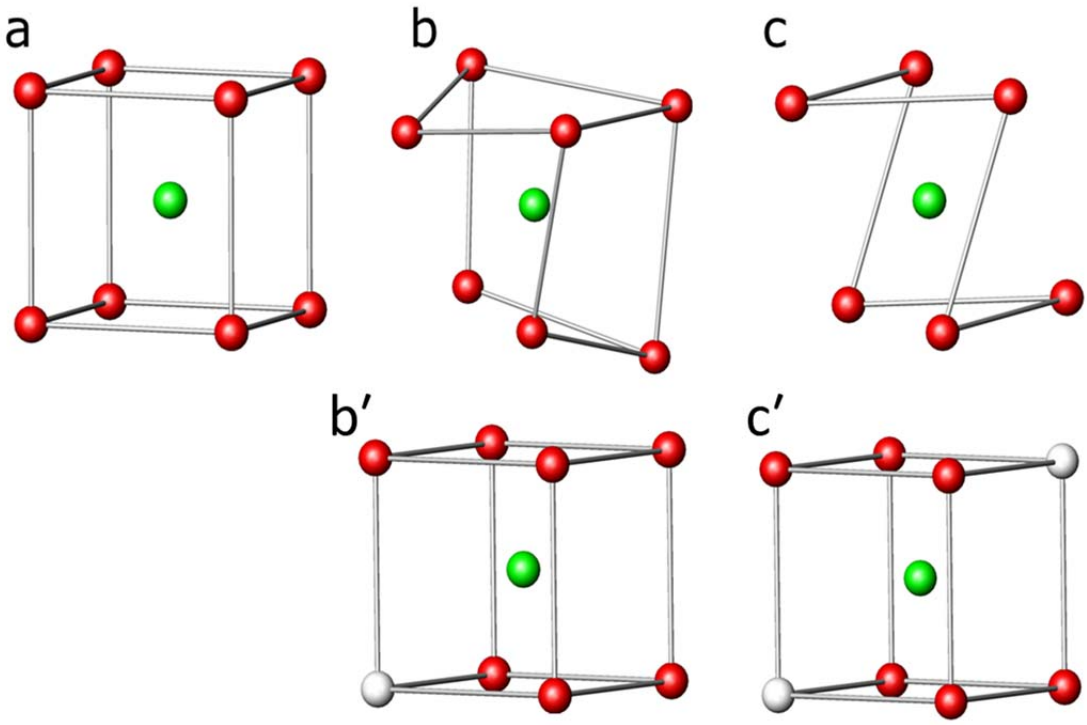

Figure 3.10. Schematic illustration of (a) fluorite, (b) pyrochlore and (c) bixbyite structural fragments. The cation and anion positions are represented by green and red spheres respectively. The pyrochlore structure has one oxide defect for eight oxide anions and shows vacancy ordering whereas the bixbyite structure has two oxide vacancies for eight oxide anions. The bottom panel compares the actual structural fragments (b and c) to the idealized fluorite structure analogues (b′ and c′). The connecting lines are only a guide to the eye. Adapted from ref. 97.

The first oxidation step from $InVO_3$ bixbyite to $InVO_{3.5}$ defect fluorite is topotactic in nature; substantial atomic connectivity in the starting material is retained in the product formed. The topotactic oxidation step proceeds through the statistical addition of an oxygen atom to one of the two oxide vacancy sites of the bixbyite structure. During this step the ion mobility is limited to the oxygen sublattice, the cation sublattice stays intact without any major changes. The subtle changes in the cation positions during this structural transition are explained later in this chapter (section 3.3.3, figure 3.17). Further oxidation results in the formation of a pentavalent vanadium cation which is too small to

be in a 7 or 8-fold coordinated environment. During this second oxidation step the cations A^{3+} and V^{5+} order with the smaller pentavalent V^{5+} occupying the tetrahedral environment in the zircon structure.

3.3. Results and Discussion – Part II

3.3.1. $ScVO_3$ Bixbyite Reactivity under Oxidative Conditions

In the first part of this chapter the reactivity of $InVO_3$ bixbyite and the associated structural modifications through controlled oxygen addition have been discussed in detail. The previous study of another promising candidate belonging to this series $ScVO_3$ bixbyite and $ScVO_{3.5}$ defect fluorite were carried out ex-situ.[69] Often, ex-situ methods are prone to missing significant intermediates especially those which are metastable and the entire chemical reactivity sequence cannot be fully understood. The aptness of in-situ methods in investigating the bixbyite reactivity and the insights gathered from it motivated us to explore the $ScVO_3$ bixbyite reactivity further.

The $ScVO_3$ oxidation pathway in oxygen was followed with in-situ x-ray diffraction and simultaneous thermogravimetric/differential thermal analysis.[98] Figure 3.11 and figure 3.12 show the in-situ x-ray diffraction contour plot and TGA/DTA data of $ScVO_3$ oxidation in oxygen respectively.

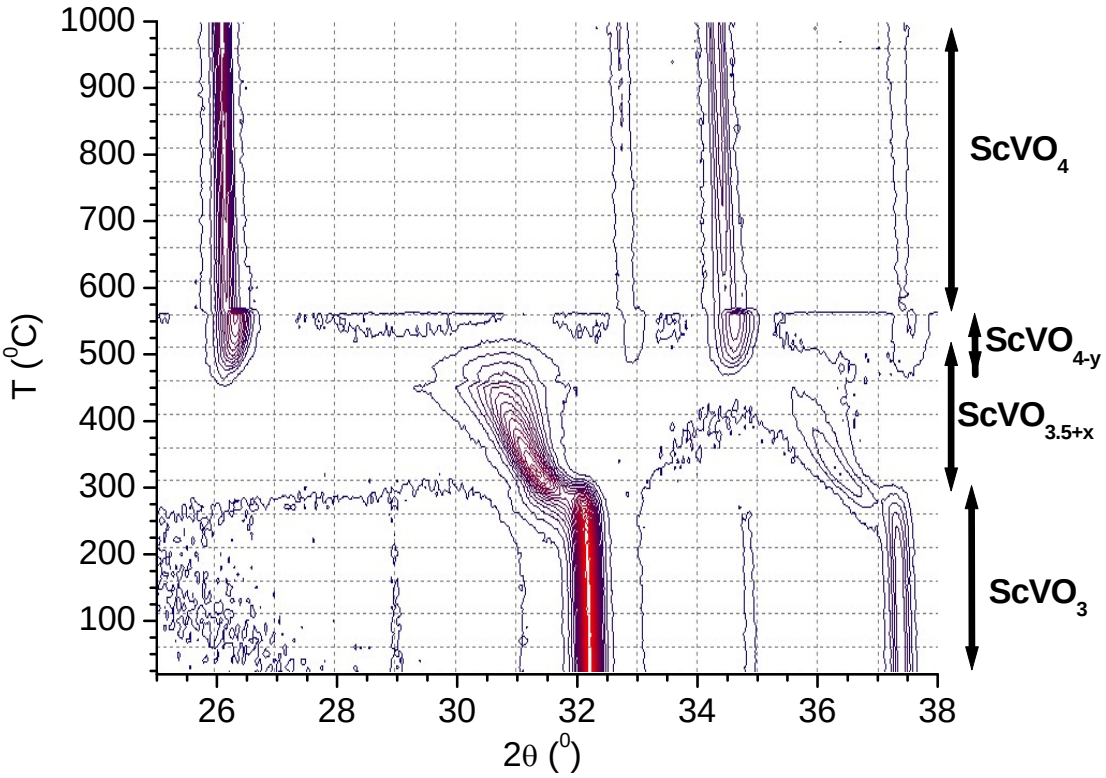

Figure 3.11. High temperature powder x-ray diffraction contour plot of $ScVO_3$ oxidation in oxygen from 30 to 1000 °C with 10 °C increments. Intensities are shown as constant increment from lowest intensity blue to highest intensity red.[98]

During the oxidation process two distinct intermediates can be seen in the in-situ x-ray diffraction contour plot shown in figure 3.11 prior to the formation of fully oxidized $ScVO_4$ zircon structure. Most of the features in the contour plot are analogous to the $InVO_3$ bixbyite oxidation pathway which includes the formation of the $AVO_{3.5+x}$ defect fluorite phase and the fully oxidized AVO_4 zircon phase. The first oxidation step resulting in the formation $ScVO_{3.5+x}$ ($0 \leq x \leq 0.22$) has been discussed in detail in the first part of this Chapter. This is evident in figure 3.11 from the disappearance of the bixbyite peaks and the appearance of the defect fluorite peaks at T ≈ 300 °C. The defect fluorite structure $ScVO_{3.5+x}$ ($0 \leq x \leq 0.22$) crystallizes in the $Fm\bar{3}m$ (225) space group with the

cations Sc^{3+}, (1-2x) V^{4+} and (2x) V^{5+} occupying the *4a* site in a disordered fashion. Also, the peaks belonging to this phase shift considerably to lower 2θ angles indicative of large oxygen uptake similar to $InVO_{3.5+x}$. The exothermic peak A in the DTA trace and the corresponding mass gain in the TGA trace shown in figure 3.12 are consistent with this first oxidation step. At T ≈ 450 °C, the defect fluorite phase disappears which is accompanied by the formation of another phase that can be indexed on a tetragonal unit cell with space group $I4_1/amd$. Previously it has been observed that the fully oxidized AVO_4 zircon structure crystallizes in the tetragonal structure with space group $I4_1/amd$. There is a clear shift of peaks to lower 2θ angles at T > 570 °C. The shift was observed within a temperature and time range of 10 °C and 20 minutes respectively. No indication of a change in space group was observed during this transition suggesting that the phase existing in the temperature range 450 ≤ T ≤ 570 °C is an oxygen deficient zircon structure and can be tentatively denoted $ScVO_{4-y}$. Notably, the peaks belonging to the $ScVO_{4-y}$ phase are significantly broader than the fully oxidized zircon structure peaks due to the presence of defects resulting in limited crystallinity. The exothermic peak B and the associated mass gain in figure 3.12 are in agreement with this second oxidation step.

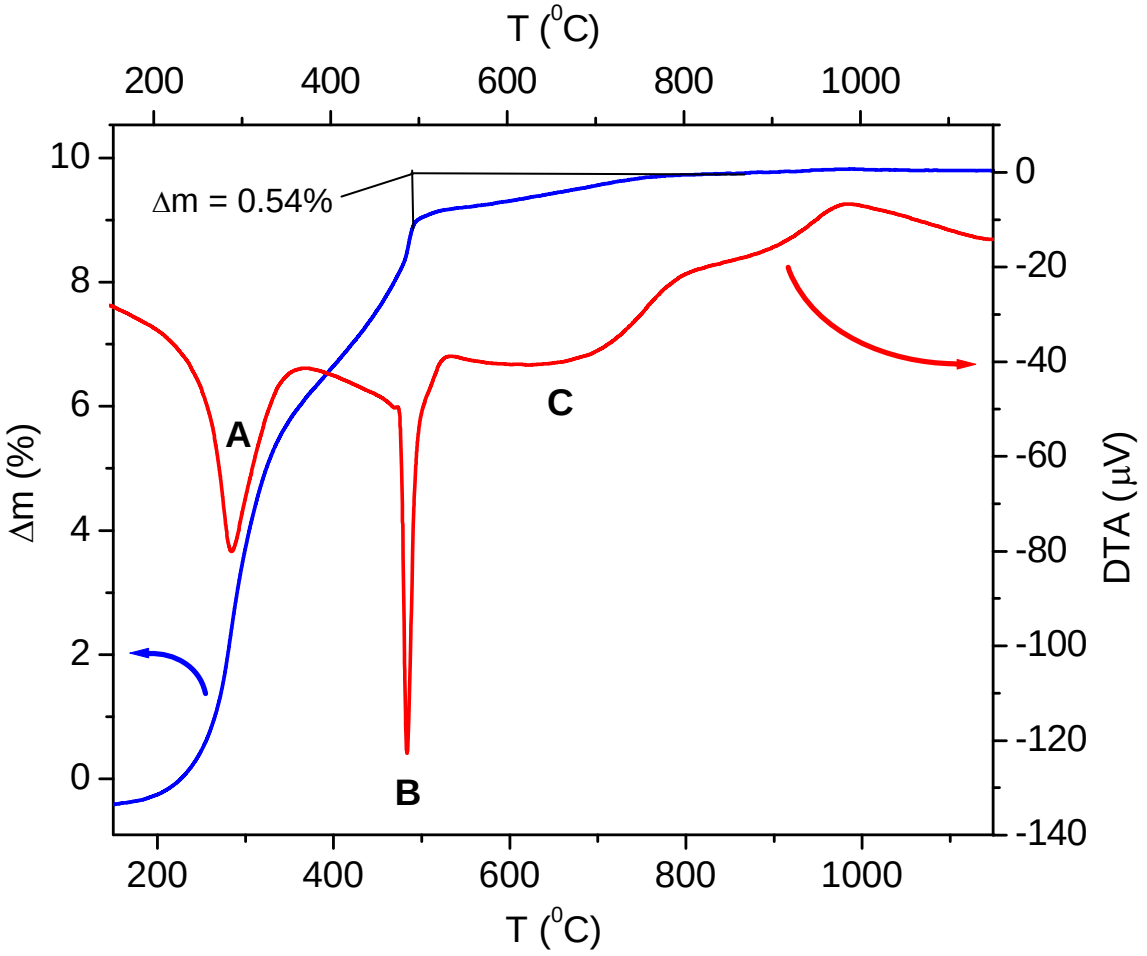

Figure 3.12. Thermogravimetric analysis (blue) and differential thermal analysis (red) traces of $ScVO_3$ bixbyite oxidation using a heating rate of 25 °C/min. in oxygen. Adapted from ref. 98.

A mass gain of 0.54 % and a broad exothermic peak C was observed in the TGA/DTA plot between 500 and 750 °C. This indicates further oxygen uptake during the final oxidation step. It should be noted that this additional oxygen uptake occurs over a wide temperature range during the TGA/DTA experiment due to a fast heating rate whereas this occurs in a relatively narrow temperature range during the in-situ powder x-ray diffraction experiment due to slow heating. In short the $ScVO_3$ bixbyite reactivity sequence can be summarized as $ScVO_3 \rightarrow ScVO_{3.5+x}$ $(0 \leq x \leq 0.22) \rightarrow ScVO_{4-y}$ $(0.0 < y$

$\leq 0.1) \rightarrow ScVO_4$. The mass gain of 0.54 % associated with the final oxidation step indicates the composition of the second intermediate phase to be $ScVO_{3.91(2)}$. On revisiting the figure 3.1 contour plot showing the $InVO_3$ oxidation, one could clearly see the broad peak at $2\theta \approx 33°$ for the temperature range 425 to 500 °C. This could very well be due to the formation of $InVO_{4-y}$. Also, as mentioned previously, the TGA trace for $InVO_3$ oxidation in oxygen (figure 3.5) showed two strongly overlapping features with the first step significantly larger than the value expected for the formation of the defect fluorite phase. This is consistent with the appearance of $InVO_4$ impurities when the synthesis of $InVO_{3.5}$ was carried out in air. There is a possibility for the existence of $InVO_{4-y}$, however this was not traceable predominantly due to lack of control for controlled oxidation in comparison to $ScVO_3$ oxidation. Also note that $InVO_{3.5}$ synthesis required oxidation of thin layers of $InVO_3$ in a CO_2 atmosphere.

3.3.2. Strategy for Bulk Synthesis and Structural Characteristics of $ScVO_{4-y}$

The direct synthesis of $ScVO_{4-y}$ by oxidation of $ScVO_3$ bixbyite always resulted in significant amounts of $ScVO_{3.5+x}$ impurities. In order to prepare phase pure $ScVO_{4-y}$, the defect fluorite $ScVO_{3.5+x}$ needs to be used as the starting material. The oxygen content in the defect zircon phase was identified using TGA under oxidizing conditions and the composition was confirmed to be $ScVO_{3.94(2)}$. In addition, each of the samples was of distinct color. The contrasting sample colors are compared in figure 3.13; $ScVO_{3.5+x}$ is black, $ScVO_{3.94(2)}$ is yellowish brown and $ScVO_4$ is cream colored.

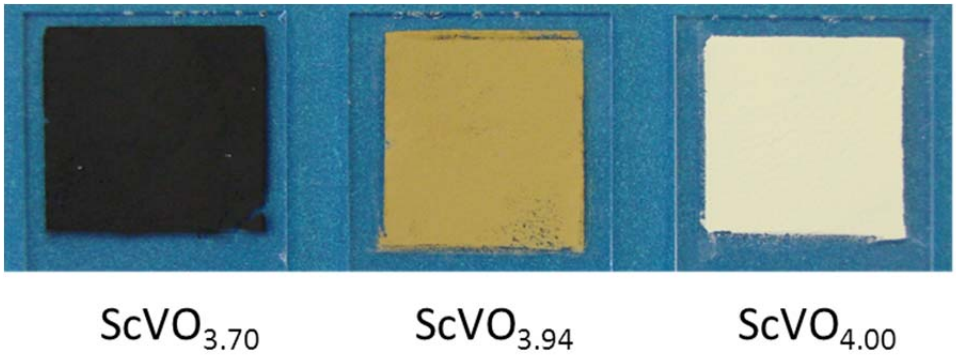

Figure 3.13. Comparison of $ScVO_{3.70}$ (black), $ScVO_{3.94}$ (beige) and $ScVO_{4.00}$ (cream) sample colors. Adapted from ref. 98.

The crystallographic details of $ScVO_{4-y}$ were deduced from the Rietveld refinements against one powder x-ray and two neutron diffraction datasets collected at room temperature. The crystallographic structure was identified to be the zircon structure with realistic bond lengths and structural parameters. The refined parameters include neutron wavelengths, unit cell parameter, scale factor, zero points, peak shape parameters, atomic coordinates and temperature factors. The Rietveld plots are shown in figure 3.14 and the structural details are provided in table 3.2.

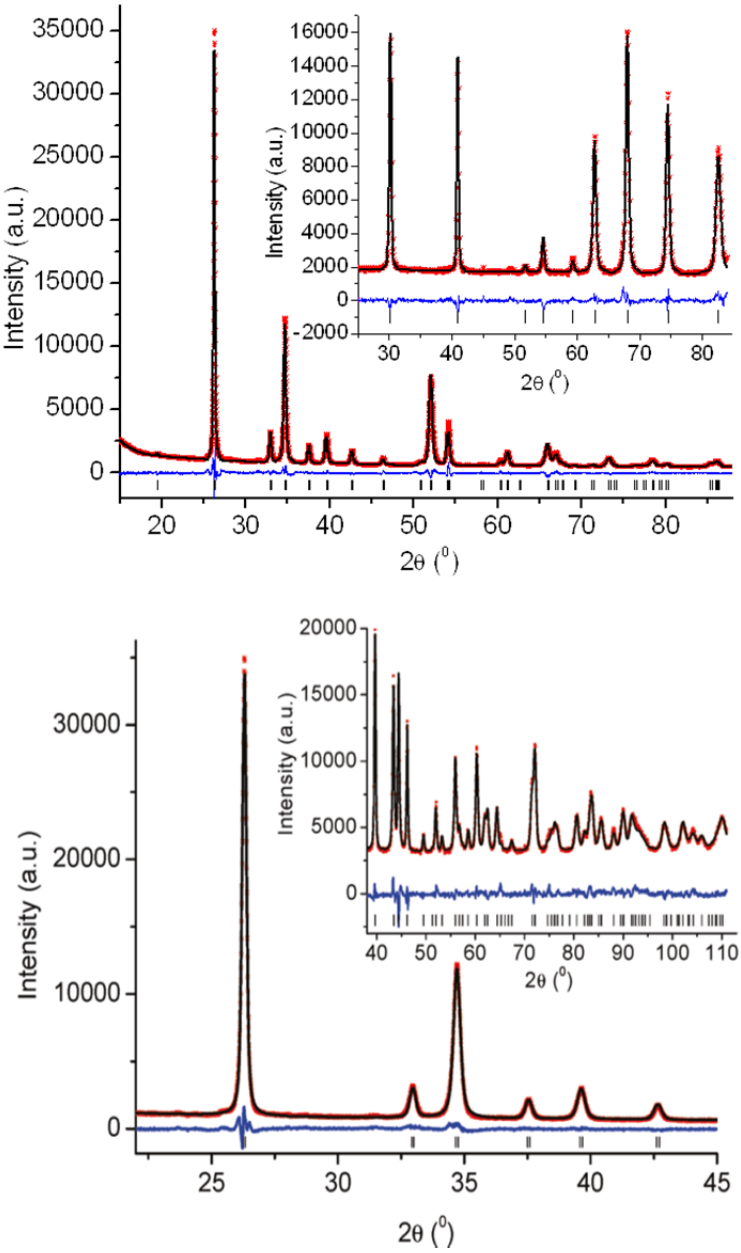

Figure 3.14. Rietveld plots of the $ScVO_{3.94}$ room temperature refinement. (TOP) The powder x-ray diffraction data were collected with $CuK\alpha_{1,2}$ (λ = 1.540598, 1.544426 Å) radiation and powder neutron data (inset) with λ =2.37126 (5) Å. (BOTTOM) Low angle portion of the powder x-ray diffraction data with Cu $K\alpha_{1,2}$ radiation and powder neutron diffraction data (inset) with short wavelength λ =1.32967 (2) Å. Red crosses = experimental data, black line = best fit, blue line = difference and black tick marks = Bragg positions. Adapted from ref. 98.

Table 3.2. Room temperature structural parameters, bond angles and average bond distances for the $ScVO_{4-y}$ defect zircon phase as obtained from Rietveld refinements against one x-ray and two neutron diffraction data. Sc^{3+} is located on site 4a (0, ¾, 1/8) and V^{5+} on 4b (0, ¼, 3/8).

T (K)	296K	
Space group	*$I4_1/amd$*	
unit cell:	a (Å)	6.77761(5)
	c (Å)	6.14045(8)
	V ($Å^3$)	282.067(5)
Sc (4a)	U_i/U_e *100	1.35
	occ.	1.000
V (4b)	U_i/U_e *100	2.85
	Occ.	1.01(3)
O1 (16h)	x/a	0
	y/b	0.4425(1)
	z/c	0.1971 (1)
	U_i/U_e *100	1.33
O-V-O (˚)		114.34(3) 100.12(5)
d(V-O) (Å)		4 x 1.7014(7)
d(Sc-O) (Å)		4 x 2.1308(7) 4 x 2.3694(7)
Composition (TGA)		$ScVO_{3.94(2)}$
# of parameters		11
R_p: XRD NPD λ=2.37126(5)Å NPD λ=1.32967(2)Å Powder totals		4.19 3.16 3.19 3.70

R_{wp}: XRD	5.56
NPD λ=2.37126(5)Å	4.40
NPD λ=1.32967(2)Å	4.17
Powder totals	4.96
$R(F^2)$: XRD	12.20
NPD λ=2.37043(5)Å	3.56
NPD λ=1.33003(2)Å	11.88
χ^2: Powder totals	4.031

The d.c. magnetic susceptibility data for $ScVO_{4-y}$ were compared with those of fully oxidized zircon $ScVO_4$. The resulting difference between the temperature dependent d.c. magnetic susceptibility for $ScVO_{4-y}$ and $ScVO_4$ showed a small paramagnetic moment consistent with minute amounts of V^{4+}. Notably both $ScVO_4$ and $ScVO_{4-y}$ showed the typical paramagnetic temperature dependence due to miniscule amounts of paramagnetic (non-vanadium) impurities in the starting materials. However, subtracting the magnetic data for $ScVO_4$ from those of $ScVO_{4-y}$ eliminates the magnetic signal contribution from the starting materials. The resulting paramagnetic signal is solely due to the presence of V^{4+} in the defect zircon structure. The individual data and the difference plot are shown in figure 3.15.

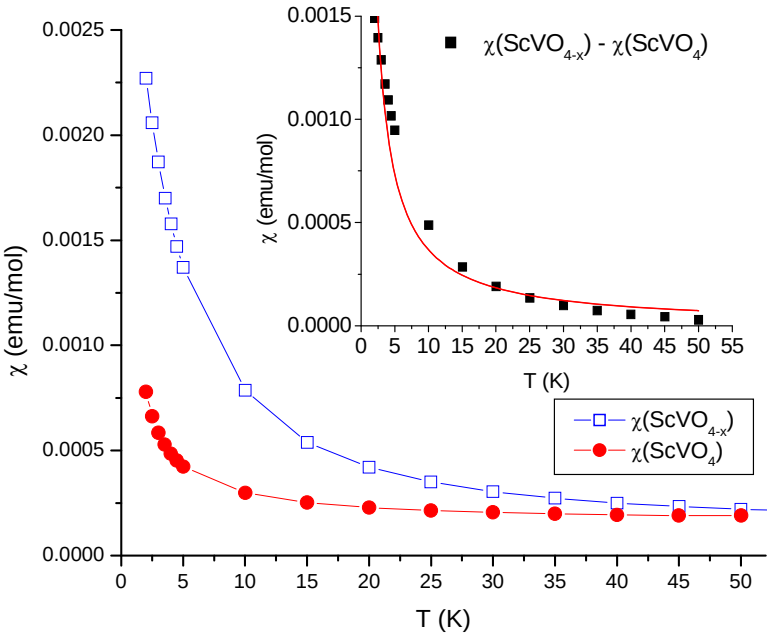

Figure 3.15. D.c. magnetic susceptibility data for $ScVO_4$ (Red) and $ScVO_{4-y}$ (Blue) measured at low temperatures in a magnetic field of H = 0.1 T. The temperature dependent magnetic susceptibility data for $ScVO_{4-y}$ after the subtraction of $ScVO_4$ susceptibility are shown in the inset, the solid red line represents the Curie fit.[98]

The Curie fit was carried out on the temperature dependent magnetic susceptibility data for $ScVO_{4-y}$ after the subtraction of $ScVO_4$ and is shown in the inset in figure 3.15. The most likely reason for the deviations from the Curie fit is the small differences of the sample holders used for the two measurements. However, the d.c. magnetic susceptibility is consistent with at least 3% of V^{4+} present in the sample.

Magic angle spinning solid state NMR spectroscopy showed broader ^{51}V peaks for the V^{5+}-O_4 tetrahedral environment in the defect zircon $ScVO_{4-y}$ (1110 Hz) compared to that of fully oxidized $ScVO_4$ (655 Hz). The plots are shown in figure 3.16; a and b represents ^{51}V MAS NMR central peaks for $ScVO_4$ and $ScVO_{4-y}$. The possible reasons for this broadening could be the increased disorder in the oxide defect zircon structure or the presence of paramagnetic centers. It was observed that the ^{51}V spin-lattice relaxation

times (T_1) decreased significantly from 25(1) s to 1.0(1) s for the defect structure, revealing the influence of paramagnetic cations. The mass normalized absolute integrated intensity of the ^{51}V signal reduced by approximately 7 % from $ScVO_4$ to $ScVO_{4-y}$ supporting the reduction of V^{5+} to paramagnetic V^{4+} in the defect zircon sample to form $ScVO_{3.94}$. The ^{45}Sc NMR spectrum for $ScVO_4$ (figure 3.16c) is in agreement with the previous data published by Kim et al.[99] of 8-fold coordinated scandium in $ScVO_4$. The ^{45}Sc peak broadens by approximately 1300 Hz (9 ppm) in $ScVO_{4-y}$ (figure 3.16d) due to the proximity of paramagnetic V^{4+}, a corresponding reduction in the relaxation time was also observed. Preliminary estimates for the relaxation times are 60 s for $ScVO_4$ and 2 s for $ScVO_{4-y}$.

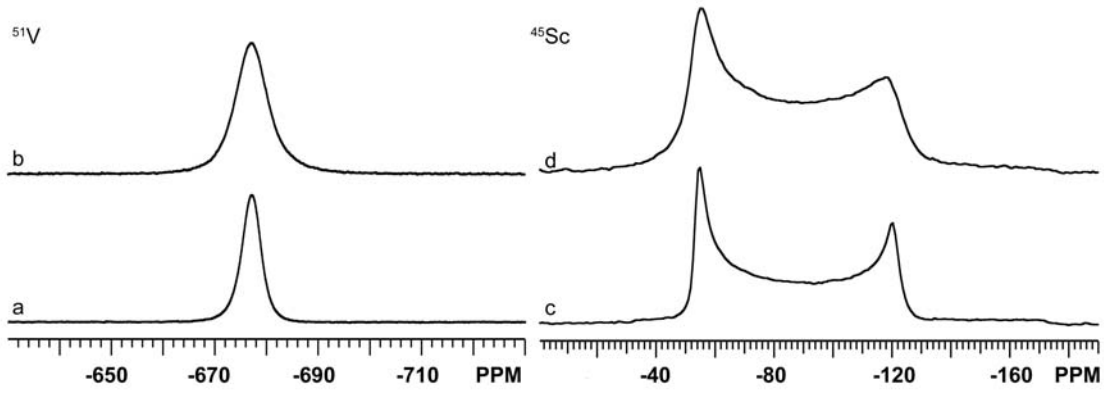

Figure 3.16. ^{51}V and ^{45}Sc MAS NMR central transition peaks for $ScVO_4$ (a and c) and $ScVO_{4-y}$ (b and d). Adapted from ref. 98.

3.3.3. Structural Aspects of the $ScVO_3$ Bixbyite Reactivity

This section focuses on the structural aspects of the three step oxidative pathway for $ScVO_3$ bixbyite to form $ScVO_4$ zircon. The first step involving the formation of $ScVO_{3.5+x}$ through topotactic oxidation has already been discussed in the first part of this

chapter. The bixbyite structure can be considered as an oxygen deficient fluorite structure with 25 % ordered oxygen defects. The defect concentrations vary from 12.5 to 7.0 % for $ScVO_{3.5+x}$ ($0.00 \leq x \leq 0.22$) depending on the value of x and the defects are disordered. Figure 3.17.a shows the cation movement during the first oxidation of bixbyite (red spheres) to form defect fluorite (green spheres). It should be noted that the coordinates have been adjusted to have a common origin for both structures. There are only subtle changes in the cation positions during this structural transition reinforcing the topotactic nature of this reaction step.

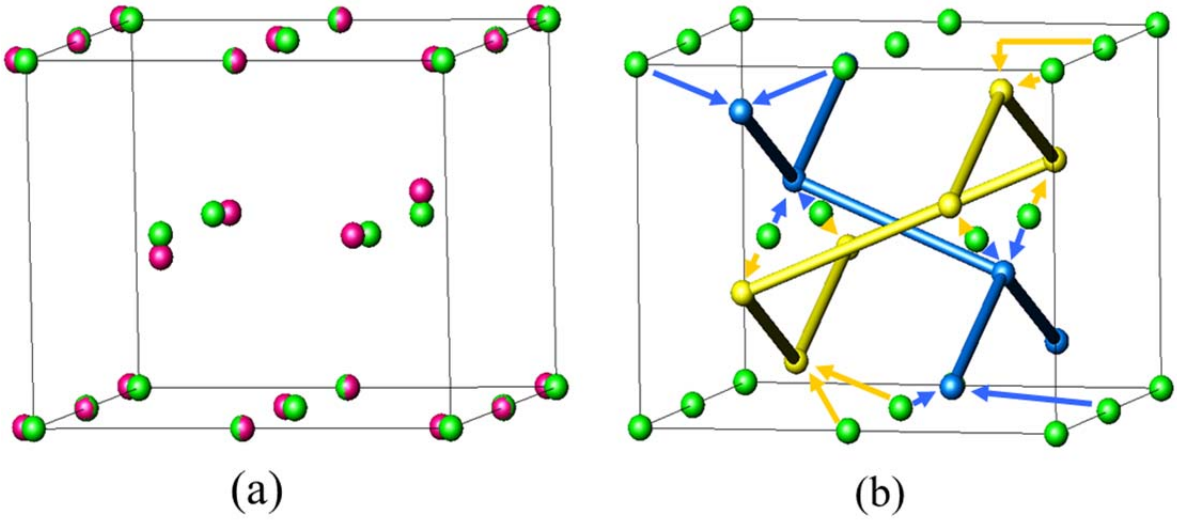

Figure 3.17. (a) Schematic illustration of cation movement during the bixbyite to fluorite structural transition. Green = disordered cations in the fluorite structure; Red = disordered cations in the bixbyite structure. (b) Schematic illustration of reconstruction of the cation network during the fluorite to zircon transition. Green = disordered cations in the fluorite structure; blue, yellow = ordered cation network in the zircon structure. All the oxide positions have been omitted for clarity.[98]

Figure 3.17.b shows the cation movement during the oxidative transition from the fluorite to the zircon structure. This is representative of the second oxidation step of defect fluorite $ScVO_{3.5+x}$ to defect zircon $ScVO_{4-y}$. In contrast to the first oxidation step,

the transition from fluorite to zircon requires major crystal structure reconstruction. The cations Sc^{3+} and V^{4+} (green spheres) were arranged in a disordered fashion in the fluorite structure whereas the cations have distinct positions (Sc^{3+} = blue, V^{5+} = yellow) in the zircon structure. The cations form two interpenetrating diamond sublattices in the zircon structure. We propose that the large concentration of the small V^{5+} cation for $ScVO_{3.72}$ collapses the fluorite structure, resulting in the formation of defect zircon structure. The smaller V^{5+} prefers to occupy the tetrahedral environment in the defect zircon structure $ScVO_{4-y}$. The final oxidative path involves filling the disordered oxide defects in the defect zircon structure with oxygen in a topotactic fashion to form the fully oxidized $ScVO_4$.

Furthermore, in order to evaluate the reversibility of the oxidation – reduction cycles, the reduction pathway for the $ScVO_4$ zircon to the $ScVO_3$ bixbyite structure was explored by means of in-situ x-ray diffraction and TGA – DTA analysis. The reduction proceeds through a single step with no indication of intermediate phases. This clearly indicates that $ScVO_{3.5+x}$ and $ScVO_{4-y}$ are only accessible if the appropriate starting materials are used. The crystalline domain sizes of the precursor phase $ScVO_{3.5+x}$ are considered important for the formation of the zircon oxide defect phase $ScVO_{4-y}$. The bulk synthesis of $ScVO_{4-y}$ was carried out by the oxidation of poorly crystalline $ScVO_{3.5+x}$ (D ≈225 (50) Å) in oxygen flow at 400 °C. With decreased particle size solid state reactions occur at lower temperature due to increased reaction kinetics. Oxidation of highly crystalline $ScVO_3$ never resulted in pure $ScVO_{4-y}$, instead phase mixtures of $ScVO_{3.5+x}$ and $ScVO_{4-y}$ were obtained. The in-situ powder x-ray diffraction experiments showed that the $ScVO_{4-y}$ defect zircon phase has a limited stability range as this phase is

stable only in the temperature range $450 \leq T \leq 570$ °C. The initial $ScVO_4$ precursor did not form any $ScVO_{4-y}$ zircon oxide defect structure during the in-situ powder x-ray diffraction reduction experiments. This is possibly due to the large domain sizes of $ScVO_4$ ($D \geq 1000$ Å) which does not permit fast kinetics and is therefore thermodynamically controlled. Consequently highly crystalline $ScVO_4$ reduced directly to highly crystalline $ScVO_3$ under reducing conditions. In order to investigate the influence of the particle size on the formation of the metastable defect zircon phase, a fully oxidized zircon phase with smaller domain sizes should be reduced in-situ. The particle size can be reduced to a few hundred Angstroms using sol-gel or co-precipitation reactions.

3.4. Conclusions and Future Work

The structure – reactivity relationship for the bixbyite oxidation pathway has been established and the entire oxidation sequence has been explored by means of in-situ techniques. The oxidation – reduction cycle for the AVO_3 – AVO_4 system is shown as a flow chart in figure 3.18. The reaction pathway and the associated phases indicated in red in the flow chart are the contributions from this project.

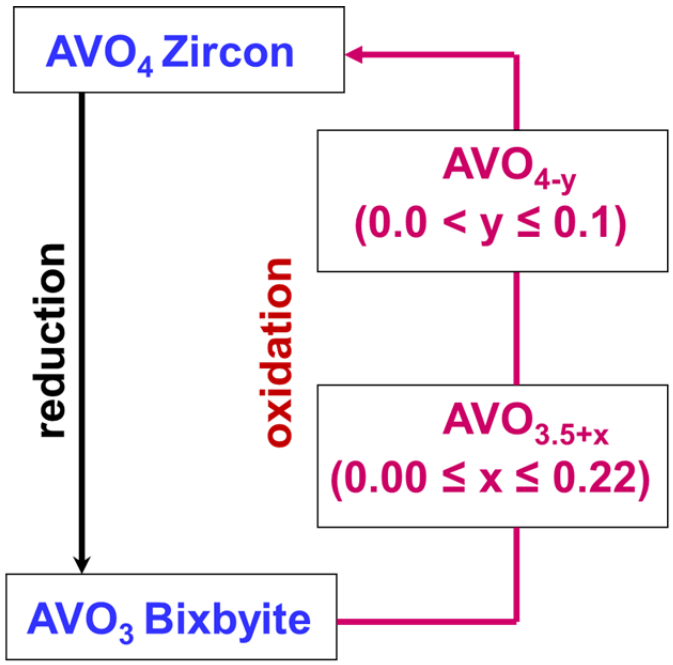

Figure 3.18. Structure flow chart of oxidation – reduction cycle for AVO_3 bixbyite – AVO_4 zircon systems.

It is important to mention that the newly identified metastable phases $AVO_{3.5+x}$ and AVO_{4-y} phases have partially occupied energetically equivalent oxide ion lattice sites which are integral ingredients for oxide ion conductivity. Hence, these novel materials are potential candidates for ion conductors in solid oxide fuel cells. The preliminary results of the electrical conductivity measurements carried out on a $ScVO_{3.5}$ defect fluorite sample are shown in figure 3.19.

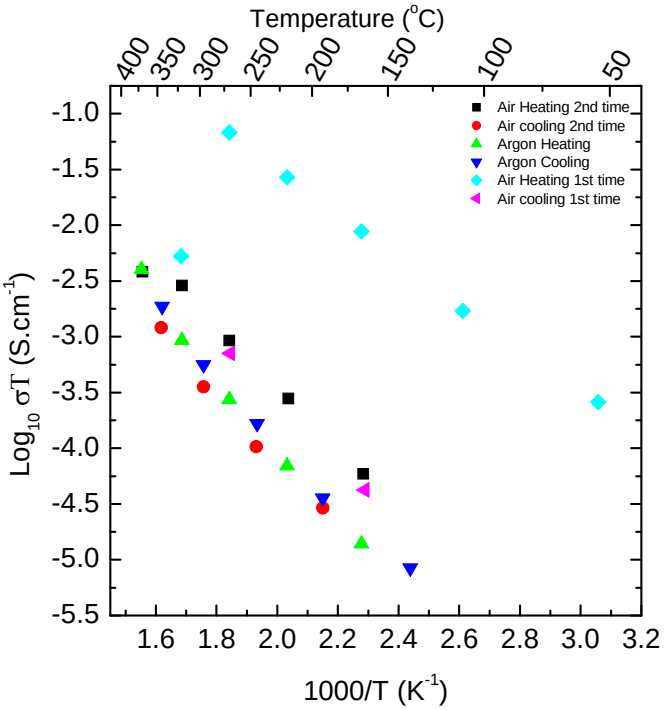

Figure 3.19. Arrhenius plots for total electrical conductivity data of $ScVO_{3.5}$ measured in air (light blue = first heating, magenta = first cooling, black = second heating and red = second cooling) and Argon atmosphere (light green = heating and dark blue = cooling).

The defect fluorite $ScVO_{3.5}$ showed promising conductivity at low temperatures. The first two heating and cooling cycles were carried out in air. It can be seen in the plot that the conductivity dropped during the first cooling (magenta) in comparison to the first heating (light blue) in air. The further measurements in air and Argon atmosphere showed similar ionic conductivities. It should be noted that $ScVO_{3.5}$ has an oxide defect concentration of 12.5 % and the first heating carried out in air must have resulted in oxidation of this phase. It is speculated that oxidation diminished the available oxide defects in the structure which resulted in a reduction of the conductivity. The powder x-ray diffraction pattern of the material after the conductivity measurements showed peak shifts to lower diffraction angles compared to the original $ScVO_{3.5}$ indicative of a larger

unit cell and higher oxygen content. The major drawback of this phase appears to be the undesired oxidation at low temperatures itself. One approach to tackle this issue would be by replacing vanadium with an appropriate cation so that oxidation can be avoided; i.e., choose a B cation with a maximum oxidation state of +4.

The range of oxygen stoichiometry that can be tolerated by the defect fluorite phase was identified to be between $ScVO_{3.50}$ and $ScVO_{3.72}$. Consequently the oxygen defect concentration can be adjusted and controlled during the synthesis. The oxygen defect concentrations for this structure vary from 12.5 % to 7.0 %. As indicated previously in the discussion section, a broad peak at $d \approx 2.13$ Å was observed in the neutron diffraction data suggesting a clustering of oxide ions and the domain size of these clusters is approximately 20 Å. From the well-established AVO_3 bixbyite oxidation sequence to AVO_4 zircon, it is known that the $AVO_{3.5+x}$ defect fluorite structure is an important intermediate. It would be interesting to investigate the influence of oxygen clusters for the reactivity of these structures. A neutron pair distribution experiment was conducted at Los Alamos National Laboratory to investigate the significance of oxygen clustering during $ScVO_{3.5}$ oxidation and to shed light on the oxidation pathway. The data analysis should provide insights into the influence of oxygen clusters on $ScVO_{3.5}$ reactivity.

The methodologies and results of this research have built a firm foundation for understanding the bixbyite structure – reactivity relationship. The ample opportunities for the synthesis of a variety of structures with variable oxygen concentration through controlled oxygen addition are very evident. Chapter 5 exploits some of these key research methodologies and findings.

Chapter 4: Investigation of AVO_3 Perovskite Reactivity

The major part of the research works discussed in chapter 4 have been presented in the manuscript 'Highly Stable Cooperative Distortion in a Weak Jahn-Teller d^2 Cation: Perovskite-Type $ScVO_3$ Obtained by High-Pressure and High-Temperature Transformation from Bixbyite' published in Journal of the American Chemical Society, volume 133 (2011), pages 8552-8563.[vi]

The chapter contains additional data and expanded discussion. The work described in this chapter was performed in collaboration with Departamento de Química Inorgánica & Laboratorio Complutense de Altas Presiones at Universidad Complutense de Madrid. Chapter 4: Results and Discussion focus on the contributions of S. P. Shafi to this manuscript. A discussion on the synthesis and preliminary structural details of $ScVO_3$ perovskite phase has been included in this chapter and these works were performed by E. Castillo-Martinez. The experimental work and the preparation of figures corresponding to the thermal stability and the oxidation pathway of $ScVO_3$ perovskite were performed by S. P. Shafi.

[vi] Based on "Castillo-Martinez, E.; Bieringer, M.; Shafi, S. P.; Cranswick, L. M. D.; Alario-Franco, M. A. J. Am. Chem. Soc. **2011**, 133, 8552-8563. Copyright © 2011 American Chemical Society."

Abstract

Chapter 4 focuses on the investigation of AVO_3 perovskites (A = Lu, Sc) reactivity under oxidative conditions. The novel metastable $ScVO_3$ perovskite has been synthesized at 8 GPa and 800 °C from the cation disordered $ScVO_3$ bixbyite phase. Powder x-ray diffraction data analysis showed that the $ScVO_3$ perovskite crystallizes in the orthorhombic structure in space group *Pnma* with lattice cell parameters a = 5.4006(2) Å, b = 7.5011(2) Å and c = 5.0706(1) Å. Powder neutron diffraction data analysis showed that the cations Sc^{3+} and V^{3+} occupy the A and B sites of the perovskite cell in an ordered fashion. The thermal stability and the reactivity of $ScVO_3$ perovskite has been investigated by means of in-situ x-ray diffraction. The reactivity of $ScVO_3$ perovskite has been compared with that of the bixbyite structure.

4.1. Introduction

Perovskite structures are commonly encountered in materials science and there are innumerable materials with perovskite or closely related superstructures with potential applications covering giant magnetoresistance, ferroelectric, piezoelectric, superconducting, ion conducting and optical properties.[100-102] The previous chapter discussed the reactivity of the AVO_3 bixbyite structure in detail. Our continued interest in understanding the structure – reactivity relationship prompted us to investigate the reactivity of the AVO_3 perovskite structure and compare its reactivity with that of the AVO_3 bixbyite phase.

4.1.1. Motivation and Background Literature

AVO_3 perovskite (A = La – Lu) structures are known to show diverse crystallographic varieties and physical properties.[58-62] AVO_3 structure types are primarily determined by the size of the A^{3+} cations. The AVO_3 series (A = La-Lu, Y) is isostructural to the orthorhombic $GdFeO_3$ structure (space group *Pnma*). The AVO_3 (A = La – Lu) perovskites can be synthesized by the reduction of the corresponding AVO_4 phases. The average V-O-V bond angle in AVO_3 decreases as the A^{3+} cation size decreases, consequently a monotonic decrease in the magnetic ordering temperatures for the canted antiferromagnetic ground state is observed.[103] The Néel temperature was found to range from 143 K for $LaVO_3$[104] to ≈ 107 K for $LuVO_3$.[105] Lu^{3+} is the smallest ($Lu^{3+}_{(VIII)}$ = 0.977 Å) A^{3+} cation known which is capable of forming a stable AVO_3 perovskite at ambient pressure. $LuVO_3$ crystallizes in the orthorhombic structure with the space

group *Pnma* (62) with V^{3+} on the B-cation site. The crystal structure of $LuVO_3$ is shown in figure 4.1 with emphasis on the two V-O-V bond angles.

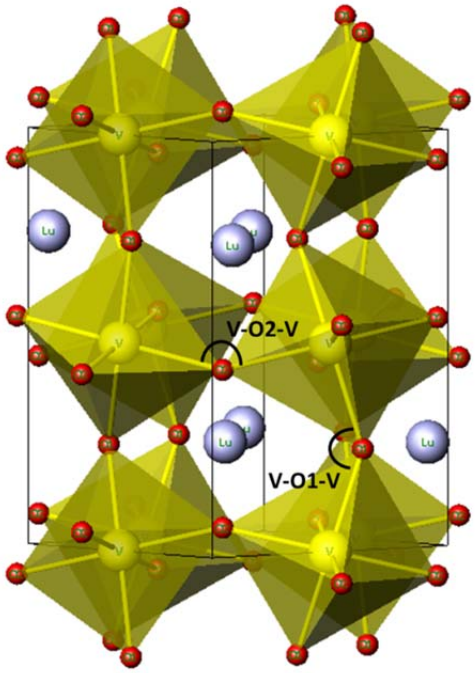

Figure 4.1. The crystal structure of $LuVO_3$; Lu = gray spheres, V = yellow spheres and O = red spheres. The two distinct V-O-V bond angles are represented by V-O1-V and V-O2-V.

Preliminary investigations of the $LuVO_3$ perovskite reactivity under oxidative conditions showed no indication of the formation of a defect fluorite phase. This is in contrast to the observation of two intermediates during the AVO_3 bixbyite oxidation pathway, thus reinforcing our earlier claims of the need for bixbyite starting material for the synthesis of $AVO_{3.5+x}$ ($0 \leq x \leq 0.22$) defect fluorites. The AVO_3 perovskite reactivity is explored in detail in the following sections with a more suitable structural model $ScVO_3$ perovskite.

Ideally, having two structure types with the same composition is highly beneficial to the study of structure – reactivity relationships. Previously, the solid solution $Sc_{(1-x)}Lu_xVO_3$ ($0 \leq x \leq 1$) was investigated in detail by Lundgren, R. J. et al. and the perovskite stability limit was identified.[106] The $Sc_{(1-x)}Lu_xVO_3$ phases were prepared via the reduction of $Sc_{(1-x)}Lu_xVO_4$ using a CO/Ar atmosphere. The $Sc_{(1-x)}Lu_xVO_3$ system showed both perovskite and bixbyite structure types. The end members $ScVO_3$ and $LuVO_3$ crystallize in the bixbyite ($Ia\bar{3}$) and orthorhombic $GdFeO_3$ structures (*Pnma*), respectively. Also, Sc-rich compositions ($x < 0.1$) formed the bixbyite structure whereas the Lu-rich regime ($x > 0.58$) crystallized in the $GdFeO_3$ distorted perovskite structure. Note that the reduction of $Sc_{(1-x)}Lu_xVO_4$ was carried out at 1300 °C and for $0.1 < x < 0.58$ no thermodynamically stable single phase was observed in the $Sc_{(1-x)}Lu_xVO_3$ system. The diffraction peaks were reported to be consistent with biphasic perovskite and bixbyite structures. Figure 4.2 represents the formula unit volume for $Sc_{(1-x)}Lu_xVO_3$ as a function of refined Lu content. The formula unit volumes of the perovskite phases were reported to be less than those of bixbyite phases which indicates that the perovskite structures are more efficiently packed in comparison to the bixbyite structures. Note that the comparison has been made between different compositions. However, Lu^{3+} is larger than Sc^{3+} and the perovskite phases have a larger Lu content (Shannon ionic radii: $Sc^{3+}{}_{(VI)}$ = 0.745 Å, $Lu^{3+}{}_{(VI)}$ = 0.861 Å, $Sc^{3+}{}_{(VIII)}$ = 0.87 Å, $Lu^{3+}{}_{(VIII)}$ = 0.977 Å) and hence it can be stated that, in general, perovskite phases are denser than the bixbyite structures in $Sc_{(1-x)}Lu_xVO_3$ systems. Lundgren and coworkers synthesized metastable $Sc_{(1-x)}Lu_xVO_3$ bixbyite for $x \leq 0.4$ through low temperature reduction (T = 600 – 650 °C, 1:1 CO/Ar) of

the corresponding $Sc_{(1-x)}Lu_xVO_4$ phases. Their report showed that the formula unit volume for $InVO_3$ is equivalent to the hypothetical $Sc_{0.3}Lu_{0.7}VO_3$ bixbyite phase.

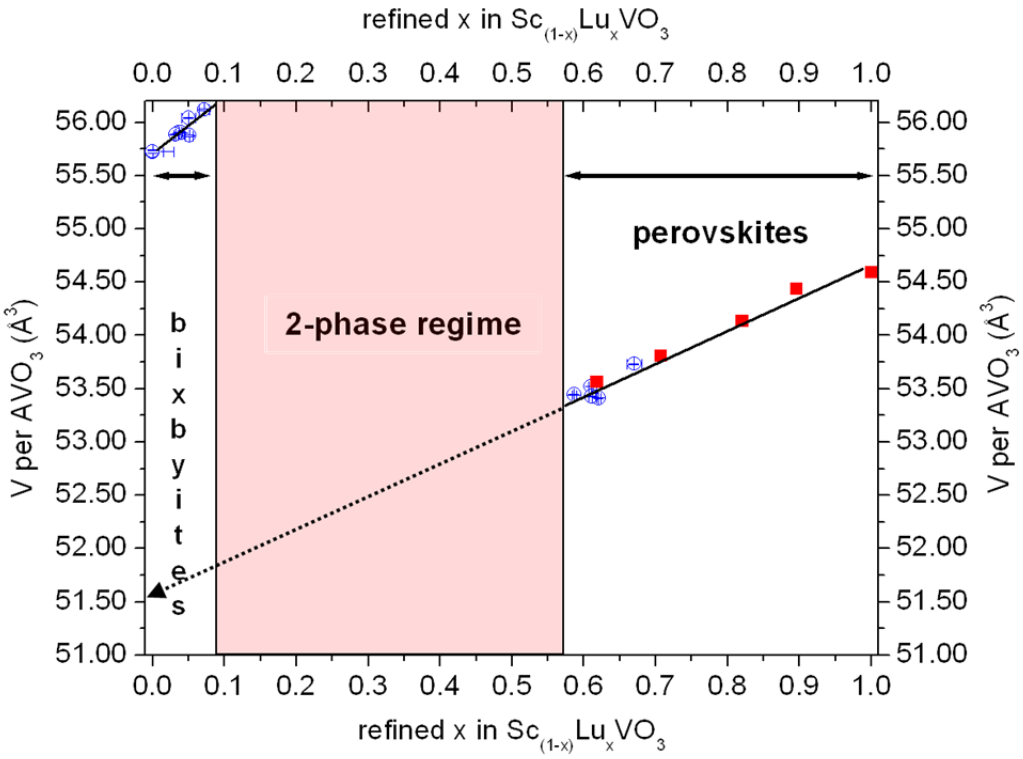

Figure 4.2. Volume per formula unit of $Sc_{(1-x)}Lu_xVO_3$ at room temperature. The values of x were determined from Rietveld refinements. Solid symbols = single phase products, open symbols = biphasic products. The perovskite volume per formula unit has been extrapolated to identify the volume per formula unit for the hypothetical $ScVO_3$ perovskite (shown with the dotted arrow). "Adapted with permission from (Lundgren, R. J.; Cranswick, L. M. D.; Bieringer, M. Chemistry of Materials 2007, 19, 3945-3955) Copyright © 2007 American Chemical Society."

In short, this report by Lundgren and coworkers indicated that the perovskite structure is denser than the bixbyite structure in the $Sc_{(1-x)}Lu_xVO_3$ system. We are interested in converting the $ScVO_3$ bixbyite structure prepared at ambient pressure to a perovskite structure which would require densification. The volume of $Sc_{(1-x)}Lu_xVO_3$

perovskite has been extrapolated toward the y-axis (V/f.u.) and the expected volume of phase pure perovskite $ScVO_3$ is indicated with the arrow in figure 4.2. The synthesis of $ScVO_3$ perovskite can be achieved through high pressure as the technique has shown promise in stabilizing many perovskite polytypes. A significant feature associated with high pressure synthesis is cation ordering which is the key ingredient for the transition from cation disordered bixbyites to cation ordered perovskites. It should be noted that such a structural conversion would also require high temperatures for cation mobility.

4.1.2. Synthesis and Structural Characterization of $ScVO_3$ perovskite:

The synthesis of $ScVO_3$ perovskite and the structural analysis were carried out in collaboration with Prof. Miguel Alario-Franco and his group in Madrid. The ex-situ synthesis of $ScVO_3$ perovskite from $ScVO_3$ bixbyite was attempted at various pressures and temperatures.[107] Single phase $ScVO_3$ perovskite was obtained at 8 GPa and 800 °C. The product $ScVO_3$ perovskite was black in color and showed a shinier luster than the brownish black starting material $ScVO_3$ bixbyite.

Preliminary structural characterization including the symmetry, lattice parameters and starting atomic positions were inferred from the Rietveld refinement of the powder x-ray diffraction data collected at room temperature. A good agreement was obtained for space group *Pnma* (62) and the reliability factors were R_p= 5.56, R_{wp} = 7.71 and χ^2 = 2.05. Powder x-ray diffraction data analysis showed that $ScVO_3$ perovskite crystallizes in the orthorhombic structure in space group *Pnma* with lattice cell parameters a = 5.4006(2) Å, b = 7.5011(2) Å and c = 5.0706(1) Å. Scandium and vanadium do not show much contrast in x-ray diffraction (Z(Sc) = 21, Z(V) = 23). On the other hand, vanadium

is a weak neutron scatterer (b(V) = -0.3824 fm) whereas scandium is a very strong neutron scatterer (b(Sc) = 12.29 fm). Also, reliable oxygen positions can be determined from neutron diffraction data as oxygen is a good neutron scatterer (b(O) = 5.803 fm). The Rietveld refinement of the room temperature powder neutron diffraction data showed that in the perovskite structure the A site is solely occupied by Sc and the B site is exclusively occupied by V. However, a 5% deficiency was observed on the Sc position. A schematic representation of the distorted $ScVO_3$ perovskite at room temperature is shown in figure 4.3. The density of the perovskite phase was found to be 7.8 % greater than that of the original bixbyite phase. The volume per formula unit obtained for the perovskite phase (51.4(1) $Å^3$) is in good agreement with the value predicted earlier in figure 4.1.

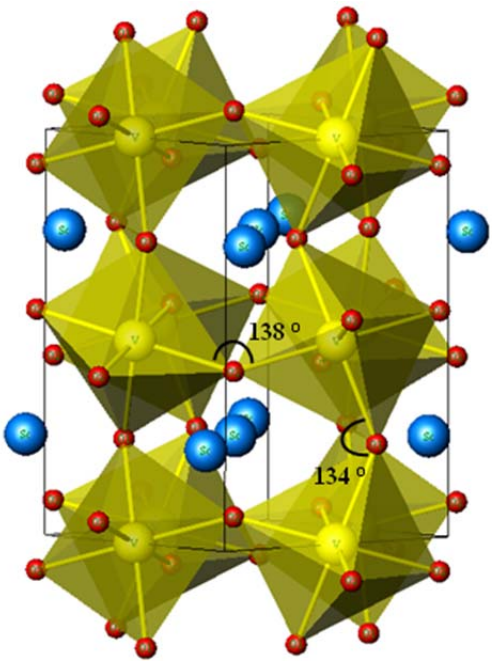

Figure 4.3. The crystal structure of $ScVO_3$ perovskite; Sc = blue spheres, V = yellow spheres and O = red spheres.

4.2. Results and Discussion

4.2.1. $ScVO_3$ Perovskite Thermal Stability and Reactivity under Oxidative Conditions

The thermal evolution of $ScVO_3$ perovskite was followed using in-situ powder x-ray diffraction at ambient pressure. The experiment was carried out under CO:He (1:3 volume ratio) in order to avoid oxidation. The temperature dependent contour plot from 25 to 1000 °C for the 2θ range 31 – 38 ° is shown in figure 4.4. Upon heating, the perovskite peaks were observed to shift to lower 2θ angle due to thermal expansion. The powder x-ray diffractograms collected during $ScVO_3$ annealing for the relevant high temperature regime is shown in figure 4.5. The changes in the high temperature x-ray diffractograms shown in figure 4.5 clearly indicate the onset of bixbyite peaks and the decrease in perovskite peak intensity at T ≈ 800 °C. The perovskite peaks were found to disappear completely at T ≈ 900 °C. The coexistence of both perovskite and bixbyite phases over the temperature range 800 to 900 °C indicate that the phase transition is first-order. In summary, the metastable $ScVO_3$ perovskite phase relaxes back to the thermodynamically stable ambient pressure bixbyite phase at T > 800 °C. This shows the metastable nature of $ScVO_3$ perovskite structure. The cations in the perovskite structure become mobile at high temperatures and the structure relaxes back to the cation disordered bixbyite phase.

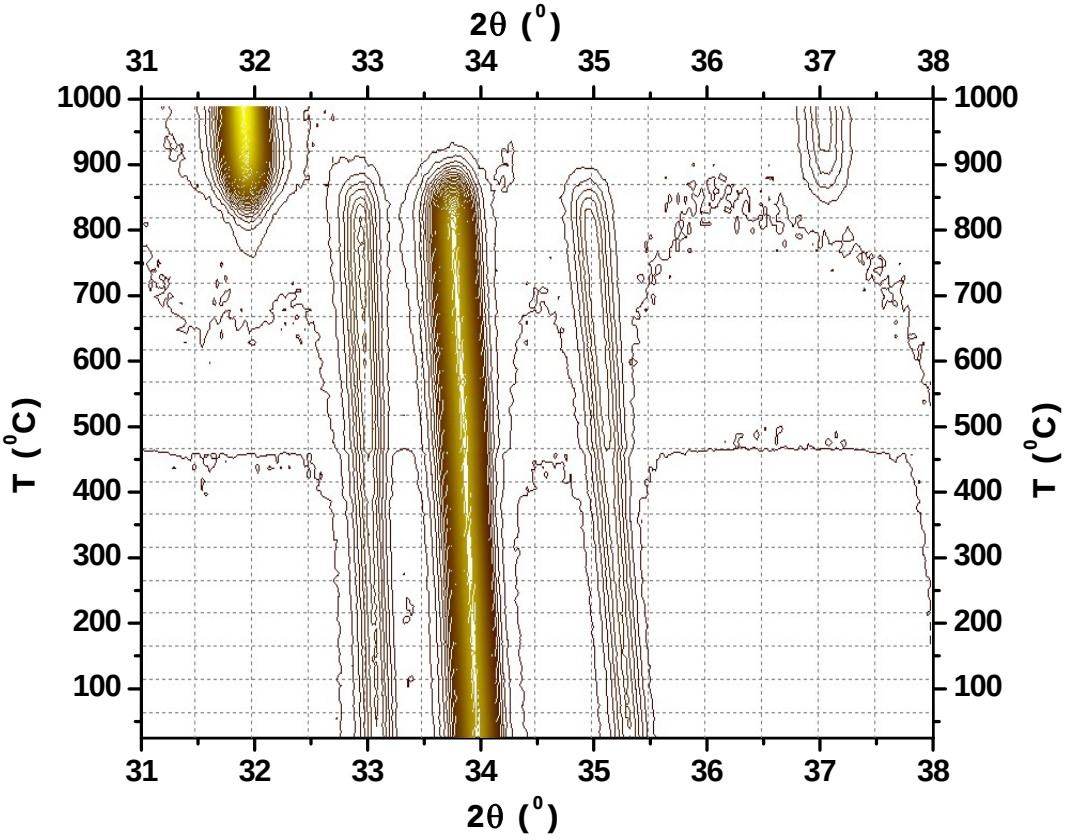

Figure 4.4. Temperature dependent in-situ powder x-ray diffraction contour plot of $ScVO_3$ perovskite annealing from 30 to 990 °C at 10 °C increments under a CO/He (1:3 volume ratio) atmosphere. Intensities are shown as constant increments from brown (lowest intensity) to yellow (highest intensity). Adapted from ref. 107.

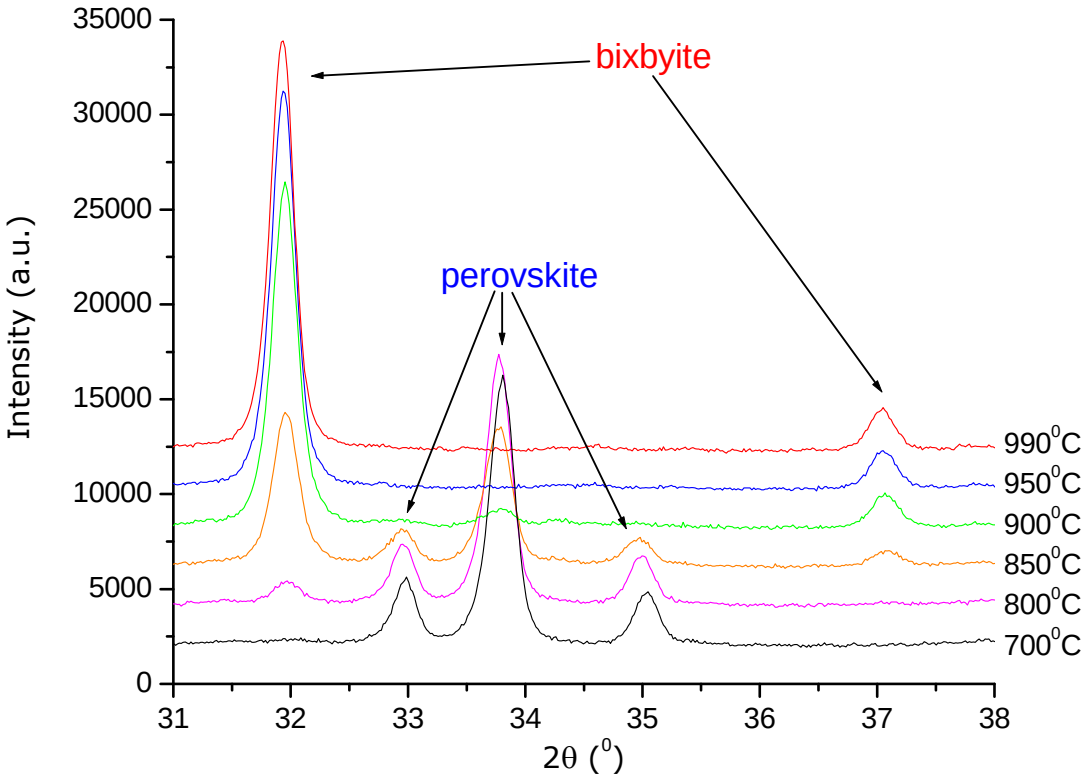

Figure 4.5. Selected high temperature Powder x-ray diffractograms collected during $ScVO_3$ perovskite annealing under CO/He (1:3 volume ratio) atmosphere.

The $ScVO_3$ perovskite oxidation pathway was studied using in-situ powder x-ray diffraction. The powder x-ray diffraction contour plot for $ScVO_3$ perovskite oxidation carried out in oxygen is shown in figure 4.6. The perovskite peaks shift to lower 2θ angles up to T ≈ 400 °C due to thermal expansion. At 420 °C new peaks belonging to the zircon phase were observed, indicative of oxidation of $ScVO_3$ perovskite phase. The perovskite peaks disappeared completely at T ≈ 550 °C suggesting the completion of oxidation. Hence the perovskite oxidation pathway was single-step and showed no indication of any intermediate phases.

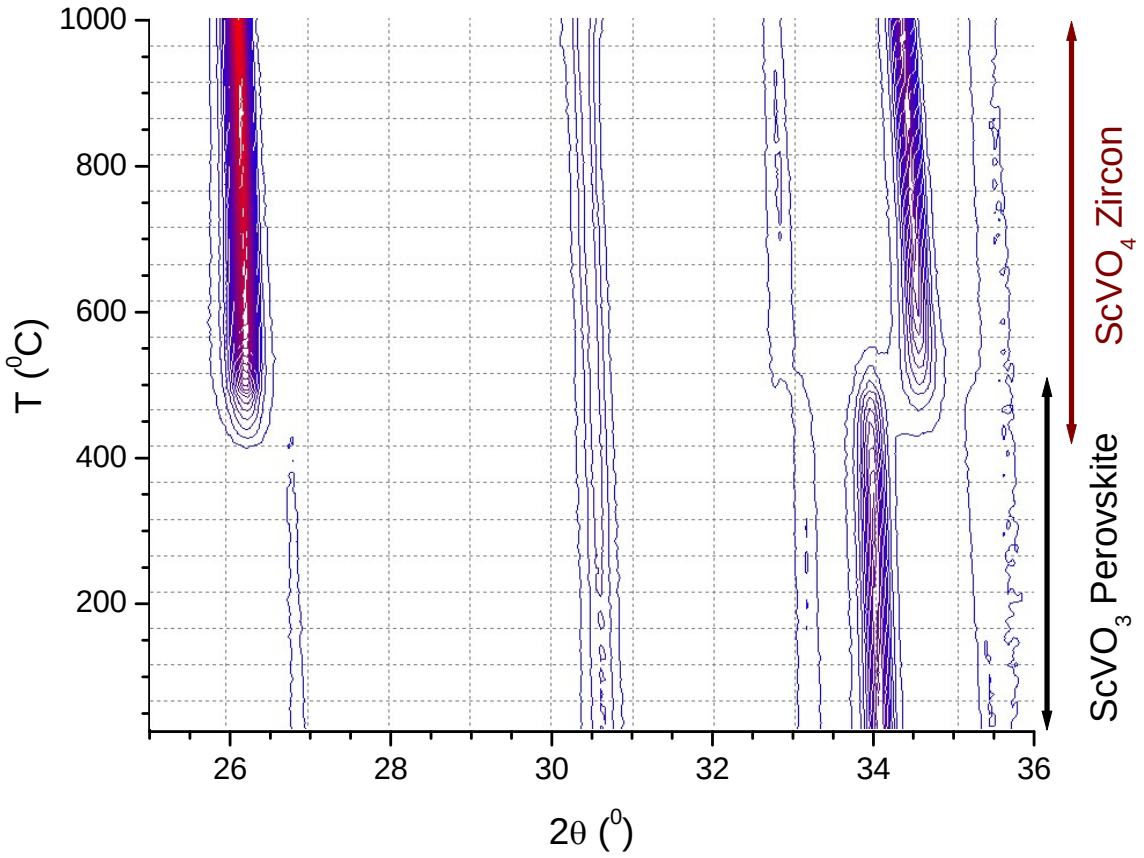

Figure 4.6. High temperature powder x-ray diffraction contour plot of $ScVO_3$ perovskite oxidation in oxygen from 25 to 1000 °C with 10 °C increments. Intensities are shown as constant increment from lowest intensity blue to highest intensity red.

4.3. Conclusion and Future Work

The transformation of the cation disordered bixbyite to the cation ordered perovskite has been achieved through high pressure synthesis. Previous reports[108-112] show that high pressure can cause a transition for $(AA')_2O_3$ oxides through the path: bixbyite → corundum → Rh_2O_3 (II) → $GdFeO_3$ (*o*-perovskite) → $CaIrO_3$ (post perovskite). The quenched products obtained after treating $ScVO_3$ bixbyite at various pressures and temperatures did not show any indication of phases other than bixbyite or

perovskite. This confirms the transition path mentioned above and should generally be applicable for the bixbyite phases formed by the reduction of $AA'O_4$ zircon phases. The transformation pathway for bixbyite → perovskite could be probed using in-situ techniques under high pressure. Identification and quenching of these intermediates would provide a whole series of AVO_3 phases ideal for structure – reactivity and structure – property studies. The quenched $ScVO_3$ perovskite phase is metastable and did not show any decomposition at room temperature even after two years. Due to the small size of Sc^{3+}, $ScVO_3$ is the most tilted RVO_3 perovskite reported so far. At ambient pressure and T > 800 °C, the metastable perovskite relaxes back to the bixbyite phase. The reactivity of $ScVO_3$ perovskite has been explored and is compared with the bixbyite reactivity in figure 4.7. In contrast to the bixbyite oxidation pathway where two intermediates were observed, the perovskite oxidation did not show any intermediates. This confirms the strong relationship between structure and reactivity. Future work should focus on applying the structure – reactivity relationship discussed so far to new systems. As the high pressure synthetic route has been successful for the transformation of bixbyite to perovskite, $InVO_3$ is another promising candidate to explore the structure – reactivity relationship in AVO_3 systems. It would be interesting to look at the effect of high pressure and high temperature on the intermediates such as $ScVO_{3.5}$ formed during bixbyite oxidation. The cations in the defect fluorite $ScVO_{3.5}$ are disordered and there is a strong possibility for the transformation to the cation ordered pyrochlore structure $Sc_2V_2O_7$ at high temperature and pressure.

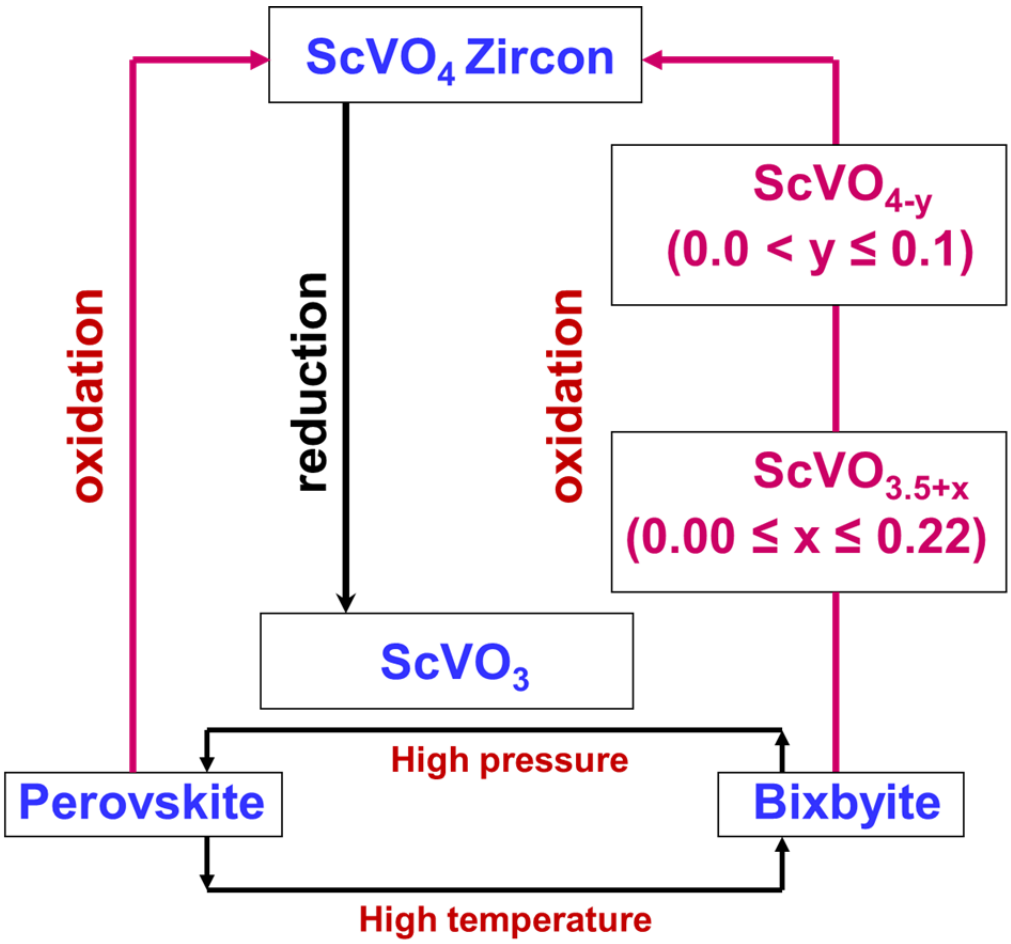

Figure 4.7. Structure flow chart comparing the oxidation pathway for $ScVO_3$ bixbyite and perovskite to $ScVO_4$ zircon systems.

Chapter 5: Investigation of $ScTiO_3$ Bixbyite Reactivity

The major part of the research work discussed in chapter 5 encompasses the manuscript 'Topotactic Oxidation Pathway of $ScTiO_3$ and High-Temperature Structure Evolution of $ScTiO_{3.5}$ and $Sc_4Ti_3O_{12}$-Type Phases' published in Inorganic Chemistry, volume 51 (2012), pages 1269-1277. [vii] The chapter contains additional data and expanded discussions.

All the experiments except neutron powder diffraction data collection (by L. M. D. Cranswick and T. Hansen) were designed and conducted by S. P. Shafi. All the figures and initial manuscript drafts were prepared by S. P. Shafi. S. P. Shafi and Dr. M. Bieringer were responsible for the revisions and final editing of the manuscript.

[vii] Based on "Shafi, S. P.; Hernden, B. C.; Cranswick, L. M. D.; Hansen, T. C.; Bieringer, M. Inorg. Chem. **2012**, 51, 1269-1277). Copyright © 2012 American Chemical Society."

Abstract

$ScTiO_3$ bixbyite reactivity in air has been studied in detail with emphasis on deducing a generalized reaction pathway for bixbyite oxidation. The oxidation pathway of $ScTiO_3$ and structure evolution of $ScTiO_{3.5}$, $Sc_4Ti_3O_{12}$ and related scandium deficient phases as well as high temperature phase transitions are reported. A detailed powder neutron diffraction study on $ScTiO_3$ bixbyite is presented for the first time. $ScTiO_3$ crystallizes in the cubic bixbyite structure in space group $Ia\bar{3}$ (206) with a = 9.7099(4) Å. The topotactic oxidation product $ScTiO_{3.5}$ crystallizes in the cubic defect fluorite structure in space group $Fm\bar{3}m$ (225) with a = 4.89199(5) Å. In-situ powder x-ray diffraction studies combined with thermogravimetric and differential thermal analysis experiments illustrate a complex sequence of topotactic oxidation steps, phase segregation and ion ordering at elevated temperatures. In comparison to the previously discussed vanadium bearing defect fluorite phases $AVO_{3.5+x}$ (A = In, Sc) the novel titanium analogue is stable over a wide temperature range. $ScTiO_{3.5}$ decomposes at high temperatures with the final products being $Sc_4Ti_3O_{12}$ and TiO_2 rutile. Simultaneous Rietveld refinements of powder x-ray and neutron diffraction data showed that $Sc_4Ti_3O_{12}$ also exists in the defect fluorite structure in space group $Fm\bar{3}m$ (225) with a = 4.90077(4) Å. $Sc_4Ti_3O_{12}$ undergoes partial reduction in a CO/Ar atmosphere to form $Sc_4Ti_3O_{11.69(2)}$.

5.1. Introduction

So far, the bixbyite reactivity studies have been carried out only on V^{3+} bearing phases.[69,97,98] The purpose of this project is to generalize the bixbyite oxidation pathway by studying non-vanadium based bixbyite reactivity. The $AVO_{3.5+x}$ (A = In, Sc; $0.0 \leq x \leq 0.22$) defect fluorite structures formed during the oxidation of AVO_3 bixbyite showed limited stability under oxidizing conditions.[97,98] The questions we are trying to answer with this study are the following.

(a) Is it possible to increase the stability range for the defect fluorite phase by substituting vanadium with another element for which the maximum possible oxidation state is +4 and thereby maintain high defect concentrations at high temperatures?

(b) What is the temperature range over which this phase is stable and what would happen beyond that temperature range?

Titanium is a good candidate for replacing vanadium in the bixbyite structure (Shannon ionic radii $V^{3+}_{(VI)} = 0.64$ Å, $Ti^{3+}_{(VI)} = 0.67$ Å). To the best of our knowledge only very few phases are known in the Sc – Ti – O phase diagram, namely, $ScTiO_3$,[68] Sc_2TiO_5,[113] $(Sc_xTi_{1-x})_2O_3$,[114] $Sc_4Ti_3O_{12}$,[115,116] $Sc_9Ti_{10}O_{31.2}$ [117]and $Sc_2Ti_2O_7$.[118-120] Among these phases, $ScTiO_3$ crystallizes in the cubic bixbyite structure in space group $Ia\bar{3}$ (206). Titanates provide a unique opportunity to stabilize the defect fluorite structure at high temperatures due to the absence of higher oxidation states than 4+ for titanium. Investigation of bixbyite reactivity with $ScTiO_3$ bixbyite as the structural model is expected to answer the above mentioned questions.

5.2. Results and Discussion

5.2.1. Reactivity of $ScTiO_3$ bixbyite under oxidative conditions

$ScTiO_3$ crystallizes in the reported[68,121] cubic bixbyite structure in space group $Ia\bar{3}$ (206) with scandium and titanium disorder on the *8b* and *24d* sites. The structural details of $ScTiO_3$ as determined by powder x-ray and neutron diffraction are discussed later in this chapter. Figure 5.1 shows the in-situ powder x-ray diffraction contour plots for $ScTiO_3$ oxidation.[121]

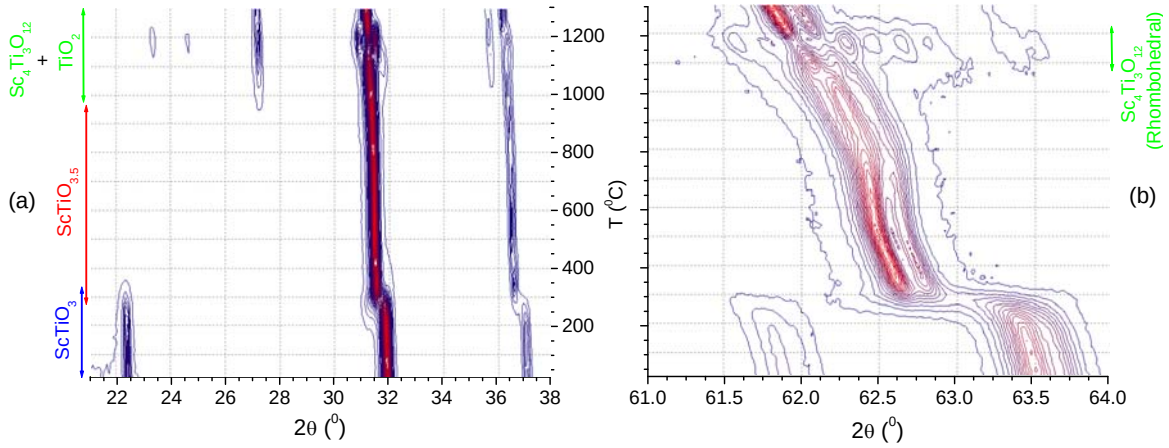

Figure 5.1. Temperature dependent in-situ x-ray diffraction contour plot of $ScTiO_3$ bixbyite oxidation in air from 25 to 1300 °C at 20 °C increments ;(a) 21 °≤ 2θ ≤ 38° and (b) 61 °≤ 2θ ≤ 64° . Diffraction peak intensities are shown as constant increments from blue (lowest intensity) to red (highest intensity). Adapted from ref. 121.

It can be seen in figure 5.1 that $ScTiO_3$ persists up to 300 °C and a new intermediate phase begins to form at 240 °C indicating the oxidation of the bixbyite. The x-ray diffraction pattern of the intermediate phase resembles that of $AVO_{3.5}$ (A = In, Sc) and can be indexed on a cubic unit cell in space group $Fm\bar{3}m$. The intermediate phase is an oxygen deficient phase with composition $ScTiO_{3.5}$ and is stable up to 840 °C. The low oxidation temperature (240 – 300 °C) is indicative of the topotactic nature of the reaction

and is in agreement with previously discussed close structural relationships between the bixbyite and the fluorite structure.[97,98] The temperature stability range during the in-situ formation in air for $ScTiO_{3.5}$ (up to 920 °C) is considerably larger than that for $ScVO_{3.5+x}$ (up to 425 °C). At T > 920 °C, decomposition of the defect fluorite phase into TiO_2 rutile and another scandium titanate phase consistent with space group $Fm\bar{3}m$ was observed. The diffractogram of the decomposition product matches $Sc_4Ti_3O_{12}$ (ICDD powder x-ray diffraction reference code: 00-031-1227). The appearance of a new set of peaks can be observed for 1080 ≤ T ≤ 1240 °C in figure 5.1.a and very noticeably in figure 5.1.b. This set of new peaks can be indexed on a rhombohedral structure with space group $R\bar{3}$ (148) and is consistent with anion ordered $Sc_4Ti_3O_{12}$. Notably, the anion disordered (cubic) and the anion ordered (rhombohedral) $Sc_4Ti_3O_{12}$ phases coexist in the temperature range 1080 ≤ T ≤ 1240 °C indicative of a first-order phase transition.

5.2.2. Evolution of Unit Cell Dimensions during Oxidation and Annealing

The cubic unit cell volume evolution of $Sc_yTi_zO_{3+x}$ is plotted as a function of temperature during the oxidation of $ScTiO_3$ in figure 5.2. The unit cell volumes of $Sc_yTi_zO_{3+x}$ phases were obtained from Rietveld refinements of temperature dependent powder x-ray diffraction data. The initial linear volume increase up to T ≈ 200 °C shows the thermal expansion of $ScTiO_3$ (blue solid circles) which is followed by an upturn due to oxygen uptake in the bixbyite structure up to T ≈ 300 °C. The oxidation occurs at 240 °C and the unit cell volume of the defect fluorite structure $ScTiO_{3.5-x}$ (red solid circles) increases until all the Ti^{3+} has been oxidized to Ti^{4+}. The nonlinear unit cell volume evolution between 400 and 700 °C is possibly due to oxide defect randomization in $ScTiO_{3.5}$. The thermal expansion of $ScTiO_{3.5}$ and $Sc_4Ti_3O_{12}$ were determined in two

separate in-situ diffraction experiments and the unit cell dimension evolution is plotted as red and green lines respectively in figure 5.2. The linear volume increase between 700 and 850 °C (solid red circles) is due to the thermal expansion of oxide vacancy randomized $ScTiO_{3.5}$. Markedly, this volume evolution is consistent with the thermal expansion data for $ScTiO_{3.5}$ (red line). This clearly indicates that the defects are formed as clusters initially and only randomize in the entropic limit after high temperature treatment. The unit cell volume of the defect fluorite phase formed from the topotactic oxidation of the bixbyite $ScTiO_3$ is in perfect agreement with that measured during the thermal expansion of $ScTiO_{3.5}$ at 800 °C.

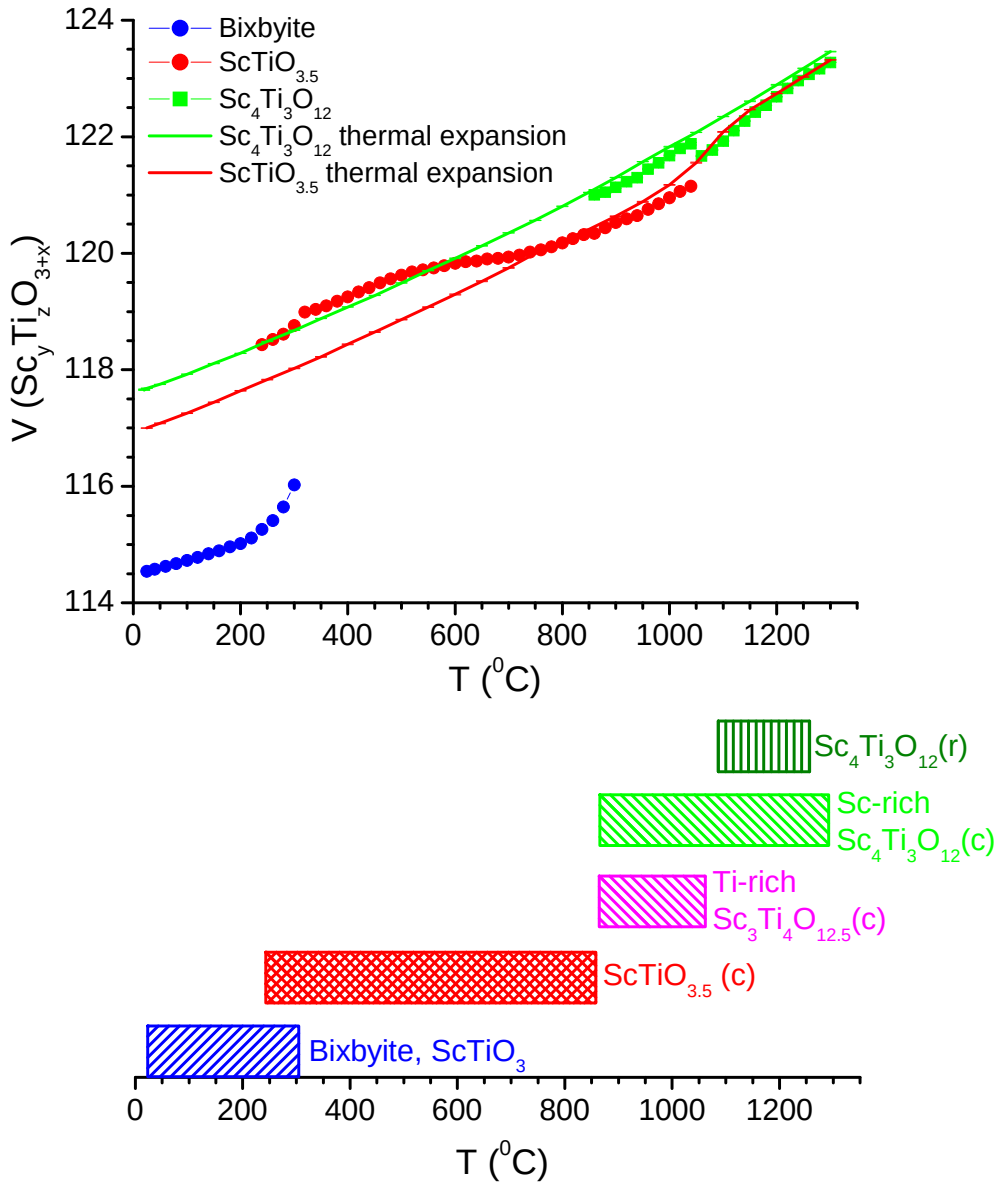

Figure 5.2. (TOP) Formula unit cell volume evolution of cubic $Sc_yTi_zO_{3+x}$ as a function of temperature during the in-situ heating of $ScTiO_3$ in air from 25 to 1300 °C. Blue solid circles = $ScTiO_3$ bixbyite evolution, Red solid circles = $ScTiO_{3.5}$, Green solid rectangles = $Sc_4Ti_3O_{12}$ defect fluorite evolution, Red solid line = thermal expansion for $ScTiO_{3.5}$ and Green solid line = $Sc_4Ti_3O_{12}$ thermal expansion. (BOTTOM) Various phases observed during the in-situ oxidation of $ScTiO_3$ bixbyite and corresponding temperature stability range. For convenience Ti and Sc-rich regimes are represented as $Sc_3Ti_4O_{12.5}$ and $Sc_4Ti_3O_{12}$ respectively for the temperature range T = 860 – 1060 °C. (c) = cubic and (r) = rhombohedral. Adapted from ref. 121.

The phases existing in the temperature range 860 ≤ T ≤ 1060 °C crystallize in the cubic structure in $Fm\bar{3}m$ space group with closely related unit cell dimensions. As can be seen in figure 5.2, the unit cell dimensions of these two cubic phases deviate from the thermal expansion data for $ScTiO_{3.5}$ (red solid line). This is indicative of phase separation of $ScTiO_{3.5}$ forming Sc-rich and Ti-rich defect fluorite phases. The phase having the larger unit cell volume (green solid rectangles) is in agreement with the thermal expansion of $Sc_4Ti_3O_{12}$ (green solid line) which suggests the formation of a Sc-rich phase. On the other hand, the phase with the smaller unit cell volume (red circles) falls below the thermal expansion of $ScTiO_{3.5}$ (red solid line) indicative of a Ti-rich phase. Note that based on the Shannon ionic radii, Sc^{3+} is larger than Ti^{4+} ($Sc^{3+}_{(VI)}$ = 0.745 Å, $Ti^{4+}_{(VI)}$ = 0.605 Å, $Sc^{3+}_{(VIII)}$ = 0.87 Å, $Ti^{4+}_{(VIII)}$ = 0.74 Å), consequently a higher Sc-content would result in a larger unit cell volume. The phases formed due to $ScTiO_{3.5}$ phase separation must be part of the solid solution $Sc_{3+x}Ti_{4-x}O_{12+\delta}$ ($0 < x < 1$) and will be represented as $Sc_3Ti_4O_{12}$ for the Ti-rich phase and $Sc_4Ti_3O_{12}$ for the Sc-rich phase for the remainder of this chapter. Decomposition was evident at T ≈ 940 °C due to the formation of the TiO_2 rutile phase. The loss of TiO_2 is proposed to be occurring from the Ti-rich phase ($Sc_3Ti_4O_{12.5}$) in a continuous fashion until it transforms completely to $Sc_4Ti_3O_{12}$. Note that there is an increase in slope of the unit cell volume (red solid circles to green rectangles) for the Ti-rich phase with the loss of TiO_2 towards the thermal expansion of $Sc_4Ti_3O_{12}$ (green line). The loss of TiO_2 increases the Sc-content and thereby the effective cation radius on the *4a* site due to the increase in Sc^{3+} to Ti^{4+} ratio. The onset of anion-ordered rhombohedral $Sc_4Ti_3O_{12}$ was observed at 1080 °C and this phase exists up to 1240 °C. For this temperature range a 3-phase refinement was carried out with cubic

and rhombohedral $Sc_4Ti_3O_{12}$ as well as TiO_2 rutile phases. For this temperature range, due to severe peak overlaps Sc-rich and Ti-rich phases could not be modeled separately. Consequently there is a slight deviation in the evolution of the unit cell volume of the $Sc_4Ti_3O_{12}$ cubic phase (green rectangles) from the thermal expansion of cubic $Sc_4Ti_3O_{12}$ (green line). The bottom panel of figure 5.2 shows the temperature stability ranges for various phases observed during the in-situ heating of $ScTiO_3$ in air from 25 to 1300 °C. An x-ray diffraction peak (peak height < 6%) observed for $1000 \leq T \leq 1160$ °C at $2\theta \approx 31.7°$ was excluded during the refinements for this temperature regime. This peak matches the hexagonal $Sc_9Ti_{10}O_{31.2}$ (ICDD powder XRD reference code 00-031-1228).

5.2.3. Analysis of Phase Fractions during in-situ Oxidation and Annealing

The phase fraction analysis for the in-situ oxidation and annealing was carried out using Rietveld refinements of the temperature dependent powder x-ray diffraction data. The phase fraction of $Sc_yTi_zO_{3+x}$ (%) is shown in figure 5.3.

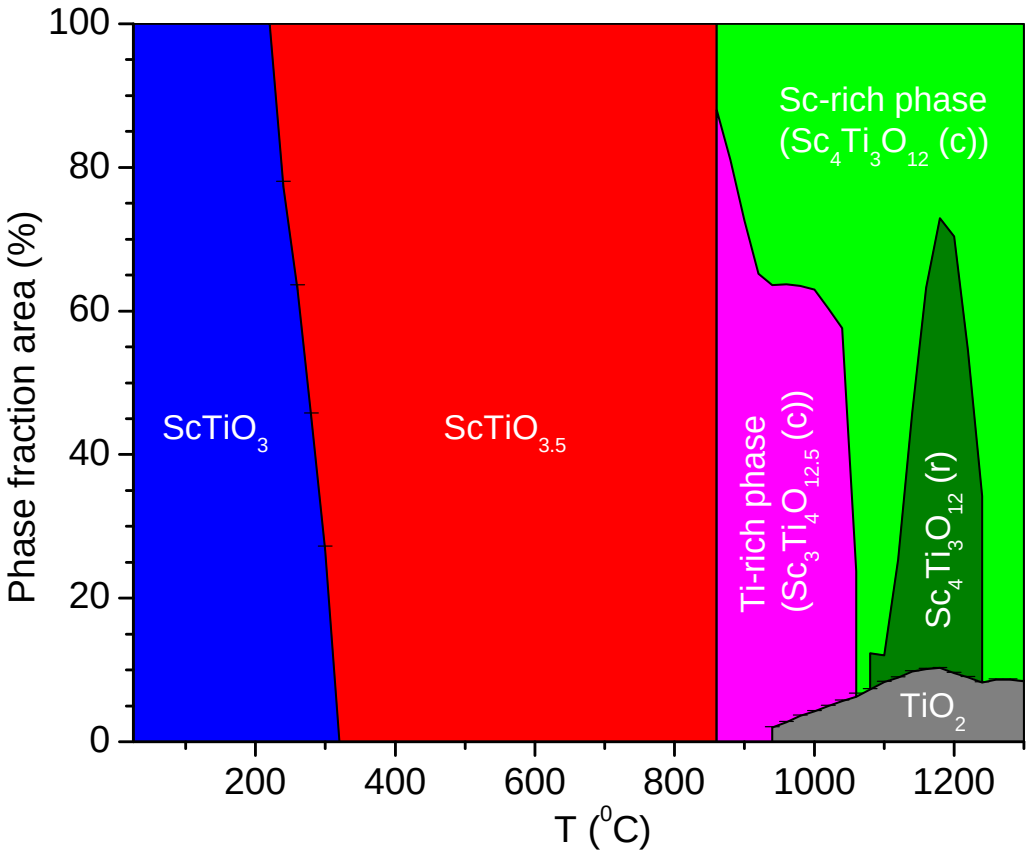

Figure 5.3. Phase fraction of $Sc_yTi_zO_{3+x}$ during the in-situ heating of $ScTiO_3$ in air from 25 to 1300 °C. Blue = $ScTiO_3$, Red = $ScTiO_{3.5}$, Magenta = Ti-rich cubic $Sc_3Ti_4O_{12.5}$, Light green = Sc-rich cubic $Sc_4Ti_3O_{12}$, Dark green = rhombohedral $Sc_4Ti_3O_{12}$ and Gray = TiO_2 rutile. The letters in the parentheses stand for c = cubic and r = rhombohedral. Adapted from ref. 121.

Topotactic oxidation of $ScTiO_3$ begins at 240 °C and all of the starting material (blue region) is oxidized to $ScTiO_{3.5}$ defect fluorite (red region) at 340 °C. The defect fluorite $ScTiO_{3.5}$ (red region) phase is stable up to 840 °C. At 860 °C the defect fluorite phase segregates forming Sc-rich (light green region, conveniently represented as $Sc_4Ti_3O_{12}$ in figure 5.3) and Ti-rich (magenta region, conveniently represented as $Sc_3Ti_4O_{12.5}$ in figure 5.3) cubic phases. With the increase in the temperature, the Ti-rich

phase was found to convert into the Sc-rich phase as we observed that the phase fraction of the Sc-rich phase (light green) increases and that of the Ti-rich (magenta region) phase decreases. This observation is in agreement with the onset of the TiO_2 rutile phase formation at 920 °C. The Ti-rich phase completely transforms to $Sc_4Ti_3O_{12}$ at 1080 °C expelling TiO_2 rutile. A fraction of the cation disordered cubic $Sc_4Ti_3O_{12}$ (light green) was observed to convert to the anion ordered rhombohedral analogue at (dark green) 1080 °C. The rhombohedral phase (dark green) disappears completely at 1260 °C forming the entropically favored cation disordered cubic $Sc_4Ti_3O_{12}$ (light green).

5.2.4. Summary of $ScTiO_3$ Oxidation and Annealing

The complex reaction pathway is summarized below and is presented as a flow chart in figure 5.4.

$ScTiO_3$ bixbyite oxidizes to the $ScTiO_{3.5}$ defect fluorite at 240 °C, the topotactic oxidation is shown as step 'a' in figure 5.4.

$$ScTiO_3 + 0.25O_2 \rightarrow ScTiO_{3.5}\ (240\ °C \leq T \leq 840\ °C) \qquad (\mathbf{a})$$

During the second step 'b + c' in figure 5.4, $ScTiO_{3.5}$ separates into Sc-rich $Sc_4Ti_3O_{12}$ and Ti-rich $Sc_3Ti_4O_{12.5}$. As mentioned previously, the phases formed due to the $ScTiO_{3.5}$ phase separation must be part of the solid solution $Sc_{3+x}Ti_{4-x}O_{12+\delta}$ $(0 < x < 1)$. Note that in this equation $Sc_4Ti_3O_{12}$ represents 'Sc-rich cubic phase' and $Sc_3Ti_4O_{12.5}$ represents 'Ti-rich cubic phase'. The equation is true only when the ratio of $Sc_4Ti_3O_{12}$ to $Sc_3Ti_4O_{12.5}$ is 1:1 and this is used only as a simple model to represent the phase separation. In reality the ratio follows the trend shown in figure 5.3.

$$ScTiO_{3.5} \rightarrow x Sc_4Ti_3O_{12} + (1-x)Sc_3Ti_4O_{12.5}\ (860\ °C \leq T \leq 920\ °C) \qquad (\mathbf{b+c})$$

The phase separation is followed by the loss of TiO_2 rutile from Ti-rich $Sc_3Ti_4O_{12.5}$ resulting in the formation of Sc-rich $Sc_4Ti_3O_{12}$ which is shown as step 'd' in the figure 5.4.

$$(1\text{-}x)Sc_3Ti_4O_{12.5} \rightarrow 0.75(1\text{-}x)Sc_4Ti_3O_{12} + 7/4(1\text{-}x)TiO_2 \ (940\ ^\circ C \leq T \leq 1060\ ^\circ C) \quad (\mathbf{d})$$

The phase transition from anion disordered cubic $Sc_4Ti_3O_{12}$ to the anion ordered rhombohedral analogue occurs at 1080 °C, shown as step 'e' in figure 5.4.

$$Sc_4Ti_3O_{12} + TiO_2 \rightarrow (1\text{-}y)Sc_4Ti_3O_{12}\ (c) + ySc_4Ti_3O_{12}\ (r) + TiO_2\ (1080\ ^\circ C \leq T \leq 1240\ ^\circ C) \quad (\mathbf{e})$$

Finally, the rhombohedral $Sc_4Ti_3O_{12}$ reverts back to the entropically favored cubic structure at T = 1260 °C which is shown as step 'f' in figure 5.4.

$$(1\text{-}y)Sc_4Ti_3O_{12}\ (c) + ySc_4Ti_3O_{12}\ (r) + TiO_2 \rightarrow Sc_4Ti_3O_{12}\ (c) + TiO_2 \quad (1260\ ^\circ C \leq T \leq 1300\ ^\circ C) \quad (\mathbf{f})$$

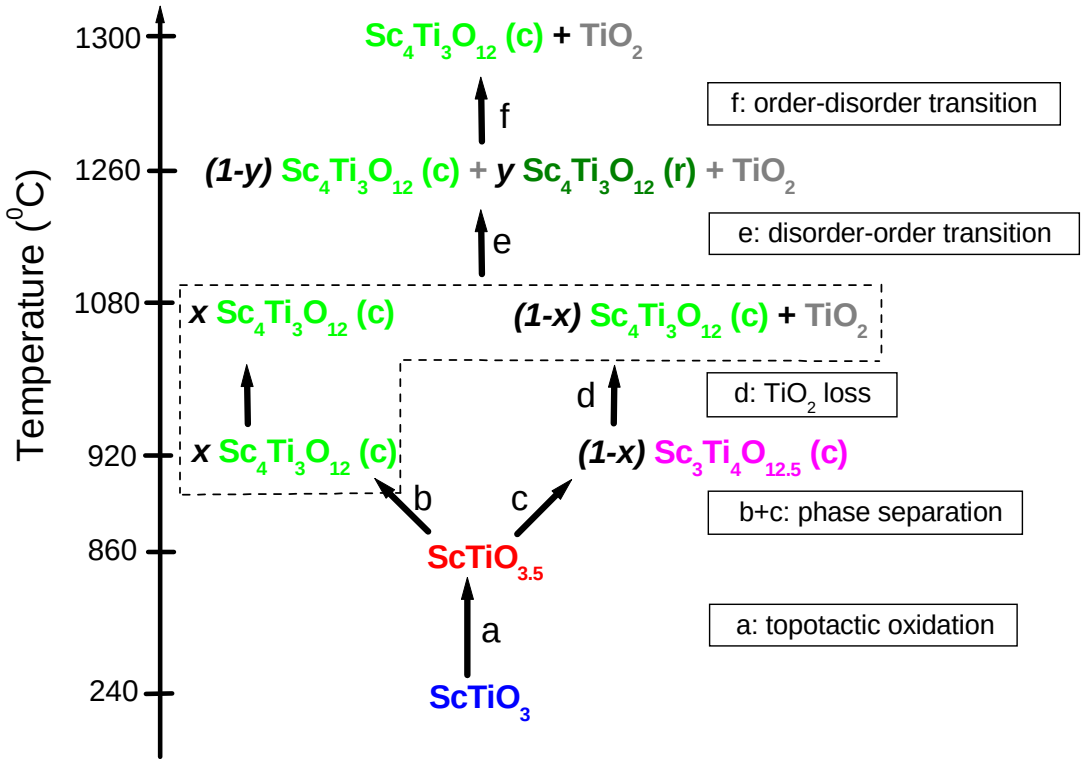

Figure 5.4. Flow chart of the proposed mass unbalanced reaction pathway for $ScTiO_3$ oxidation and annealing. Sc-rich and Ti-rich defect fluorite phases are represented as $Sc_4Ti_3O_{12}$ and $Sc_3Ti_4O_{12.5}$ respectively. The letters in the parentheses stand for (c) = cubic and (r) = rhombohedral. Adapted from ref. 121.

The entire reaction pathway for the $ScTiO_3$ bixbyite oxidation pathway has been analyzed and the complex reaction process involves topotactic oxidation, phase separation and order-disorder phase transition. The findings from the unit cell volume evolution analyses which can be traced back to diffraction peak positions and phase fraction analyses which are based on the diffraction peak intensities are in excellent agreement. The phases with the exception of rhombohedral $Sc_4Ti_3O_{12}$ involved in the reaction process are cubic. This has been advantageous for the detailed analysis of the entire reaction pathway.

The reaction process was further studied using thermogravimetric – differential thermal analyses (TGA/DTA). The TGA/DTA plot in figure 5.5 complements the in-situ x-ray diffraction experiments. The first exothermic peak at 375 °C in the DTA curve and the associated mass gain of 5.33% is in agreement with the oxidation of $ScTiO_3$ to $ScTiO_{3.5}$. The mass gain of 5.33% suggests the product at 800 °C is $ScTiO_{3.47(2)}$. It can be observed in figure 5.5 that the TGA curve plateaus beyond 500 °C which indicates the completion of oxidation. In addition, no further mass change was observed in the TGA curve upon further heating. At higher temperatures various reaction processes such as phase segregation into Sc-rich and Ti-rich phases, formation of TiO_2 rutile and the order-disorder phase transition are occurring as observed in the in-situ x-ray diffraction experiments. The poorly resolved broad feature in the DTA curve at $T \approx 900$ °C is likely due to these reaction processes. The final product obtained after the TGA/DTA experiment was a cubic $Sc_4Ti_3O_{12}$ and TiO_2 rutile mixture.

The appropriate conditions for the bulk synthesis of $ScTiO_{3.5}$ were determined from TGA/DTA and in-situ powder x-ray diffraction experiments. $ScTiO_{3.5}$ can be synthesized by the oxidation of $ScTiO_3$ at 800 °C in air or oxygen for 5 hours. $ScTiO_{3.5}\square_{0.5}$ (where $\square$ represents oxide defects) crystallizes in the fluorite structure with 0.5 oxide defects. The $ScTiO_{3.5}$ defect fluorite structure has a 12.5% oxide defect concentration. The lack of randomization of the oxide defects in the defect fluorite structure $ScTiO_{3.5}$ observed at low temperatures during the in-situ synthesis was overcome significantly during ex-situ synthesis through sufficient annealing.

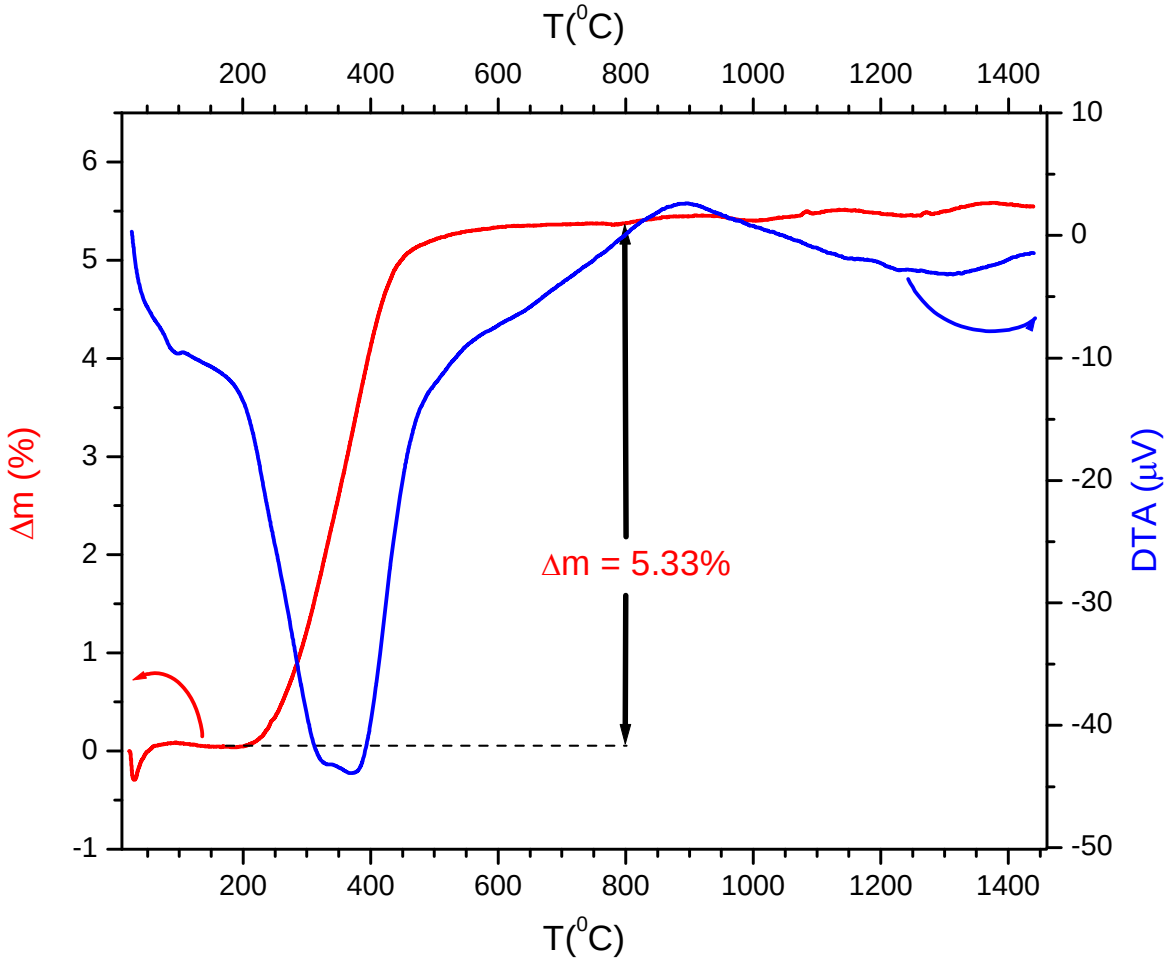

Figure 5.5. TGA/DTA oxidation of $ScTiO_3$ bixbyite in air from 25 to 1450 °C at a heating rate of 20 °C/min. Blue and red lines represent DTA and TGA curves respectively. The solid arrow shows the mass gain observed during the oxidation from room temperature to 800 °C. The dashed line is only a guide to the eye. Adapted from ref. 121.

5.2.5. Structural Analysis of $ScTiO_3$, Topotactic Oxidation Product $ScTiO_{3.5}$ and $Sc_4Ti_3O_{12}$ Phases Involved in the Reaction Process

5.2.5.1. $ScTiO_3$ Structure

The previously published structural analysis of $ScTiO_3$[68] was carried out using powder x-ray diffraction data alone. X-ray diffraction does not provide the required contrast for investigating the extent of Sc^{3+}/Ti^{3+}cation ordering. The contrasting neutron

scattering lengths of Sc (coh b = 12.29 fm) and Ti (coh b = -3.438 fm) allows one to identify the Sc/Ti preference for each of the two cation sites. In addition, the fact that oxygen is a good neutron scatterer (coh b = 5.803 fm) permits the accurate determination of the oxygen sublattice and thereby to obtain reliable coordination polyhedra. The Rietveld refinement was carried out on one powder x-ray and three powder neutron diffraction datasets collected at room temperature. A total of 38 parameters including unit cell parameter, atomic positions, neutron wavelengths, zero point, scale factors, peak shape parameters, temperature factors and site occupancies were refined. Initially the background parameters were fitted with a cubic spline and were held fixed for the subsequent refinement cycles. The Sc/Ti ratios at the two cation positions were refined independently with the total site occupancies constrained to be fully occupied. The Rietveld plots and the structural details are provided in figure 5.6 and table 5.1 respectively. $ScTiO_3$ crystallizes in the cubic structure in $Ia\bar{3}$ (206) space group with a = 9.7099 (4) Å. The site occupancy refinement results from the Rietveld analysis showed a small site preference of Sc^{3+} for *24d* site and a site preference of Ti^{3+} for *8b* site. The *8b* site forms a regular octahedron whereas the *24d* site forms a distorted octahedron. The refined composition $Sc_{0.969(6)}Ti_{1.0259(6)}O_3$ is in good agreement with the nominal composition. The bond valences confirmed Sc^{3+} (BV (*8b* site) = 3.348; site occupancy based on BV = 43%, BV (*24d* site) = 3.226; site occupancy based on BV = 61%) and Ti^{3+} (BV (*8b* site) = 2.742; site occupancy based on BV = 57%, BV (*24d* site) = 2.642; site occupancy based on BV = 39%) site preferences. No indication of cation ordering was observed in $ScTiO_3$ bixbyite.

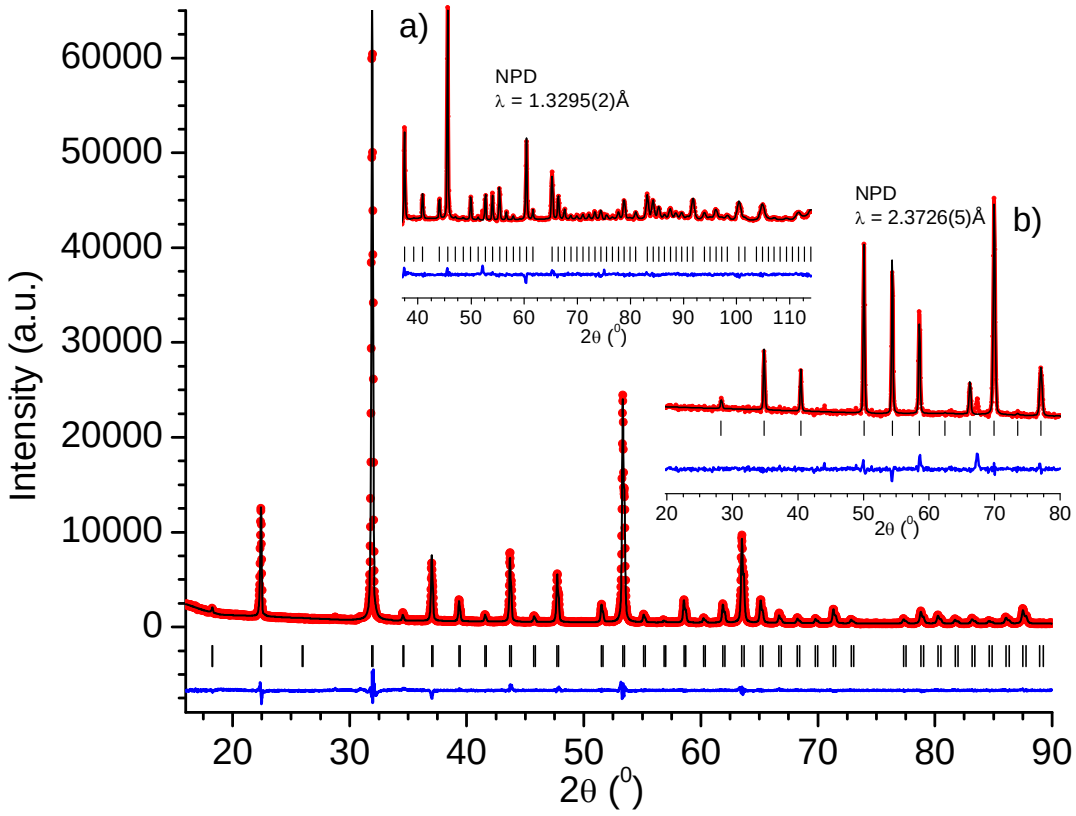

Figure 5.6. Room temperature Rietveld refinement plots for $ScTiO_3$. Powder x-ray diffraction data were collected using Cu $K_{\alpha 1,\,2}$ radiation (λ = 1.54098 Å and 1.544426 Å). Inset: the powder neutron diffractograms were collected using λ = (a) 1.3295 (2) Å and (b) 2.3726 (5) Å. Solid red circles = experimental data, black line = best fit, blue line = difference and black tick marks = Bragg positions. Adapted from ref. 121.

Table 5.1. The structural parameters, bond angles and average bond distances for $ScTiO_3$ bixbyite from the multi histogram Rietveld refinements carried out on one x-ray and three neutron powder diffractograms. The bond valences were determined using VaList.

Composition		$ScTiO_3$
Unit cell content		$Sc_{15.5(1)}Ti_{16.4(1)}O_{48}$
T (K)		295
space group		$Ia\bar{3}$ (206)
unit cell	a (Å) V (Å^3)	9.7099(4) 915.47(7)
Sc/Ti (8b) (¼, ¼, ¼)	B_{iso} (Å^2) Occ. (Sc) Occ. (Ti)	0.76(9) 0.281(5) 0.719(5)
Sc/Ti (24d) (x, 0, ¼)	x/a B_{iso} (Å^2) Occ. (Sc) Occ. (Ti)	0.9665(1) 0.66(5) 0.554(3) 0.446(3)
O (48e) (x, y, z)	x/a y/b z/c B_{iso} (Å^2) Occ. (O)	0.3905(3) 0.1553(2) 0.3812(3) 0.43(4) 1.000 (fixed)
d (Sc(1)/Ti(1))-O (Å) d (Sc(2)/Ti(2))-O (Å)		6 * 2.081(2) 2 * 2.143(2) 2 * 2.108(2)

average d(Sc(2)/Ti(2)-O		2 * 2.040(2) 2.097(2)
Bond valences: BV, site occupancy based on BV, (site occupancy from refinement)	Sc(1) Ti(1) Sc(2) Ti(2)	3.348 43% (0.28) 2.742 57% (0.72) 3.226 61% (0.55) 2.642 39% (0.45)
# of parameters		38
Z		16
R-values:	XRD:* (Rp, Rwp, χ^2) NPD-1:* (Rp, Rwp, χ^2) NPD-2:* (Rp, Rwp, χ^2) NPD-3:* (Rp, Rwp, χ^2)	4.39 / 5.99 / 3.94 2.07 / 2.80 / 4.78 2.18 / 2.95 / 4.64 2.24 / 2.97 / 2.62

* *X-ray: $K_{\alpha 1,2}$, λ= 1.540598 Å, 1.544426 Å, 10° ≤ 2θ ≤ 90 °, Δ2θ= 0.0167°, 4781 data points, weight in refinement = 0.25; NPD-1: λ = 1.3295(2)Å, 4.4° ≤ 2θ ≤ 84 °, Δ2θ= 0.1003°, 795 data points, weight in refinement = 0.25; NPD-2: λ = 1.3295(2)Å, 35.4° ≤ 2θ ≤ 115 °, Δ2θ= 0.1003°, 795 data points, weight in refinement = 0.25 ; NPD-3: λ = 2.3726(5) Å, 4.4° ≤ 2θ ≤ 84 °, Δ2θ= 0.1003°, 795 data points, weight in refinement = 0.25*

5.2.5.2. $ScTiO_{3.5}$ Structure

The multi-histogram Rietveld refinement was carried out on one powder x-ray and one powder neutron diffractogram of $ScTiO_{3.5}$ collected at room temperature. A total of 19 parameters including unit cell parameter, neutron wavelength, zero points, scale factors, peak shape parameters, temperature factors and cation occupancies were refined. During the initial refinement cycles the backgrounds were fitted using a cubic spline and were fixed for the subsequent cycles. The topotactic oxidation product $ScTiO_{3.5}$ crystallizes in the defect fluorite structure in $Fm\bar{3}m$ (225) space group with a =

4.89199(5) Å. The Rietveld plots and structural details such as structural parameters, bond angles and average bond distances are provided in figure 5.7 and table 5.2 respectively. Al_2O_3 corundum was used a thermocouple sleeve for the high temperature measurements. Small impurity peaks from this Al_2O_3 corundum sleeve were observed in the room temperature powder neutron diffractogram for $ScTiO_{3.5}$ and the corresponding Bragg positions are shown as the bottom tick marks in figure 5.7 inset. In the defect fluorite structure the Sc^{3+}/Ti^{4+} cations are arranged on the *4a* (0, 0, 0) site in a disordered fashion and the oxide anions occupy the *8c* (¼, ¼, ¼) site with an occupancy of 0.875. A particularly large temperature factor of 5.15(3) $Å^2$ for oxygen is due to the large oxide defect concentration and the associated disorder on the oxide sublattice in the defect fluorite structure. A broad peak at d ≈ 2.14 Å was observed in the powder neutron diffraction data. This feature is absent in the powder x-ray diffraction data. A similar feature was observed in the powder neutron diffraction patterns for $AVO_{3.5+x}$ (A = In, Sc) and it was proposed that this is due to oxide defect clustering. The bond valences determined using VaList indicated the presence of Sc^{3+} (BV = 3.9) and Ti^{4+} (BV = 3.5) on one site. No indication of superstructure peaks in the powder x-ray and neutron diffractograms rules out ion/defect ordering in the structure.

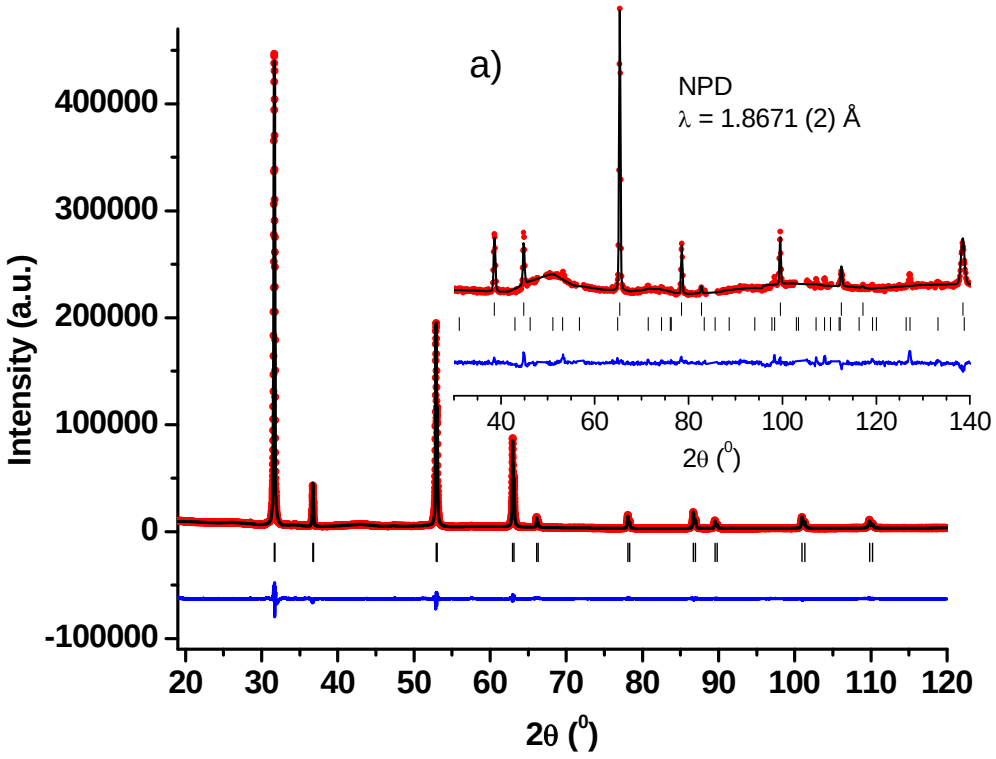

Figure 5.7. Room temperature Rietveld refinement plots for $ScTiO_{3.5}$. Powder x-ray diffraction data were collected using Cu $K_{\alpha 1,2}$ radiation (λ = 1.54098 Å and 1.544426 Å). Inset: the powder neutron diffractogram was collected using λ = 1.8671 (2) Å. In the neutron diffractogram the top and bottom tick marks are $ScTiO_{3.5}$ and Al_2O_3 Bragg positions respectively. Solid red circles = experimental data, black line = best fit, blue line = difference and black tick marks = Bragg positions. Adapted from ref. 121.

Table 5.2. The structural parameters, bond angles and average bond distances for $ScTiO_{3.5}$ defect fluorite from the multi-histogram Rietveld refinements carried out against one x-ray and one neutron powder diffractogram.

Composition		$ScTiO_{3.5}$
Unit cell content		$Sc_{1.94(2)}Ti_{2.05(2)}O_{7.00}$
T (K)		295
space group		$Fm\bar{3}m$ (225)
unit cell	a (Å) V ($Å^3$)	4.89199(5) 117.073(2)
Sc/Ti (4a) (0, 0, 0)	B_{iso} ($Å^2$) Occ. (Sc) Occ. (Ti)	2.43(1) 0.487(5) 0.513(5)
O (8c) (¼, ¼, ¼)	B_{iso} ($Å^2$) Occ.	5.15 (3) 0.875
d (Sc(1)/Ti(1))-O (Å)		8 * 2.118292(4)
# of parameters		19
Z		2
R-values:	XRD:* (Rp, Rwp, χ^2) NPD-1:* (Rp, Rwp, χ^2)	2.90 / 4.30 / 11.6 3.18 / 4.42 / 3.04

* *X-ray: $K_{\alpha 1,2}$ λ= 1.540598 Å, 1.544426 Å, 10º ≤ 2θ ≤ 120 º, Δ2θ= 0.0083º, 13158 data points, weight in refinement = 0.3 ; NPD-1: λ = 1.8671 (2)Å, 0.1º ≤ 2θ ≤ 150.9 º, Δ2θ= 0.1001º, 1508 data points, weight in refinement = 0.7*

In the idealized cubic fluorite structure the cations form a cubic close packed structure with the anions occupying the tetrahedral interstitials. The average oxide defect fluorite structure derived from the parent fluorite structure with one of the eight oxide ions being vacant is shown in figure 5.8. The cations are shown as blue spheres, anions as red spheres and the randomly chosen oxide ion vacancy as a yellow sphere. The structural aspects of the topotactic oxidation of bixbyite to defect fluorite has been already discussed in chapter 3. Topotactic oxidation of $ScTiO_3$ to $ScTiO_{3.5}$ does not require any cation migration. The oxygen uptake during the topotactic oxidation process increases the cation coordination from six in bixbyite to an average coordination number of seven in the defect fluorite structure.

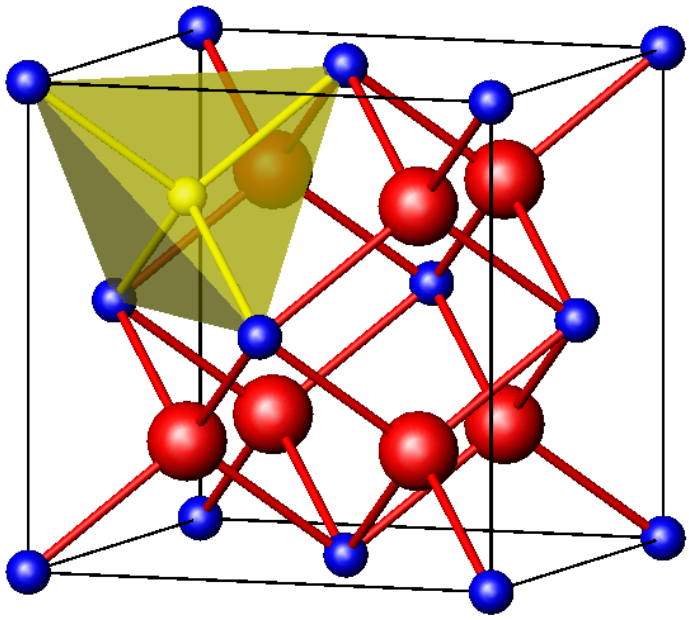

Figure 5.8. $ScTiO_{3.5}$ defect fluorite structure with Sc^{3+}/Ti^{4+} cations as blue spheres and O^{2-} anions as red spheres. The randomly chosen oxygen defect is shown as a yellow sphere in the tetrahedral environment. Adapted from ref. 121.

5.2.5.3. $Sc_4Ti_3O_{12}$ Structure

There are only two entries in the literature and ICSD as well as PDF2003 databases corresponding to the composition $Sc_4Ti_3O_{12}$; a cation-disordered cubic defect fluorite structure and an anion-ordered rhombohedral structure. During the in-situ oxidation of $ScTiO_3$ the diffraction patterns obtained at T ≥ 900 °C matched the cubic fluorite phase $Sc_4Ti_3O_{12}$. The structural characteristics of cubic $Sc_4Ti_3O_{12}$ were established through 2 histogram Rietveld refinements against one powder x-ray and one powder neutron diffraction data set collected on a bulk sample at room temperature. A total of 20 parameters including unit cell parameter, neutron wavelength, zero points, scale factors, peak shape parameters, temperature factors and cation occupancies were refined. The backgrounds were fitted using a cubic spline for initial cycles and were fixed for the subsequent refinement cycles. $Sc_4Ti_3O_{12}$ crystallizes in the cubic defect fluorite structure in space group $Fm\bar{3}m$ (225) with a = 4.90077(4) Å. The Rietveld refinement plots and the structural details are provided in figure 5.9 and table 5.3. The broad feature in the neutron diffractogram (figure 5.9 inset) is due to instrumental background. The normalized volume of the $Sc_4Ti_3O_{12}$ defect fluorite is larger than $ScTiO_{3.5}$ due to the higher Sc^{3+}/Ti^{4+} ratio (Shannon ionic radii Sc^{3+} (VI) = 0.745 Å and Ti^{4+} (VI) = 0.605 Å). The cations Sc^{3+}/Ti^{4+} are arranged on the *4a* (0, 0, 0) site in a disordered fashion and the oxide anions occupy the *8c* (¼, ¼, ¼) site with an occupancy of 0.88. The particularly large temperature factor of 6.91(9) $Å^2$ observed for oxygen is due to the presence of the large defect concentration in the $Sc_4Ti_3O_{12}$ defect fluorite structure. The bond valences determined using VaList indicated the presence of Sc^{3+} (BV = 3.8) and Ti^{4+} (BV = 3.5)

on one site. The composition calculated from the multi-histogram Rietveld refinement is $Sc_{2.16(1)}Ti_{1.84(1)}O_{7.03(4)}$ with Z = 1.

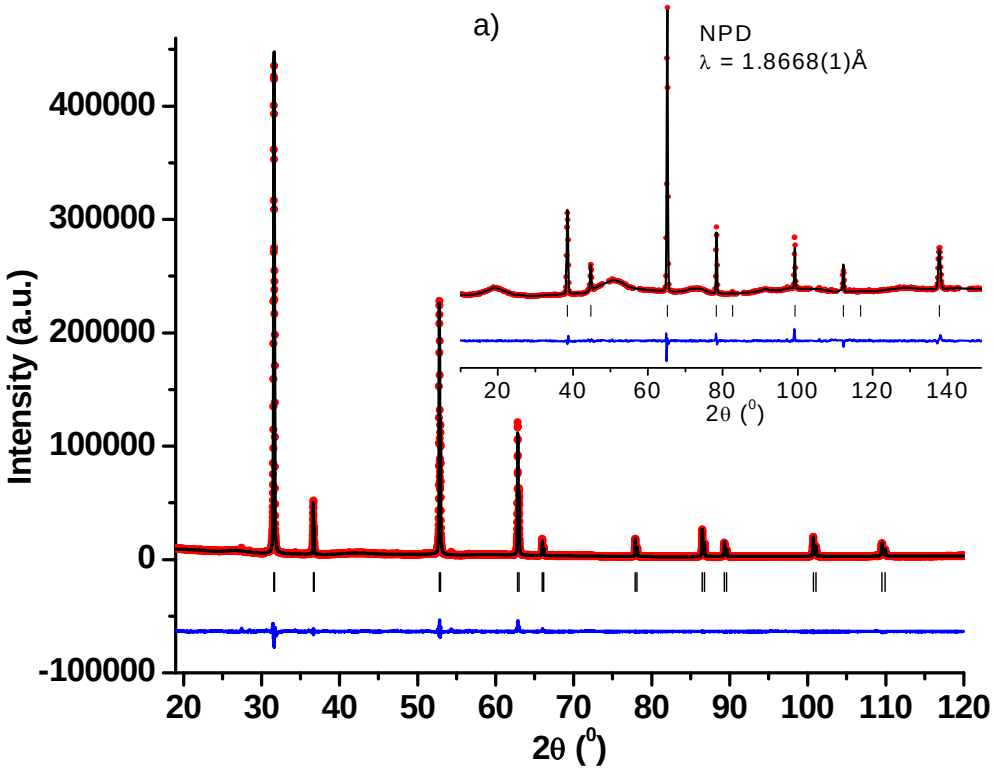

Figure 5.9. Room temperature Rietveld refinement plots for cubic $Sc_4Ti_3O_{12}$. Powder x-ray diffraction data were collected using Cu $K_{\alpha 1,2}$ radiation (λ = 1.54098 Å and 1.544426 Å). Inset: the powder neutron diffractograms were collected using λ = 1.8668 (1) Å. In the neutron diffractogram Pt peaks from the sample container have been excluded from the refinement. Solid red circles = experimental data, black line = best fit, blue line = difference and black tick marks = Bragg positions. Adapted from ref. 121.

Table 5.3. The structural parameters, bond angles and average bond distances for $Sc_4Ti_3O_{12}$ defect fluorite from the multi-histogram Rietveld refinements carried out on one x-ray and one neutron powder diffractograms.

Composition		$Sc_4Ti_3O_{12}$
Unit cell content		$Sc_{2.16(1)}Ti_{1.84(1)}O_{7.03(4)}$
T (K)		295
space group		$Fm\bar{3}m$ (225)
unit cell	a (Å) V (Å^3)	4.90077 (4) 117.705 (1)
Sc/Ti (4a) (0, 0, 0)	B_{iso} (Å^2) Occ. (Sc) Occ. (Ti)	3.28 (2) 0.540(3) 0.460(3)
O (8c) (¼, ¼, ¼)	B_{iso} (Å^2) Occ.	6.91(9) 0.88(2)
d (Sc(1)/Ti(1))-O (Å)		8 * 2.12210(2)
# of parameters		20
Z		1
R-values:	XRD:* (Rp, Rwp, χ^2) NPD-1:* (Rp, Rwp, χ^2)	3.10 / 4.69 / 12.0 2.30 / 3.57 / 4.71

* *X-ray: $K_{\alpha 1,2}$, λ= 1.540598 Å, 1.544426 Å, 10° ≤ 2θ ≤ 120 °, $\Delta 2\theta$= 0.0083°, 13158 data points, weight in refinement = 0.3 ; NPD-1: λ = 1.8668(1)Å, 0.1° ≤ 2θ ≤ 150.9 °, $\Delta 2\theta$= 0.1001°, 1508 data points, weight in refinement = 0.7*

5.2.6. Partial Topotactic Reduction of $ScTiO_{3.5}$ and $Sc_4Ti_3O_{12}$

The defect fluorite phases $ScTiO_{3.5}$ and $Sc_4Ti_3O_{12}$ showed partial reduction of the Ti^{4+} ions under strongly reducing conditions (H_2 gas, 700 °C for $ScTiO_{3.5}$ and CO gas, 1500 °C for $Sc_4Ti_3O_{12}$). The reduction was obvious from x-ray diffraction patterns as well as from the contrasting colors for the pristine samples and the reduced products. Figure 5.10 shows the (111) reflections in the powder x-ray data for $Sc_4Ti_3O_{12}$ and the reduced phase $Sc_4Ti_3O_{12-x}$ as well as their respective sample colors. The two samples are visibly distinguishable as $Sc_4Ti_3O_{12}$ is yellow and the reduced phase $Sc_4Ti_3O_{12-x}$ is black in color. Both the phases produced similar x-ray diffraction patterns that can be indexed on a cubic unit cell with space group $Fm\bar{3}m$, however, obvious peak position shifts were observed. Pristine $Sc_4Ti_3O_{12}$ peaks (red peak) are shifted to lower 2θ angles in comparison to those of $Sc_4Ti_3O_{12-x}$ (green peak). In addition, the x-ray diffraction pattern of the mixture of these two phases showed double peaks (blue pattern in the figure 5.10 inset) indicating different unit cell dimensions for the phases. The TGA/DTA plot for the oxidation of $Sc_4Ti_3O_{12-x}$ is shown in figure 5.11. As can be seen in figure 5.11 the DTA curve showed a single exothermic peak and the TGA curve showed a single-step mass gain. The mass gain of 0.97% during the oxidation indicates the composition of the reduced phase to be $Sc_4Ti_3O_{11.69(2)}$. The reduced phase $Sc_4Ti_3O_{12-x}$ has a smaller unit cell due to the smaller oxygen content in comparison to the fully oxidized $Sc_4Ti_3O_{12}$. This trend of increase in unit cell dimension for larger oxygen content is consistent with the redox beaviour of $AVO_{3.5+x}$ (A = Sc, In) defect fluorite phases discussed in chapter 3. During the in-situ formation of $AVO_{3.5+x}$ (A = Sc, In) phases, unit cell expansion was

observed with the increasing oxygen content rather than cell contraction due to substitution of larger V^{4+} with the smaller V^{5+} cation.

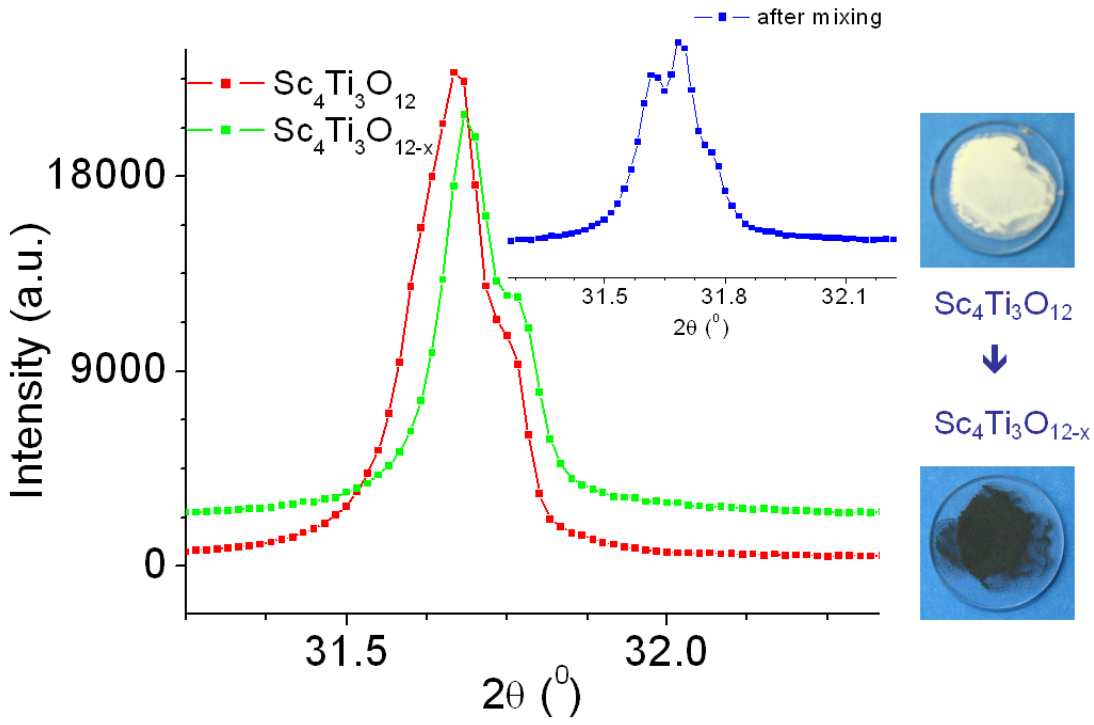

Figure 5.10. Powder x-ray diffraction patterns of $Sc_4Ti_3O_{12}$ (red), $Sc_4Ti_3O_{12-x}$ (green) and the mixture (blue) zoomed in to the (1 1 1) reflection. Powder x-ray diffraction data were collected using Cu $K_{\alpha 1,2}$ radiation (λ = 1.54098 Å and 1.544426 Å).The sample colors of $Sc_4Ti_3O_{12}$ and $Sc_4Ti_3O_{12-x}$ are compared on the right hand side. Adapted from ref. 121.

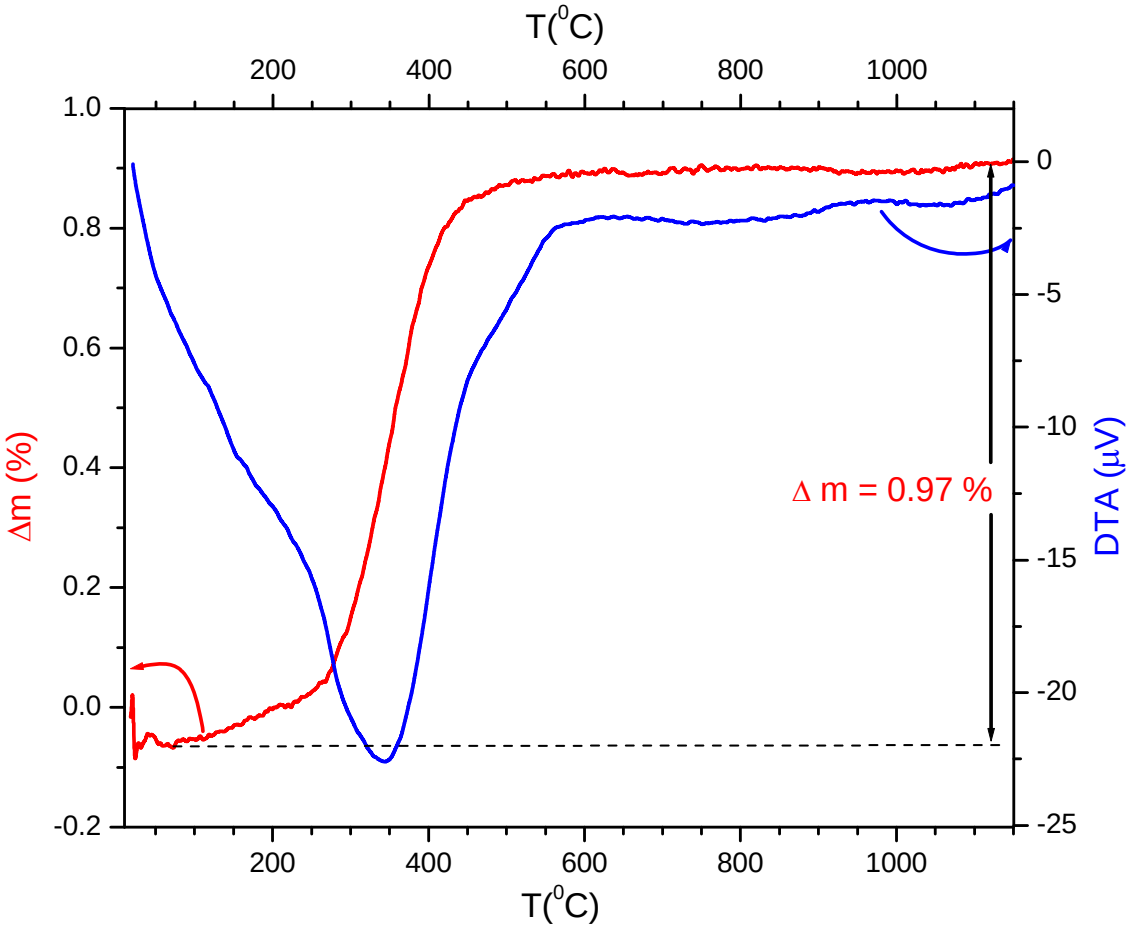

Figure 5.11. TGA/DTA oxidation of $Sc_4Ti_3O_{12-x}$ in air from 25 to 1400 °C with a heating rate of 20 °C/min. Red and Blue lines represent TGA and DTA curves respectively. The solid arrow indicates the mass gain from room temperature to 1100 °C and the dashed line is only a guide to the eye. Adapted from ref. 121.

5.3. Cubic – Rhombohedral Phase Transition in $Sc_4Ti_3O_{12}$

Our continued interest in understanding the structure – reactivity relationship prompted us to further investigate the high temperature phase transition for $Sc_4Ti_3O_{12}$. Single phase cubic defect fluorite $Sc_4Ti_3O_{12}$ was heated from 25 to 1200 °C in air at 100 °C increments followed by isothermal heating at 1200 °C for 6 hours and the process was monitored using in-situ powder x-ray diffraction. Figure 5.12.a shows the in-situ powder x-ray diffraction contour plot for heating cubic $Sc_4Ti_3O_{12}$ in air from 100 to 1200 °C at

100 °C increments and 5.12.c shows the contour plot of isothermal heating at 1200 °C for 6 hours. As can be seen in figure 5.12.a, no indication of new peaks was observed during heating from room temperature to 1200 °C. The only feature observed was the shift of the cubic $Sc_4Ti_3O_{12}$ peaks to lower 2θ diffraction angles due to the thermal expansion. The linear unit cell parameter evolution of the cation-disordered cubic structure (green circles) is plotted in figure 5.12.b. Isothermal heating of the cubic phase at 1200 °C resulted in the appearance of new peaks after 80 minutes as shown in the contour plot in figure 5.12.c. The new peaks can be indexed with a rhombohedral unit cell in space group $R\bar{3}$. The phase fraction analysis for the in-situ isothermal heating was carried out using Rietveld refinements of time dependent powder x-ray diffraction data. The phase fraction (wt.%) of $Sc_4Ti_3O_{12}$ cubic and rhombohedral structures are plotted in figure 5.12.d. With the increase in time cubic $Sc_4Ti_3O_{12}$ (light green) was found to convert to the rhombohedral analogue (dark green). Continued heating for 6 hours did not result in the formation of a single rhombohedral phase. The synthesis of a single rhombohedral phase by the ex-situ heating of the cubic $Sc_4Ti_3O_{12}$ at 1200 °C for 24 – 48 hours was not successful. Our previous study on the $ScVO_3$ bixbyite to perovskite structural conversion had indicated that cation ordering can be achieved through the application of high pressure. Phase pure rhombohedral $Sc_4Ti_3O_{12}$ was synthesized from the cation-disordered cubic analogue at 8 GPa and 1350 °C and the powder x-ray diffractograms of the pristine and the quenched high pressure product are compared in figure 5.13. The inset shows the room temperature diffraction peaks of the two phases for the 2θ range (30.5° - 32°) used for the in-situ contour plots. The similarities between the two plots are very evident with

the cubic phase peak ((111) reflection) at the center of the two rhombohedral phase peaks ((003) and (211) as well as (3-11) reflections).

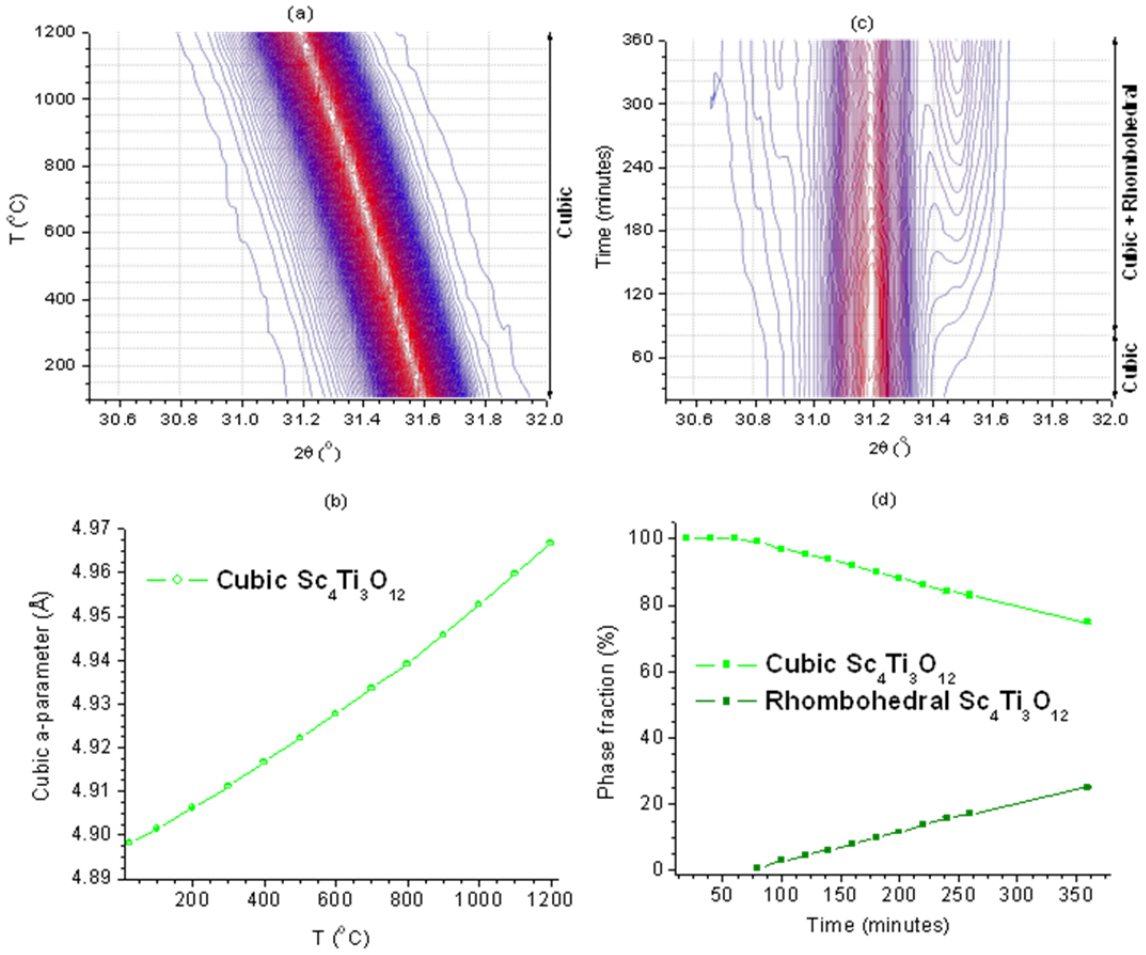

Figure 5.12. (a). In-situ powder x-ray diffraction contour plot of cation disordered cubic $Sc_4Ti_3O_{12}$ heating in air from 100 to 1200 °C at 100 °C increments. (b) Cubic unit cell parameter evolution of defect fluorite $Sc_4Ti_3O_{12}$ from 25 to 1200 °C. (c) In-situ x-ray diffraction contour plot of cubic $Sc_4Ti_3O_{12}$ during isothermal heating at 1200 °C in air with the 20 minute diffraction patterns being measured continuously for 6 hours.(d) Phase fraction of $Sc_4Ti_3O_{12}$ cubic (light green) and rhombohedral (dark green) phases during the isothermal heating of the cubic phase at 1200 °C.

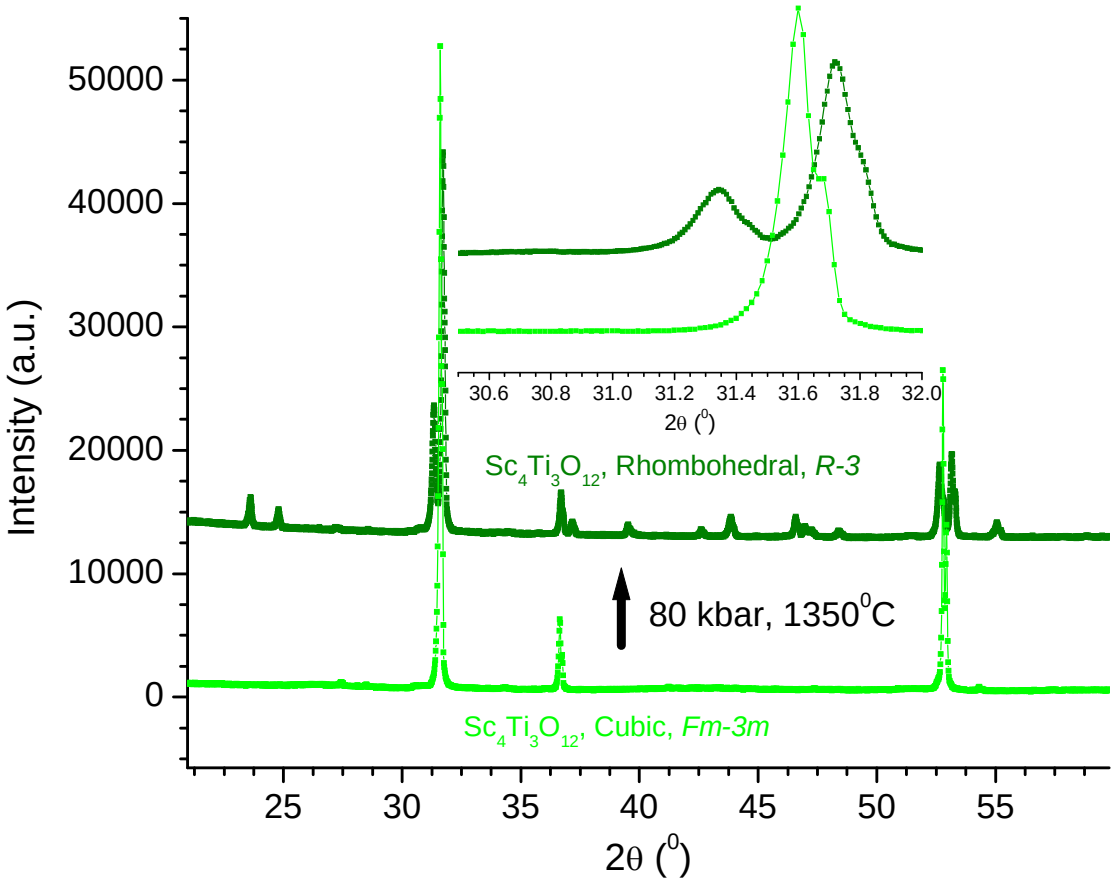

Figure 5.13. Comparison of powder x-ray diffraction patterns of pristine cation-disordered defect fluorite $Sc_4Ti_3O_{12}$ (light green) and the quenched high pressure rhombohedral analogue (dark green). Inset shows the room temperature x-ray diffraction peaks of the two phases for the 2θ range (30.5° - 32°) used for the in-situ contour plot.

5.3.1. $Sc_4Ti_3O_{12}$ Rhombohedral Structure

Structural analysis of the $Sc_4Ti_3O_{12}$ rhombohedral phase prepared through the high pressure - high temperature route was carried out using multi-histogram Rietveld refinements against one powder x-ray and two powder neutron diffraction datasets. X-rays are not an ideal probe for studying Sc^{3+}/Ti^{4+} ordering because of their very similar x-ray form factors whereas neutrons serve as an ideal probe for this due to the excellent contrast between scandium and titanium neutron scattering lengths (Sc (Coh b = 12.29 fm and Ti (Coh b = -3.348 fm)). In addition, neutrons are more sensitive than x-rays to

oxygen, consequently a better understanding of the oxygen sublattice can be achieved. A total of 41 parameters including unit cell parameter, neutron wavelength, zero points, scale factors, peak shape parameters, temperature factors and atomic coordinates were refined. The structural details are listed in table 5.4. High pressure $Sc_4Ti_3O_{12}$ exists in the rhombohedral structure in space group $R\bar{3}$ with a = b = 9.0969(2) Å and c = 8.5374(2) Å (trigonal/hexagonal settings). The cation occupancies were fixed in the structural model used such that Ti^{4+} cations occupy the *3a* site and *18f* site is occupied by Sc^{3+}/Ti^{4+} cations with a 2:1 ratio. In order to understand the extent of cation ordering, different structural models were used in the Rietveld refinement. The rhombohedral structure with cations occupying both the cationic sites in a fully disordered fashion was attempted as a structural model for the Rietveld refinement, the fit obtained was poor. Another structural model used was the rhombohedral structure with partial substitution (≈10%) of scandium on the *3a* site. Most importantly, refining the cation occupancies of the fully cation-disordered rhombohedral structure showed that there is no Sc^{3+} on the *3a* site. The best fit was obtained when the *3a* site is occupied solely by Ti^{4+}. This indicates that Ti^{4+} cations prefer octahedral coordination environment. The structure of the anion ordered rhombohedral $Sc_4Ti_3O_{12}$ is shown in figure 5.14. The octahedral *3a* sites are represented with yellow polyhedra and are solely occupied by Ti^{4+} cations. The *18f* site represented by blue spheres contains disordered Sc^{3+}/Ti^{4+} cations with a 2:1 ratio.

Table 5.4. The structural details for $Sc_4Ti_3O_{12}$ rhombohedral phase from the multi-histogram Rietveld refinements carried out against one x-ray and two neutron powder diffractograms.

Composition		$Sc_4Ti_3O_{12}$
T (K)		295
space group		$R\bar{3}$ (148)
unit cell (trigonal/hexagonal)	a = b (Å) c (Å) V ($Å^3$)	9.0969 (2) 8.5374 (2) 611.85 (2)
Ti (3a) (0, 0, 0)	B_{iso} ($Å^2$) Occ. (Ti)	1.97 (8) 0.16667 (fixed)
Sc/Ti (18f) (0.2943 (2), 0.4121 (1), 0.0179 (1))	B_{iso} ($Å^2$) Occ. Sc Occ. Ti	1.56 (2) 0.66667 (fixed) 0.33333 (fixed)
O1 (18f) (0.3039 (6), 0.4707 (4), - 0.2188 (3))	B_{iso} ($Å^2$) Occ. O1	1.5 (1) 1
O2 (18f) (0.3054 (5), 0.4553 (4),	B_{iso} ($Å^2$)	1.06 (9)

0.2755 (3))	Occ. O2	1
# of parameters		41
Z		3
R-values:	XRD:* (Rp, Rwp, χ^2)	4.91 / 6.63 / 14.9
	NPD-1:* (Rp, Rwp, χ^2)	4.49 / 6.64 / 5.56
	NPD-2:* (Rp, Rwp, χ^2)	3.68 / 5.40 / 5.97

* *X-ray: $K_{\alpha 1,2}$, λ= 1.540598 Å, 1.544426 Å, 5° ≤ 2θ ≤ 148 °, $\Delta 2\theta$= 0.0083°, 17108 data points, weight in refinement = 0.334 ; NPD-1: λ = 1.329 (1)Å, 5° ≤ 2θ ≤ 85 °, $\Delta 2\theta$= 0.1006°, 798 data points, weight in refinement = 0.333; NPD-2: λ = 2.3699(4)Å, 18.50° ≤ 2θ ≤ 98 °, $\Delta 2\theta$= 0.1010°, 789 data points, weight in refinement = 0.333.*

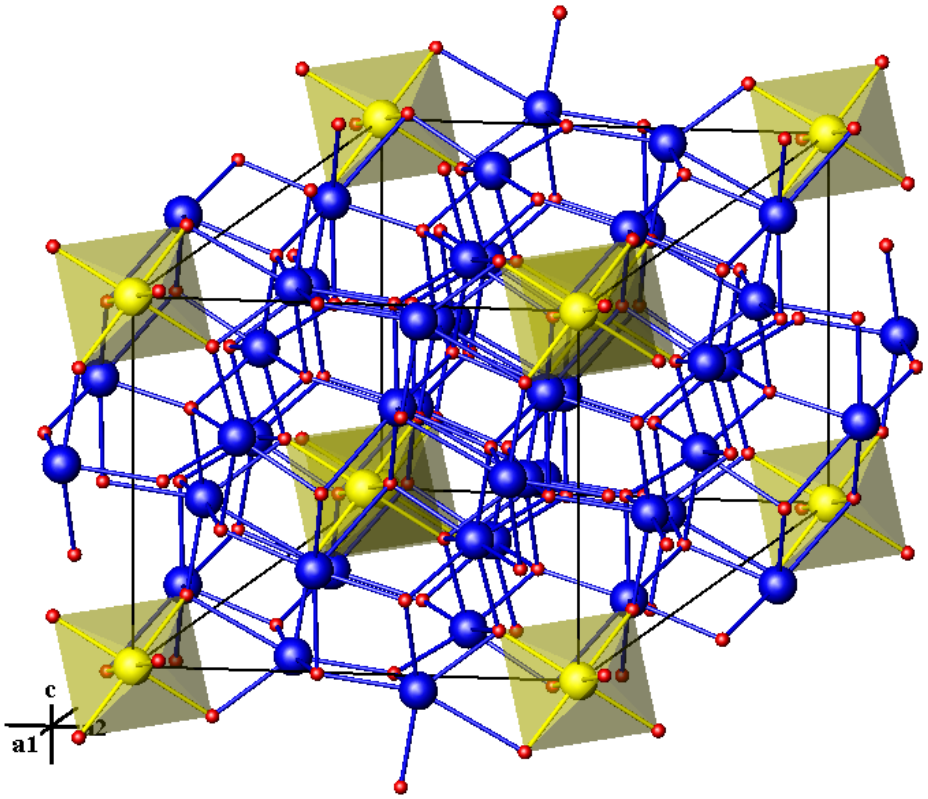

Figure 5.14. Structure of rhombohedral $Sc_4Ti_3O_{12}$ with ordered oxide anions. Octahedral sites (yellow polyhedra) are solely occupied by Ti^{4+}. Blue = Sc^{3+}/Ti^{4+}, red = O^{2-}.

5.4. Summary and Conclusions

The synthesis, stability and the structure of the novel oxygen deficient fluorite phase $ScTiO_{3.5}$ has been reported for the first time. The $ScTiO_3$ bixbyite oxidation pathway has been followed via in-situ powder x-ray diffraction and TGA/DTA experiments. The novel $ScTiO_{3.5}$ defect fluorite structure formation was identified during the topotactic oxidation of $ScTiO_3$ bixbyite and has been compared with the reactivity of vanadium-bearing bixbyite phases such as $InVO_3$ and $ScVO_3$. This study emphasizes a generalized topotactic oxidation pathway for bixbyite phases and consequently illustrates a significant structure – reactivity relation. $ScTiO_{3.5}$ crystallizes in the defect fluorite structure ($Fm\bar{3}m$) with Sc^{3+}/Ti^{4+} disorder on the *4a* site and O^{2-} anions occupying the *8c*

site with 1/8 disordered defects. The average coordination number for both cations in $ScTiO_{3.5}$ is seven. Similar to $AVO_{3.5+x}$ phases, the powder neutron diffraction data suggest possible oxide defect clustering in $ScTiO_{3.5}$. In addition to the initial topotactic oxidation, the in-situ studies revealed a complex equilibrium between cubic $ScTiO_{3.5}$, $Sc_3Ti_4O_{12.5}$ and $Sc_4Ti_3O_{12}$ phases as well as a structural phase transition from the cubic anion-disordered defect fluorite to the anion-ordered rhombohedral structure for $Sc_4Ti_3O_{12}$. At lower temperatures the ion mobility and hence the chemical reactivity is limited to the oxide sublattice. Above this topotactic regime (T > 840 °C) the cations become sufficiently mobile for $ScTiO_{3.5}$ phase separation into Sc-enriched as well as Ti-enriched cubic defect fluorite structures. The phase separation and the phase transitions appear to be driven by the preference of Ti^{4+} for octahedral coordination. This is the case for the TiO_2 rutile structure which is formed as the byproduct during the formation of $Sc_4Ti_3O_{12}$. The $Sc_4Ti_3O_{12}$ rhombohedral structure formed at higher temperatures due to oxide ordering also has an octahedral site which is exclusively occupied by Ti^{4+}. The present study illustrates the potential for controlling the reactivity of sublattices and the corresponding ion mobilities in oxide defect structures which is particularly important for ion conductors and consequently for solid state electrolytes in fuel cell applications.

Chapter 6: Two – Step Formation Pathway of Indium Doped CeO_2

The major part of the research work discussed in chapter 6 encompasses the manuscript 'In-Situ Powder X-ray Diffraction Investigation of Reaction Pathways for the $BaCO_3$-CeO_2-In_2O_3 and CeO_2-In_2O_3 Systems' published in Inorganic Chemistry, volume 49, 2010, pages 1699-1704.[viii] The chapter contains additional data and expanded discussions.

The work described in Chapter 6 was performed in collaboration with the Department of Chemistry at the University of Calgary. The in-situ investigation of 2-step formation pathway for indium doped CeO_2 was first conceived by Dr. V. Thangadurai and Dr. M. Bieringer. All the experiments were designed and conducted by S. P. Shafi. The figures and manuscript drafts were prepared by S. P. Shafi, Dr. M. Bieringer and Dr. V. Thangadurai. All the authors contributed to the revisions and final editing of the manuscript.

[viii] Based on "Bhella, S. S.; Shafi, S. P.; Trobec, F.; Bieringer, M.; Thangadurai, V. Inorg. Chem. **2010**, 49, 1699-1704. Copyright © 2010 American Chemical Society."

Abstract

The $BaCO_3 – CeO_2 – In_2O_3$ and $CeO_2 – In_2O_3$ systems are studied over a wide range of temperatures between 25 and 1200 °C using in-situ powder x-ray diffraction with emphasis on the formation pathway of indium doped CeO_2. The formation pathway of $Ce_{1-x}In_xO_{2-\delta}$ through a CO_2 – capture reaction of the intermediate precursor $BaCe_{1-x}In_xO_{3-\delta}$ perovskite and the chemical stability of the fluorite phases are discussed in detail. The two-step reaction pathway is contrasted with the unsuccessful direct conventional solid state reaction between CeO_2 and In_2O_3. The decomposition of In-doped perovskites under a CO_2 atmosphere is followed using high temperature powder x-ray diffraction which provides insights into the reaction pathway as well as the thermal stability of the $Ce_{1-x}In_xO_{2-\delta}$ systems. In a CO_2 flow, the perovskite phase decomposes into $BaCO_3$ and $Ce_{1-x}In_xO_{2-\delta}$ above 600 °C. The in-situ x-ray diffraction confirmed the metastable nature of In-doped CeO_2 phases as the fluorite-type phases decompose above 800 °C. The unit cell parameter and the domain size of the doped fluorite phases depend upon the indium concentration. The maximum In-doping level for CeO_2 that can be attained through the CO_2 – capture reaction of the $BaCe_{1-x}In_xO_{3-\delta}$ perovskite has been identified. In addition, a preliminary insight into the high temperature structural phase transition for $BaCe_{0.9}In_{0.1}O_{3-\delta}$ is provided.

6.1. Introduction

Oxide ion conductors contain mobile oxide ions and are of immense commercial potential as oxide-ion electrolytes in fuel cells. Most of the commercial solid oxide – ion electrolytes have the fluorite structure with anion vacancies.[122] CeO_2 crystallizes in the fluorite structure and provides ample opportunities for doping with divalent and trivalent cations, forming the solid solutions of $Ce_{1-x}M_xO_{2-\delta}$ (M = Ca, Sr, Ba, Ln = rare earth). In particular, 10 to 20 mol % Ln – doped $Ce_{1-x}Ln_xO_{2-\delta}$ have drawn significant attention because of their high oxide ion conductivity compared to that of Y_2O_3 – doped ZrO_2 (YSZ) and SrO + MgO – doped $LaGaO_3$ (LSGM).[123-127] Despite the fact that CeO_2 has been doped successfully with a variety of divalent and trivalent cations[128-140] ex-situ direct synthesis of indium doped CeO_2 via a conventional high temperature ceramic method (800 – 1500 °C) was not successful. Based on the Shannon ionic radii[141], doping In ($In^{3+}_{(VIII)}$ = 0.92 Å) for Ce ($Ce^{4+}_{(VIII)}$ = 0.97 Å) in the fluorite structure should be feasible as the difference in ionic radii between In^{3+} and Ce^{4+} is almost half compared to that between successfully doped Sm ($Sm^{3+}_{(VIII)}$ = 1.079 Å) and Ce ($Ce^{4+}_{(VIII)}$ = 0.97 Å). In fact, there is strong structural correlation between the CeO_2 fluorite and In_2O_3 bixbyite structures. Removal of two anions along the body diagonal of the cubic fluorite structure will result in the bixbyite structure. Synthesis of In – doped CeO_2 has been carried out via a two-step reaction process including formation of the intermediate perovskite $BaCe_{1-x}In_xO_{3-\delta}$ and subsequent CO_2 – capture reaction. The CO_2 – capture reaction byproduct $BaCO_3$ is removed using an acid wash. Here, we report the in – situ investigation of $BaCe_{1-x}In_xO_{3-\delta}$ (x = 0.1, 0.2 and 0.3) perovskite formation followed by the CO_2 – capture reaction during $Ce_{1-x}In_xO_{2-\delta}$ formation using in – situ powder x-ray diffraction. In

addition, the direct reaction between CeO_2 and In_2O_3 was investigated in-situ and is contrasted with the two – step reaction process.

6.2. Results and Discussion

6.2.1. Direct Reaction between CeO_2 and In_2O_3

The direct reaction between 0.9 mol CeO_2 and 0.05 mol In_2O_3 was studied by means of in-situ powder x-ray diffraction from 25 to 1100 °C in 25 °C increments in air in search of thermodynamic as well as metastable intermediates which might have been overlooked in the past during ex-situ studies. Figure 6.1 represents the corresponding in-situ powder x-ray contour plot.[142] CeO_2 and In_2O_3 peaks shift to lower 2θ angles as can be seen in the contour plot which is consistent with the thermal expansion of the two phases. CeO_2 peaks ((111) and (200) reflections in the contour plot) sharpen above 1000 °C due to crystalline domain size growth. No indication of a reaction is evident as no high temperature intermediates or new phases are observed. Only the starting materials are observed during this experiment and therefore direct In-doping for CeO_2 is not possible using this method.

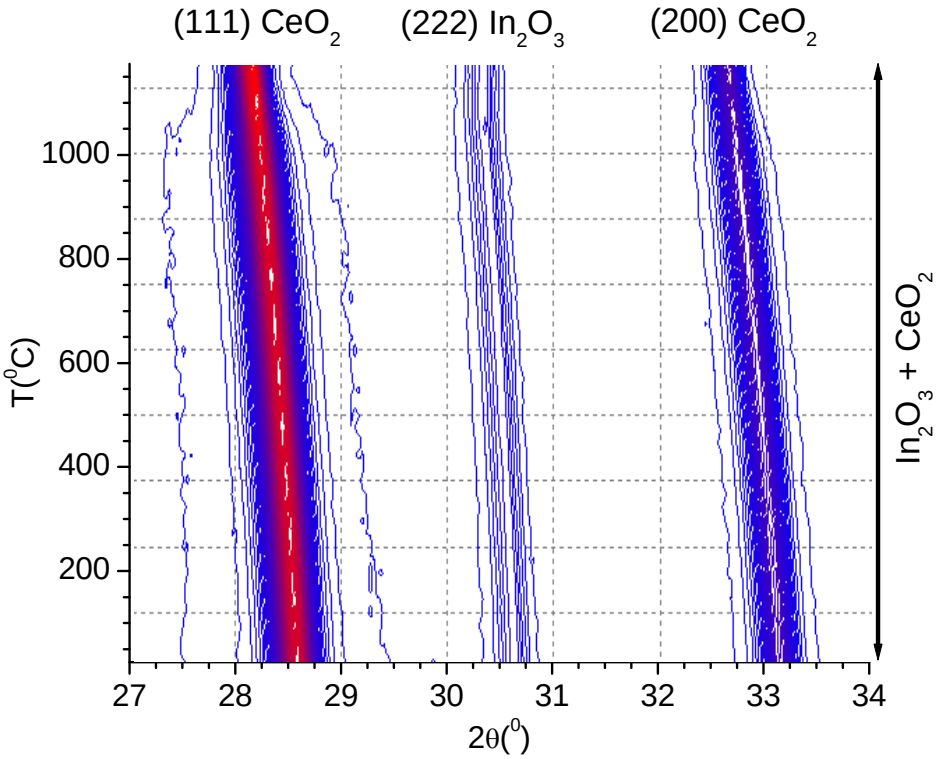

Figure 6.1. In-situ powder x-ray diffraction contour plot illustrating the coexistence of In_2O_3 and CeO_2 between 25 to 1200 °C in air. The peak shifts to lower 2θ angles as a function of temperature are due to thermal expansion and no indication of any reaction was observed. Intensities are shown as constant increments from blue (lowest intensity) to red (highest intensity). Adapted from ref. 142.

6.2.2. Formation of $BaCe_{1-x}In_xO_{3-\delta}$ Perovskites

Synthesis of In-doped CeO_2 can be accomplished through the formation of intermediate perovskite phases $BaCe_{1-x}In_xO_{3-\delta}$ (x = 0.1, 0.2, 0.3). In-situ powder x-ray diffraction has been used to investigate the formation pathway of $BaCe_{1-x}In_xO_{3-\delta}$ perovskites from stoichiometric amounts of starting materials for the temperature range 25 to 1200 °C in 25 °C increments. Figure 6.2. shows the contour plot of temperature dependent powder x-ray diffraction data during the formation of $BaCe_{1-x}In_xO_{3-\delta}$ in air (a. formation of $BaCe_{0.9}In_{0.1}O_{3-\delta}$, b. formation of $BaCe_{0.8}In_{0.2}O_{3-\delta}$ and c. formation of $BaCe_{0.7}In_{0.3}O_{3-\delta}$). The formation pathway for $BaCe_{0.9}In_{0.1}O_{3-\delta}$ shown in figure 6.2.a is

discussed below as a general model for $BaCe_{1-x}In_xO_{3-\delta}$ ($0.1 \leq x \leq 0.3$). Up to T ≈ 750 °C, only the thermal expansion of the starting materials is visible as can be observed in the contour plot in figure 6.2.a. At T = 750 °C the orthorhombic to rhombohedral phase transition for $BaCO_3$ is observed followed by the onset of $BaCe_{0.9}In_{0.1}O_{3-\delta}$ perovskite formation just below T ≈ 900 °C. The diffraction patterns at high temperatures are similar to the cubic undoped $BaCeO_3$. The incorporation of In^{3+} into the perovskite structure can be identified from the in-situ contour plot. At T ≈ 975 °C the In_2O_3 (222) diffraction peak at 2θ ≈ 30.5 ° and the CeO_2 (200) diffraction peak at 2θ ≈ 33 ° disappear simultaneously. The absence of the In_2O_3 peak at T ≥ 900 °C proves the incorporation of In^{3+} into the final perovskite structure. The high temperature perovskite structure showed less than 1 mass% starting material impurities. However, these impurities can be reacted off during the bulk synthesis through prolonged heating. The formation pathway for the perovskites $BaCe_{0.8}In_{0.2}O_{3-\delta}$ and $BaCe_{0.7}In_{0.3}O_{3-\delta}$ are shown in figure 6.2. (b) and (c) respectively. Overall, the general formation pathway is similar to 10 mol% In-doped $BaCeO_3$ formation with slight variations in the formation temperature for the perovskite phases. Another significant feature observed in the contour plots is the appearance of a peak at 2θ ≈ 29.5 ° belonging to a transient phase between T ≈ 800 °C to T ≈ 1050 °C. This transient phase is the Ba_2CePtO_6 double perovskite.[143, 144] Note that the heating filament used during the in-situ experiments is Pt and it appears that it reacted with the perovskite phase forming the double perovskite Ba_2CePtO_6. Further research regarding the formation of the double perovskite and its influence on the formation of the final perovskite structure is currently ongoing in the Bieringer group.[143]

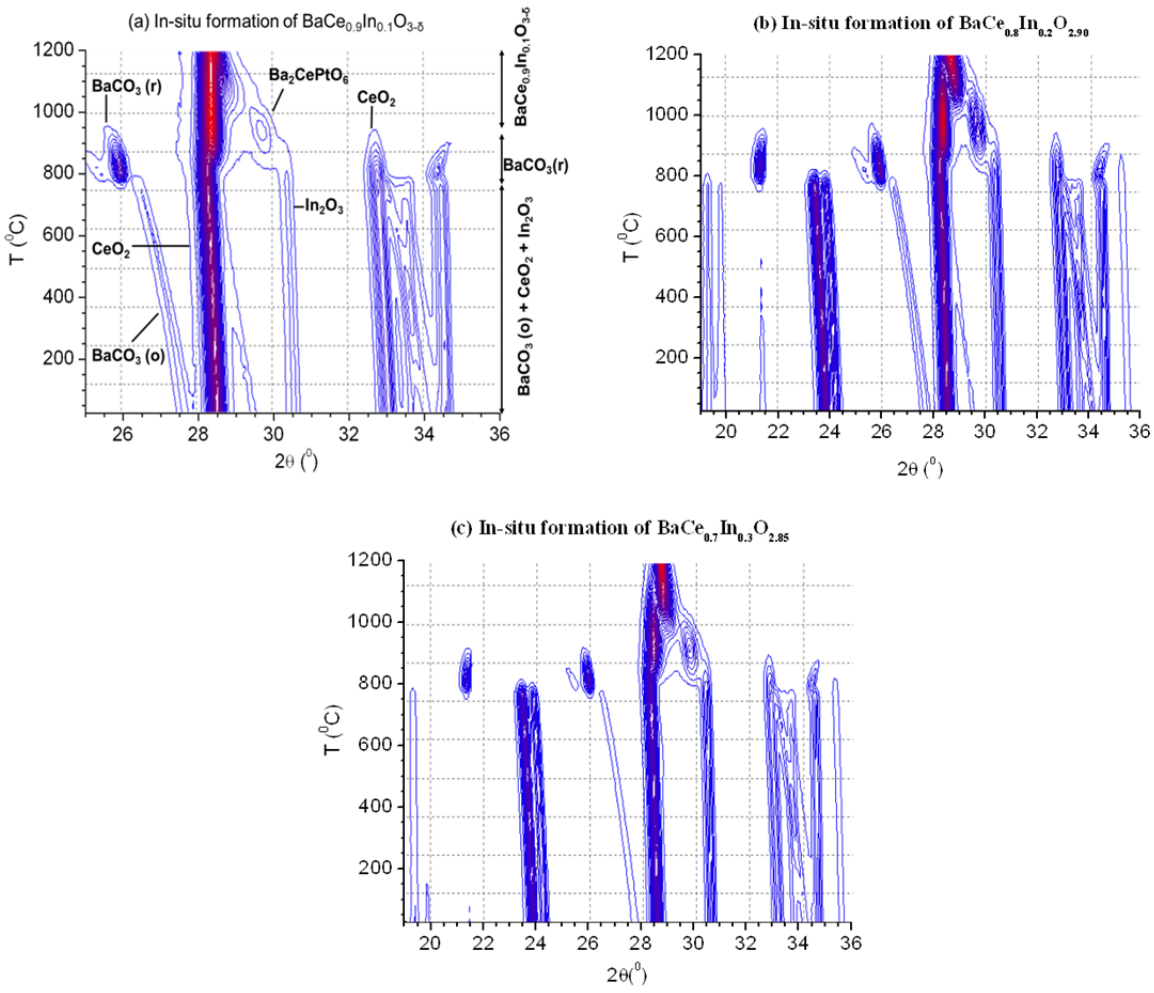

Figure 6.2. In-situ contour plots for the temperature ranges 25 – 1200 °C at 25 °C increments representing the formation of the perovskite $BaCe_{1-x}In_xO_{3-\delta}$ phases during the reaction of $BaCO_3$ – $xCeO_2$ – x/2 In_2O_3 in air. (**a**) formation of $BaCe_{0.9}In_{0.1}O_{3-\delta}$ ($25\ ^\circ \leq 2\theta \leq 36\ ^\circ$), (**b**) formation of $BaCe_{0.8}In_{0.2}O_{3-\delta}$ ($19\ ^\circ \leq 2\theta \leq 36\ ^\circ$) and (**c**) formation of $BaCe_{0.7}In_{0.3}O_{3-\delta}$ ($19\ ^\circ \leq 2\theta \leq 36\ ^\circ$). Intensities are shown as constant increments from blue (lowest intensity) to red (highest intensity).

6.2.3. Carbon Dioxide Capture Reaction

Indium doped barium cerate perovskite precursors were heated under a CO_2 atmosphere in search of In-doped CeO_2 and the reactions were followed via in-situ powder x-ray diffraction. Figure 6.3.a shows the in-situ powder x-ray diffraction contour

plot of CO_2 – capture reaction carried out on $BaCe_{0.9}In_{0.1}O_{3-\delta}$. The diffraction peaks of all the phases observed are color coded in figure 6.3.a and are shown as individual area outlines in figure 6.3.b for improved clarity. The decomposition of the perovskite phase $BaCe_{0.9}In_{0.1}O_{3-\delta}$ is evident due to the appearance of the orthorhombic $BaCO_3$ phase at T = 475 °C. The decomposition of the perovskite phase results in the formation of the $Ce_{0.9}In_{0.1}O_{2-\delta}$ fluorite phase. The fluorite phase $Ce_{0.9}In_{0.1}O_{2-\delta}$ is found to be stable up to 825 °C. Further heating leads to the decomposition of the doped fluorite phase into CeO_2 and In_2O_3. Even though there is strong overlap between the peaks of In-doped CeO_2 and undoped CeO_2 due to their similar structures with only slightly different unit cell parameters, the decomposition is evident due to the appearance of the (222) reflection of the In_2O_3 phase at $2\theta \approx 30.5$ ° as shown in the contour plot. At 800 °C the structural phase transition of $BaCO_3$ from orthorhombic to rhombohedral is observed and at even higher temperatures $BaCO_3$ exists in the cubic structure. At high temperatures it appears that there is an equilibrium between $BaCO_3$ and small amounts of BaO. The In_2O_3 phase disappears at 1100 °C and this coincides with the re-formation of the In-doped perovskite phase $BaCe_{0.9}In_{0.1}O_{3-\delta}$. The formation pathway for In-doped $BaCeO_3$ illustrated a complex reaction pathway.

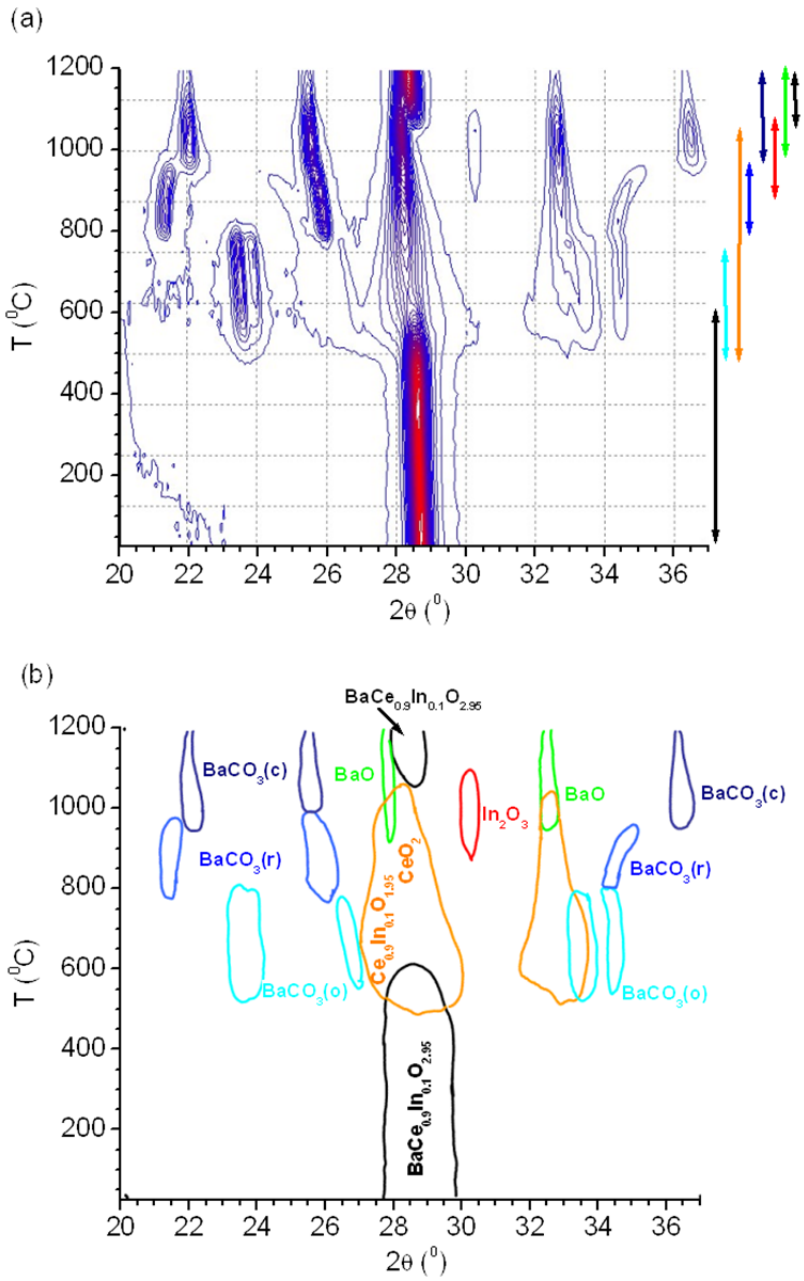

Figure 6.3. (**a**) In-situ contour plots for the temperature ranges 25 – 1200 °C at 25 °C increments representing the evolution of $Ce_{0.9}In_{0.1}O_{2-\delta}$ during decomposition of the perovskite $BaCe_{0.9}In_{0.1}O_{3-\delta}$ under CO_2 atmosphere. Intensities are shown as constant increments from blue (lowest intensity) to red (highest intensity).The color codes shown in figure (**a**) are in accordance with the phase identification contour plot (**b**). Each phase is represented by an individual color and label. The letters in the parentheses for $BaCO_3$ stand for (o) = orthorhombic, (r) = rhombohedral and (c) = cubic. Adapted from ref. 142.

The complex reaction sequence with the final re-formation of the perovskite phase is illustrated by a proposed mass unbalanced reaction shown as scheme 6.1. The letters in the parentheses for $BaCO_3$ stand for (o) = orthorhombic, (r) = rhombohedral and (c) = cubic. The in-situ powder x-ray diffraction experiments illustrate that at high temperatures $BaCO_3$ decomposes, forming BaO and it reacts with readily available In_2O_3 and CeO_2 re-forming the perovskite phase $BaCe_{0.9}In_{0.1}O_{3-\delta}$ which is now the thermodynamically stable product.

$$BaCe_{0.9}In_{0.1}O_{2.95} + CO_2 \xrightarrow{475^0C} Ce_{0.9}In_{0.1}O_{1.95} + BaCO_3(o) \xrightarrow{800^0C} \xrightarrow{800^0C} Ce_{0.9}In_{0.1}O_{1.95} + BaCO_3(r) \xrightarrow{825^0C} 0.9CeO_2 + 0.1In_2O_3 + BaCO_3(r) \xrightarrow{900^0C} \xrightarrow{900^0C} 0.9CeO_2 + 0.1In_2O_3 + BaCO_3(c) + BaO \xrightarrow{1100^0C} \xrightarrow{1100^0C} BaCe_{0.9}In_{0.1}O_{2.95} + CO_2 + \text{minor amounts of unreacted} CeO_2 + In_2O_3 + BaCO_3(c) \quad (6.1)$$

The reaction times during the in-situ experiments are short which result in slightly higher decomposition temperatures for In-doped CeO_2 phases in comparison to the 6 h bulk synthesis. Figure 6.4 shows the isothermal decomposition of $Ce_{0.7}In_{0.3}O_{2-\delta}$ in a CO_2 atmosphere at 800 °C followed in 20 min increments. The onset and growth of the In_2O_3 phase is readily visible due to the appearance of the corresponding (222) reflection at $2\theta \approx 30.5$ ° indicated by the arrow in the figure. For the successful bulk synthesis of 30 mol% In-doped CeO_2 via CO_2 – capture reaction, the temperature has to be lowered to 700 °C in order to avoid decomposition into In_2O_3 and CeO_2. The fluorite $Ce_{1-x}In_xO_{2-\delta}$ phases with lower In-content ($x \leq 0.2$) are stable up to 800 °C.

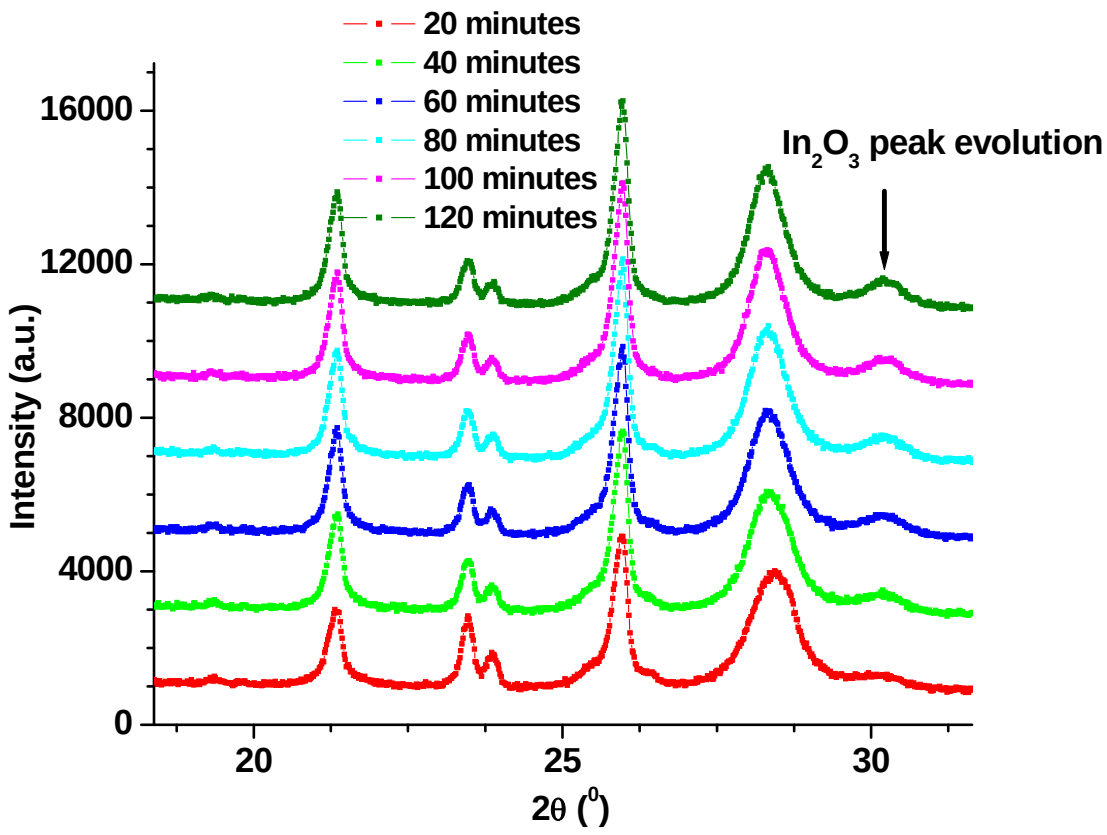

Figure 6.4. Powder x-ray diffraction patterns obtained during the isothermal heating of $BaCe_{0.7}In_{0.3}O_{3-\delta}$ under CO_2 atmosphere at 800 °C. Adapted from ref. 142.

6.2.4. Evolution and Stability of $Ce_{1-x}In_xO_{2-\delta}$ (x = 0.1, 0.2 and 0.3)

Structural analyses of In-doped CeO_2 phases $Ce_{1-x}In_xO_{2-\delta}$ (x = 0.1 – 0.3) were carried out using Rietveld refinements of powder x-ray diffraction data collected at room temperature. The Rietveld refinement plot for $Ce_{0.7}In_{0.3}O_{2-\delta}$ and the refinement results for $Ce_{1-x}In_xO_{2-\delta}$ (x = 0.1 – 0.3) are provided in figure 6.5 and table 6.1. Indium doped CeO_2 crystallizes in the cubic fluorite structure in space group $Fm\bar{3}m$ (225) with Ce^{4+}/In^{3+} occupying the 4*a* (0,0,0) site in a disordered fashion and oxide anions located on the 8*c* (¼, ¼, ¼) site with disordered oxide defects. A total of 25 to 26 parameters were refined including unit cell constants, scale factors, pseudo-Voigt peak shape parameters and peak

asymmetry. The background was described with linear interpolation between 17 refined background parameters. The Shannon ionic radii at the 8-fold oxygen coordination number (CN) of $Ce^{4+}_{(VIII)}$, $In^{3+}_{(VIII)}$ and $O^{2-}_{(IV)}$ predict the bond distances *d*(Ce-O) = 2.35 Å and *d*(In-O) = 2.30 Å. This is in good agreement with the values obtained from the Rietveld refinements (Table 6.1). The phase fraction of In_2O_3 was found to be ≤ 1% up to x = 0.3 for $Ce_{1-x}In_xO_{2-\delta}$.

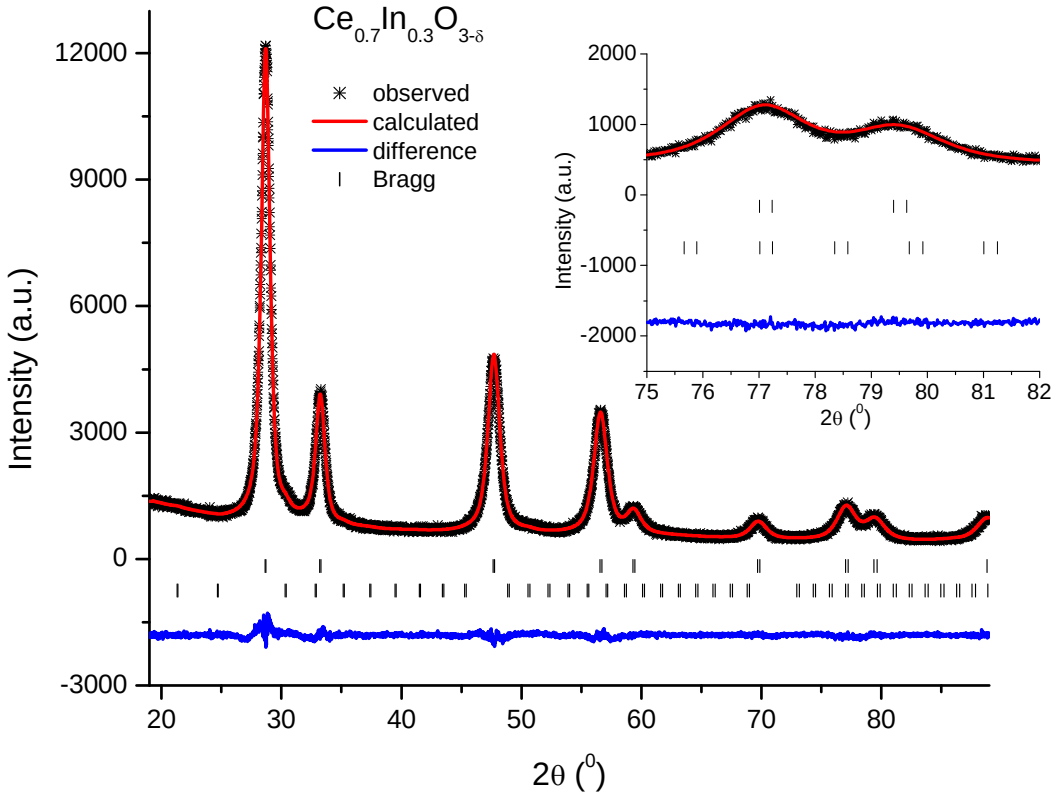

Figure 6.5. Room temperature Rietveld plot of $Ce_{0.7}In_{0.3}O_{2-\delta}$. The powder x-ray diffraction data were collected with $CuK\alpha_{1,2}$ (λ = 1.540598, 1.544426 Å) radiation. Black crosses = experimental data, red line = best fit, blue line = difference, upper tick marks = Bragg positions of $Ce_{0.7}In_{0.3}O_{2-\delta}$ and lower tick marks = In_2O_3 Bragg positions. Adapted from ref. 142.

Table 6.1. Crystallographic details for $Ce_{1-x}In_xO_{2-\delta}$ at room temperature from Rietveld refinements of powder x-ray diffraction. The powder x-ray diffraction data were collected with $CuK\alpha_{1,2}$ (λ = 1.540598, 1.544426 Å) radiation.

x	**0**	**0.1**	**0.2**	**0.3**	**0.35**	**0.4**
a-axis (Å)	5.4173(2)	5.4116(3)	5.4030(4)	5.3932(6)	5.3917(6)	5.3942(8)
cell volume ($Å^3$)	158.982(8)	158.48(2)	157.73(2)	156.87(3)	156.74(3)	156.95(3)
d(Ce/In)-O (Å)	2.34574(8)	2.3433(1)	2.3396(2)	2.3353(3)	2.3347(3)	2.3357(4)
In_2O_3 (mass%)	0	<1.0	<1.0	1.0	7	16
R_p:	3.62	3.50	2.90	3.05	3.05	3.20
R_{wp}:	4.71	4.46	3.69	3.86	3.83	4.08
χ^2:	2.76	2.32	1.88	1.72	1.93	2.19
# of parameters	25	25	25	25	26	26
# of data points	4247	4247	4247	4247	4247	4247

Ce^{4+}/In^{3+} are disordered on the 4a (0, 0, 0) site and O^{2-} located at the 8c (¼, ¼, ¼) site. Single-phase refinements were carried out for $x < 0.3$ with 25 refined parameters and 2-phase refinements for $x \geq 0.3$ with 26 refined parameters.

The variation of the cubic unit cell parameter for the defect fluorite $Ce_{1-x}In_xO_{2-\delta}$ as a function of the nominal indium content is plotted in figure 6.6. It is clear from the figure that the unit cell of the defect fluorite phases $Ce_{1-x}In_xO_{2-\delta}$ contracts with the

increase in the indium content. This is expected as according to the Shannon ionic radii In^{3+} (8-fold = 0.92 Å) is smaller than Ce^{4+} (8-fold = 0.97 Å) and the concentration of oxide ions reduces with increasing substitution of In^{3+} for Ce^{4+}. The In-doped defect fluorite $Ce_{1-x}In_xO_{2-\delta}$ can be successfully synthesized with only minor traces (<1.0%) of In_2O_3 impurities. Further doping of In ($x > 0.3$) in $Ce_{1-x}In_xO_{2-\delta}$ resulted in two-phase products consisting of $Ce_{0.7}In_{0.3}O_{2-\delta}$ and excess In_2O_3 which is illustrated for x = 0.35 and 0.4 in figure 6.6 and table 6.1. There is no significant change in the unit cell dimensions beyond $x = 0.3$ indicating that this is the maximum In-content that can be achieved in $Ce_{1-x}In_xO_{2-\delta}$ prepared via the CO_2-capture reaction.

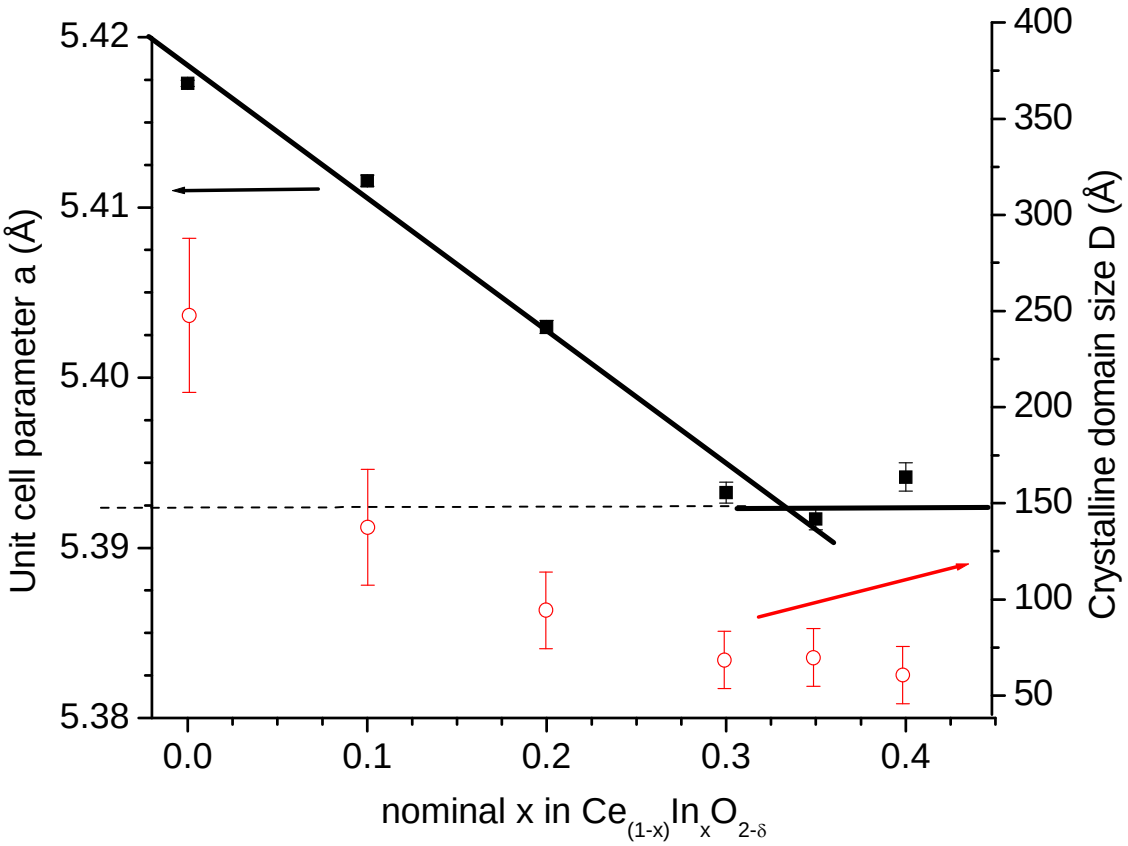

Figure 6.6. Evolution of the cubic unit cell parameter for $Ce_{1-x}In_xO_{2-\delta}$ (black squares) is plotted against the nominal In-content (x).The samples with nominal compositions x = 0.35 and x = 0.4 contain In_2O_3 as a second phase. Isotropic crystalline domain size evolution in $Ce_{1-x}In_xO_{2-\delta}$ is represented by open red circles. The solid black lines are only a guide to the eye. Adapted from ref. 142.

The diffraction peaks of the In-doped phases show broadening with increasing In-content. This is due to the decrease in crystalline domain sizes and no significant strain induced broadening has been observed. The isotropic crystalline domain sizes were calculated using the Scherrer equation (Eq. 6.1) shown below.

$$D = 0.9\lambda/(B\cos\theta) \qquad \text{(Eq. 6.1)}$$

where D is the domain size, B the integral breadth, λ the wavelength and θ the diffraction angle. Contributions from the instrumental broadening have been corrected for the

estimate of the isotropic domain size using the Scherrer equation. The evolution of the isotropic domain sizes for the fluorite phases are plotted as red open circles against the nominal In-content *x* in figure 6.6. The pristine CeO_2 starting material has a crystalline domain size in excess of 600 Å. The perovskite $BaCeO_3$ was synthesized and it was subjected to CO_2-capture reaction. The resulting undoped CeO_2 shows nanosized crystalline domain sizes of 250(40) Å. It can be seen in figure 6.6 that upon indium doping the domain sizes decrease monotonically from $x = 0$ to $x = 0.3$ and plateau beyond $x = 0.3$. Notably the crystalline domain size and the cubic unit cell parameter plateau simultaneously at $x \geq 0.3$ with a crystalline domain size D = 70 (15) Å. There is clear evidence for the fact that the domain sizes are controlled by the indium content in the CeO_2 fluorite phase and are only limited by the stability range of the fluorite-type phases.

6.2.5. CO_2-capture Reaction vs. $Ce_{1-x}In_xO_{2-\delta}$ Decomposition

Carbon dioxide capture reactions of the perovskite precursors require temperatures from 600 to 700 °C for the formation of pure bulk samples of $Ce_{1-x}In_xO_{2-\delta}$ ($x = 0.1 – 0.3$). The In-doped fluorite samples are found to undergo decomposition into their binary oxides at T ≈ 800 °C for $x < 0.3$ and at T ≤ 700 °C for $x \geq 0.3$. The in-situ powder x-ray diffraction experiments monitoring the CO_2 – capture reactions provide intriguing insights into the formation temperatures (T_{form}) of $Ce_{1-x}In_xO_{2-\delta}$. The T_{form} for $x = 0.1$ and 0.2 is 475 °C, for $x = 0.3$ T_{form} is 500 °C. The decomposition temperatures (T_{decomp}) of $Ce_{1-x}In_xO_{2-\delta}$ for $x = 0.1$, 0.2 and 0.3 are 825, 800 and 775 °C respectively which is determined by the first appearance of In_2O_3 during the in-situ experiments. In order to obtain pure bulk samples of $Ce_{1-x}In_xO_{2-\delta}$, the CO_2-capture reactions have to be carried out approximately 100 °C above the formation temperature T_{form}. The formation and

decomposition temperatures converge towards each other with the increase in the indium doping levels. Hence, a maximum value for In-doping is observed for the preparation of $Ce_{1-x}In_xO_{2-\delta}$ using the CO_2-capture reaction. Based on this finding, we propose that larger indium concentrations in CeO_2 can only be achieved if an intermediate precursor is used which can form the $Ce_{1-x}In_xO_{2-\delta}$ phases at low temperatures. It should be noted that all the reported $Ce_{1-x}In_xO_{2-\delta}$ phases are metastable and consequently can only be accessed through low temperature preparation routes. This explains why the direct reaction between CeO_2 and In_2O_3 shown as a contour plot in figure 6.1 was unsuccessful. The direct reaction has to occur below T ≈ 825 °C for the formation of $Ce_{1-x}In_xO_{2-\delta}$ due to the metastability of these phases. The cation mobilities are insufficient for the direct reaction to succeed at such low temperatures.

6.2.6. Structural Phase Transition in $BaCe_{0.9}In_{0.1}O_{3-\delta}$ perovskite

This section provides preliminary insights into the structural phase transition for the $BaCe_{0.9}In_{0.1}O_{3-d}$ perovskite phase. The perovskite $BaCe_{1-x}In_xO_{3-\delta}$ for $x \leq 0.3$ phases exist in either an orthorhombic or a monoclinic structure at room temperature. It is worth drawing attention to the fact that the parent compound $BaCeO_3$ is reported[72,73] to undergo three structural phase transitions between room temperature and 1273 K: (i) from room temperature to 563 K it is orthorhombic with space group *Pnma*; (ii) 563K, second-order phase transition to another orthorhombic phase with space group *Imma*; (iii) first-order transition to a rhombohedral phase with space group $R\bar{3}c$ at 673 K and (iv) a cubic phase with space group $Pm\bar{3}m$ formation at 1173 K. Phase identification and in depth structural analysis have been carried out using neutron powder diffraction by Knight, K. S.[72,73] In-situ powder x-ray diffraction experiments were carried out in air to probe the structural

phase transitions in $BaCe_{1-x}In_xO_{3-\delta}$ perovskites. Figure 6.7 represents the in-situ x-ray diffraction contour plot of $BaCe_{0.9}In_{0.1}O_{3-d}$ from 25 to 1200 °C at 25 °C intervals during heating (a) and cooling (b) cycles. Up to 175 °C, the perovskite phase can be indexed on an orthorhombic structure with space group *Pnma*. Between 200 and 325 °C the diffraction peaks are very broad in comparison to those at 175 and 350 °C which indicate the onset of a phase transition and the existence of multiple phases. The diffraction patterns between 200 and 325°C cannot be indexed with a single space group. The diffraction patterns indicated the possibility for a structural transition from orthorhombic *Pnma* to another orthorhombic phase at low temperatures. The superstructure peaks are too weak to make an explicit statement regarding this phase transition using powder x-ray diffraction. For the intermediate temperature range a single rhombohedral phase ($R\bar{3}c$) was observed. Two possible structural transitions were identified for $BaCe_{0.9}In_{0.1}O_{3-\delta}$ using x-ray diffraction: orthorhombic – rhombohedral – cubic. There is a strong structural correlation between the rhombohedral and cubic structures observed at high temperatures. The phase transition from the rhombohedral to the cubic structure is not readily visible in the in–situ x-ray diffraction contour plot. However, the pseudo-cubic unit cell axes *a* and *c* of the rhombohedral structure converge towards each other and almost meet at T = 625 °C indicating the formation of the cubic phase at high temperatures. The focus of this discussion has been limited to the high temperature regime as a better understanding of the low temperature regime requires neutron powder

diffraction data.

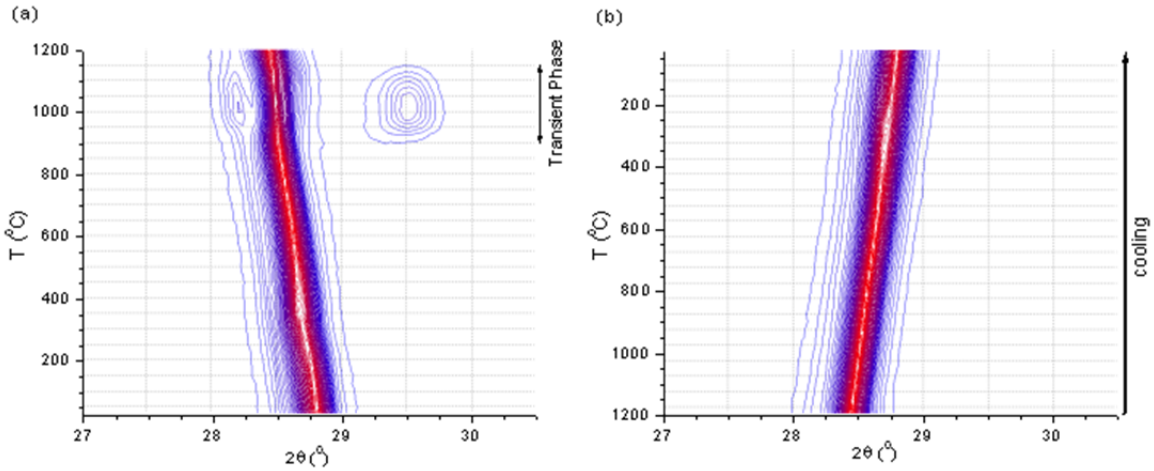

Figure 6.7. In-situ x-ray diffraction contour plot (a) heating and (b) cooling of $BaCe_{0.9}In_{0.1}O_{3-d}$ perovskite in air from 25 to 1200°C. Diffraction peak intensities are shown as constant increment contour from lowest intensity blue to highest intensity red.

Figure 6.7.a shows a novel phase (peak at $2\theta \approx 29.5°$) at T = 900°C. This transient phase is the Ba_2CePtO_6 double perovskite. The features observed at high temperatures can be better described with reference to those observed during the in-situ heating of undoped $BaCeO_3$. Figure 6.8 shows the unit cell evolution of cubic $BaCeO_3$ from 800 to 1200 °C during the in-situ heating of undoped $BaCeO_3$. The linear volume increase is consistent with the thermal expansion of the $BaCeO_3$ cubic phase. No transient phase was observed during this experiment. However the appearance of the transient phase was observed when an identical in-situ experiment was carried out at a later stage. $BaCeO_3$ reacted with the Pt heating filament resulting in the formation of the double perovskite Ba_2CePtO_6 and CeO_2 as shown in Eq. 6.2.

$$2BaCeO_3 + Pt + O_2 \rightarrow Ba_2CePtO_6 + CeO_2 \qquad \text{(Eq. 6.2)}$$

The unreacted $BaCeO_3$ would give a similar unit cell volume evolution to that shown in figure 6.8. At higher temperatures the reverse reaction occurs according to Eq. 6.3.

$$Ba_2CePtO_6 + CeO_2 \rightarrow 2BaCeO_3 + Pt + O_2 \qquad \text{(Eq. 6.3)}$$

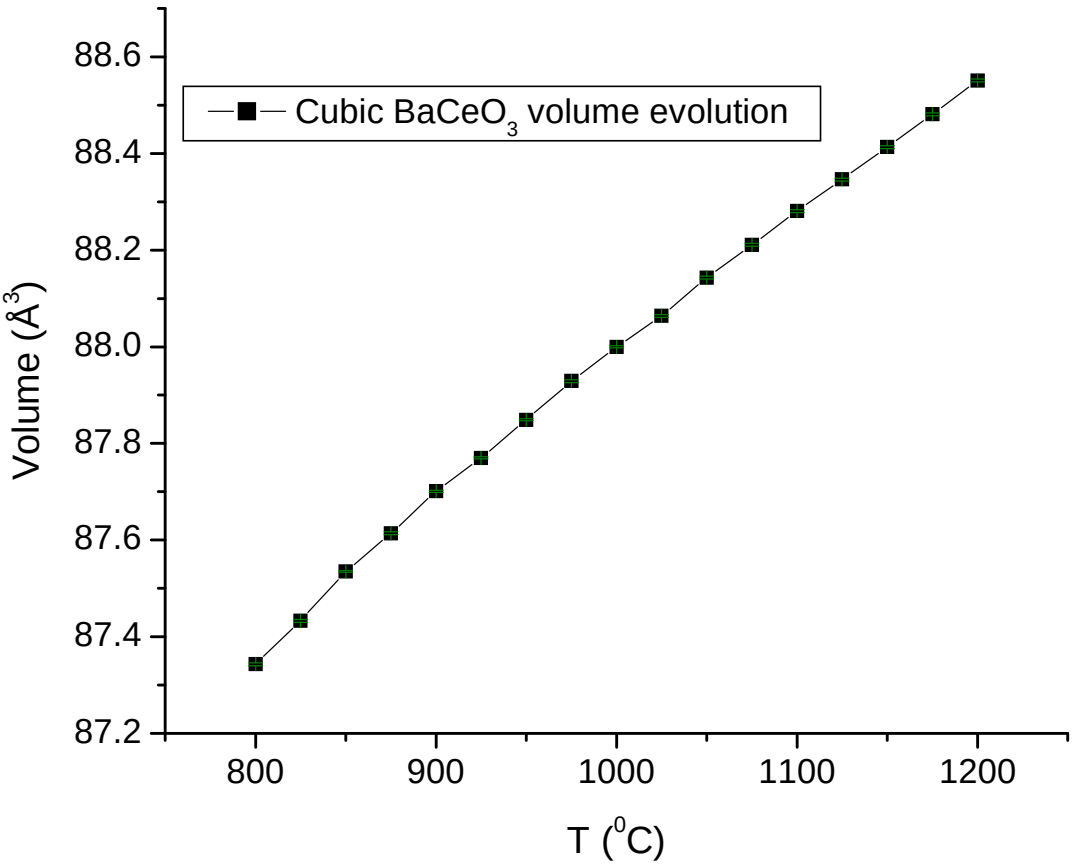

Figure 6.8. Unit cell volume evolution of cubic $BaCeO_3$ from 800 to 1200 °C during the in-situ heating of undoped $BaCeO_3$.

Multi-phase Rietveld refinements were carried out on the diffractograms obtained during the in-situ heating of 10 mol% In-doped $BaCeO_3$ for the temperature range $925 \leq T \leq 1300$ °C. Note that the figure 6.7 contour plot shows diffractograms only up to 1200

°C; further heating up to 1300 °C was carried out after cooling to 800 °C to investigate the reproducibility of the features in the contour plot. The reappearance of the peak at 2θ ≈ 29.5° was observed during the second heating. The Rietveld refinements were conducted for 3 and 4 phases depending on the temperature range as indicated below.

i) 925 ≤ T ≤ 1100 °C: 4 phases, 10 mol% In-doped $BaCeO_3$, CeO_2, Ba_2CePtO_6 and In-enriched $BaCe_{0.9}In_{0.1}O_{3-\delta}$

ii) 1150 ≤ T ≤ 1175 °C: 3 phases, 10 mol% In-doped $BaCeO_3$, CeO_2 and In-enriched $BaCe_{0.9}In_{0.1}O_{3-\delta}$

iii) 1200 ≤ T ≤ 1300 °C: 4 phases, 10 mol% In-doped $BaCeO_3$, CeO_2 , In-enriched $BaCe_{0.9}In_{0.1}O_{3-\delta}$ and In-depleted $BaCe_{0.9}In_{0.1}O_{3-\delta}$

Figure 6.9 shows the unit cell volume evolution of the cubic phases during the in-situ heating of 10 mol% In-doped $BaCeO_3$ in air from 925 to 1300 °C. The red solid circles represent the linear volume expansion of the 10 mol% In-doped $BaCeO_3$. The appearance of the Ba_2CePtO_6 double perovskite phase was observed at 925 °C due to the reaction between the doped $BaCeO_3$ and the Pt heating filament as shown previously in Eq. 6.2. This phase was found to exist up to 1100°C. The diffraction patterns in this temperature range indicated the presence of 4 phases: CeO_2 impurity from the starting material, Ba_2CePtO_6 and two cubic perovskite phases with closely matched unit cell volumes.

The reaction was evident from the diffraction patterns as the phase fractions of both Ba_2CePtO_6 and CeO_2 increased up to 1000 °C and then gradually decreased. The formation of the double perovskite enhanced the local availability of indium in a small

fraction of the sample, stimulating the formation of a second cubic perovskite structure of In-enriched $BaCe_{0.9}In_{0.1}O_{3-\delta}$. As expected, the unit cell volume of this perovskite phase (blue circles) is smaller than the original one (red solid circles) because of the larger indium concentration. The double perovskite phase disappears at T > 1100 °C possibly reverting back to the $BaCeO_3$ perovskite expelling Pt as shown in equation 6.3. Also, we note that the double perovskite phase is not visible during cooling shown as a contour plot in figure 6.7.b. These observations regarding the transient phase Ba_2CePtO_6 double perovskite are consistent with the previous report by Ouchetto, K et al.[144] They observed the appearance and disappearance of the double perovskite phase during the ex-situ annealing of $BaCeO_3$ for several days.

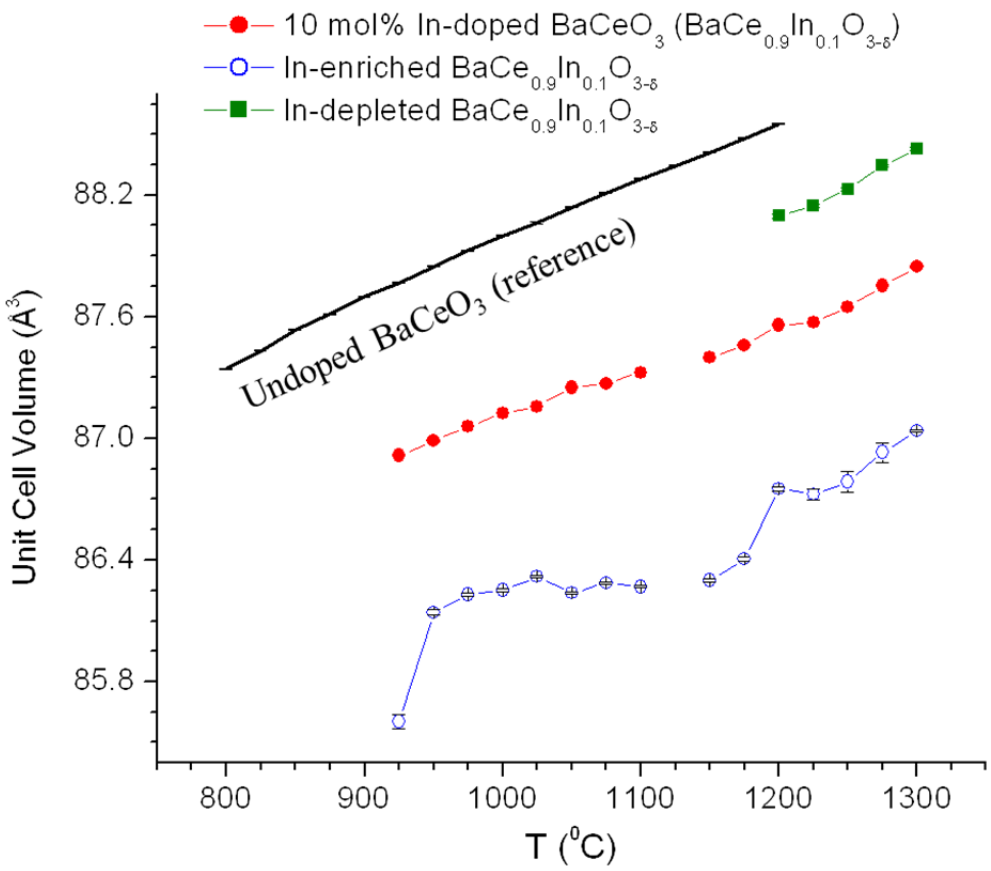

Figure 6.9. Cubic unit cell volume evolution of various phases observed at high temperatures during the heating of 10 mol% In-doped $BaCeO_3$. Red solid circles = nominal 10 mol% In-doped $BaCeO_3$, green solid rectangles = In-depleted $BaCe_{0.9}In_{0.1}O_{3-\delta}$ and blue circles = In-enriched $BaCe_{0.9}In_{0.1}O_{3-\delta}$. The black reference line represents the cubic unit cell evolution of the undoped $BaCeO_3$.

At temperatures between 1200 and 1300 °C, the appearance of an additional cubic perovskite phase was observed. This third perovskite phase appeared to have a larger unit cell volume (green rectangles) in comparison to the 10 mol% indium substituted phase (red solid circles) indicating the In-depletion in the structure. It is important to note that the disappearance of Ba_2CePtO_6 (T = 1150 °C) and the appearance of the In-depleted $BaCe_{0.9}In_{0.1}O_{3-\delta}$ phase (T = 1200 °C) occur within a narrow temperature range. Hence the formation of this In-depleted $BaCe_{0.9}In_{0.1}O_{3-\delta}$ phase is a consequence of the re-

consumption of the $BaCeO_3$ byproduct. These observations are consistent with the thermal expansion of the undoped $BaCeO_3$ cubic perovskite phase shown as a black reference line in figure 6.9. The volume evolution of the cubic $BaCeO_3$ phase with less indium is closer to that of the thermal expansion of the undoped $BaCeO_3$. The volume evolution of the cubic $BaCeO_3$ with more indium is farther to that of the thermal expansion of the undoped $BaCeO_3$.

6.3. Summary & Future Work

The two-step formation pathway for $Ce_{1-x}In_xO_{2-\delta}$ phases through $BaCe_{1-x}In_xO_{3-\delta}$ perovskite intermediate has been discussed in detail. The complex reaction sequences have been studied using in-situ powder x-ray diffraction and this has allowed for a better understanding of the formation pathway as well as the metastable nature of the In-doped CeO_2 fluorite phases. Cubic unit cell parameters obtained via Rietveld refinements of powder x-ray diffraction data of $Ce_{1-x}In_xO_{2-\delta}$ follow the expected trend based on their Shannon ionic radii and illustrate the maximum indium concentration in $Ce_{1-x}In_xO_{2-\delta}$. The indium concentration was also found to control the crystalline domain sizes in $Ce_{1-x}In_xO_{2-\delta}$ and reach a minimum D = 70(15) Å for $x \geq 0.3$. The CO_2 – capture reaction opens up an elegant preparation route for the synthesis of doped fluorite-type phases through ($B'B''$) cation-disordered $Ba(B'_{1-x}B''_x)O_{3-\delta}$ perovskite intermediate precursors. The decomposition of the perovskite phase into $B'_{1-x}B''_xO_{2-\delta}$ and $BaCO_3$ is thermodynamically driven by the formation of $BaCO_3$ in CO_2 and provides access to the metastable $B'_{1-x}B''_xO_{2-\delta}$ phases. An alternate approach for the synthesis of doped fluorite-type phases is to use doped perovskite-type intermediates other than $BaCeO_3$ perovskite based ones. The $SrCeO_3$ perovskite is known and can be considered to substitute $BaCeO_3$ for this purpose.

However, we have seen that the formation of the doped fluorite phases is driven by the formation of $BaCO_3$ in CO_2. The decomposition temperature of $SrCO_3$ is lower than that of $BaCO_3$. Since the stability of $SrCO_3$ is limited, its formation at a lower temperature during the CO_2-capture reaction of $Sr(Ce_{1-x}B''_x)O_{3-\delta}$ perovskite is doubtful. Hence it appears that doped $BaCeO_3$ perovskite is the ideal intermediate for the synthesis of doped fluorite-type phases through CO_2-capture reactions.

Many oxygen deficient $AB^{4+}_{(1-x)}(B')^{3+}_{x}O_{3-\delta}$ perovskites exhibit proton conductivity. At high temperatures, upon exposing to water-containing atmospheres, such a perovskite can absorb water into the structure. If the proton mobility is sufficiently high it can act as a proton conductor. [145] An example is Y_2O_3-doped $BaCeO_3$.[137] The intermediate perovskite precursor In-doped $BaCeO_3$ is a potential proton conductor for solid oxide fuel cells. The structural investigation as a function of temperature is extremely important for any materials that could be used in commercialized devices. Preliminary investigation of the structural phase transition for $BaCe_{0.9}In_{0.1}O_{3-\delta}$ perovskite has been carried out using temperature dependent in-situ powder x-ray diffraction and at least two high temperature structures including a rhombohedral and a cubic structure have been identified. The temperature dependent neutron powder diffractograms have been collected on the high resolution 800-wire diffractometer C2 operated by the National Research Council Canada in Chalk River to probe the structural phase transition for the perovskite $BaCe_{0.9}In_{0.1}O_{3-\delta}$. The data analysis is yet to be carried out; further research regarding this is currently ongoing in the Bieringer group.

Chapter 7: Conclusions

This thesis aims at enhancing insights into structure – reactivity relations for extended solid state systems as illustrated with bixbyite, fluorite and perovskite phases belonging to the vanadate, titanate and cerate families. The majority of studies concerning solid state reaction pathways in the literature are carried out using ex-situ methods. We have demonstrated that in-situ diffraction techniques have developed into a powerful tool for studying solid state reaction pathways, facilitating the controlled synthesis of extended solids. This approach had a substantial impact on identifying most of the metastable materials (limited stability) discussed in this thesis. Correlating defect structures, defect (i.e., oxide) mobility and chemical reactivity provides means to a deeper understanding of functional materials such as solid state ion conductors. This strong correlation was employed throughout this thesis.

The redox reactions presented for the vanadate and titanate systems have provided unprecedented insights into the formation of defects using in-situ methods. This is in stark contrast to the traditional approach of doping, e.g., ZrO_2 with Y_2O_3, at high temperatures where only highly crystalline thermodynamic products are characterized in terms of structure and performance with no insight into defect formation. The oxidative routes presented in this thesis clearly show that defects initially form as clusters and only randomize in the entropic limit after high temperature treatment. The oxidation of $ScTiO_3$ clearly supports this statement through the initial formation of oxide defect clusters at low oxidation temperatures followed by the entropy driven randomization of these defects when exceeding 800 °C. The vanadate system is not able to illustrate the randomization of the oxide defects because of its enhanced oxidative reactivity at

temperatures above 450 °C with the formation of the zircon oxide defect structure. In fact it is the +5 oxidation state that drives the formation of the zircon type phase. Notably $ScVO_{3.5}$ with its oxide defect clusters showed excellent electrical conductivity, whereas $ScTiO_{3.5}$ with randomized defects is a poorly performing oxide ion conductor. This initial finding is further complicated by the strong Ti-O bond which presumably also reduces the ion conductivity in $ScTiO_{3.5}$. Further work is required in order to investigate the contributions of oxide defect clustering on the performance of solid ion conductors.

A substantial portion of this thesis is dedicated to the understanding of structure-reactivity relationships. A generalized oxidation pathway has been established for bixbyite structures with AVO_3 (A = Sc, In) and $ScTiO_3$ as model systems. The two representative ternary oxide systems chosen were found to be excellent candidates for the investigation of the interplay between structure and reactivity. Both the systems showed the first oxidation step to be topotactic in nature. The AVO_3 bixbyites formed $AVO_{3.5+x}$ and $ScTiO_3$ formed $ScTiO_{3.5}$. In the low temperature topotactic regime, the ion movement is confined to the oxide sublattice. Controlling the reactivity and consequently ion mobility in oxygen defect materials is crucial for oxide ion conductors with potential applications in solid oxide fuel cells. The $AVO_{3.5+x}$ defect fluorite structure can tolerate an oxygen stoichiometry ranging from 3.50 to 3.72 corresponding to an oxygen defect concentration range of 12.5% to 7.0%. The features beyond this topotactic regime varied primarily due to the difference in maximum oxidation state possible for vanadium (5+) and titanium (4+). The further oxidation of $ScVO_{3.5+x}$ proceeded through $ScVO_{4-y}$ finally forming fully oxidized $ScVO_4$ zircon. This oxidation step is driven by the tetrahedral site preference for smaller V^{5+}. The topotactic formation of $ScTiO_{3.5}$ was followed by a

complex reaction sequence including phase separation and disorder-order phase transition. The driving force behind the disorder-order phase transition was identified to be the octahedral site preference for Ti^{4+}. A common feature observed for both the systems beyond the topotactic regime is the sufficient mobility of the cations.

The reduction pathway for $ScVO_4$ to $ScVO_3$ did not show any intermediates. The large domain sizes of $ScVO_4$ precursor do not permit fast kinetics. Highly crystalline $ScVO_4$ reduced directly to highly crystalline $ScVO_3$. The formation of $ScVO_{4-y}$ through topotactic reduction of $ScVO_4$ (with smaller particle size) is worth exploring. Sol-gel or co-precipitation reactions can be used to reduce the particle size. The successful synthesis of $ScVO_{4-y}$ defect zircon phase through reduction would greatly enhance the opportunity for the synthesis of oxygen defect phases. Note that only a limited number of $AVO_{3.5+x}$ precursors with the potential of forming AVO_{4-y} are reported in the literature. Compared to this, the number of potential AVO_4 zircon phases reported yet in the literature is plenty. Novel AVO_{4-y} defect zircon phases could be potential photocatalysts for water-splitting as vanadium based zircon phases (e.g., $InVO_4$) have narrow band gaps. One could begin with the synthesis of $InVO_{4-y}$ defect structure by the reduction of appropriate $InVO_4$ precursor (nano-sized). The oxide defect structures could serve as excellent model systems for the systematic investigation of the correlation between concentration of oxide defects and photocatalytic property. Note that, in $ScVO_{4-y}$, the oxide defect concentration can be varied. The oxide defects could act as active sites for photocatalysis. Further studies should be extended to the photocatalytic mechanism of these oxide defect zircon structures.

A true structure – property relationship was established for the AVO_3 systems with the reactivity studies on $ScVO_3$ perovskite. The oxidation of $ScVO_3$ perovskite to $ScVO_4$ zircon is a single step process with no intermediates. Due to the small A cation size, $ScVO_3$ has a smaller tolerance factor of $G_t = 0.8353$ in comparison to the $G_t = 0.8784$ of $LuVO_3$. The synthesis of the perovskite phase was carried out in a targeted fashion through the high pressure route. The high pressure synthesis of the perovskite phase from the bixbyite precursor opens up a new synthetic route for AVO_3 perovskite phases. The opportunity for the synthesis of novel exotic ABO_3 perovskites with smaller A^{3+} cations (e.g., $InVO_3$, $ScTiO_3$) is evident. In addition, the cation ordering observed under high pressure can be extended to the metastable phases including $AVO_{3.5+x}$ for further investigation of structure – reactivity – property relationships.

The traditional approach of doping CeO_2 with In_2O_3 at high temperatures through direct reaction was not successful. This is primarily due to the metastable nature of the In-doped CeO_2 fluorite-type phase as demonstrated with in-situ studies. The successful two-step synthetic approach involved the formation of In-doped $BaCeO_3$ perovskites and subsequent CO_2-capture reaction. The CO_2-capture reaction is an elegant approach for the synthesis of doped fluorite-type phases through appropriate doped perovskite intermediates. The formation of $BaCO_3$ at sufficiently low temperatures during the CO_2-capture reaction is the defining step. The convergence of the formation and decomposition temperatures with increasing In-content limits the maximum value for In-doping for CeO_2 through this method. However, insights into the reaction mechanisms allow us to establish strategies to achieve higher In-concentration in CeO_2 phases. Larger In-concentrations can be achieved by using an intermediate precursor capable of forming

the doped CeO_2 phases at lower temperatures. The research methodology and the insights into the reaction pathways discussed in this thesis can be extended to synthesize other doped CeO_2 phases with potential oxide ion conductivity properties.

The intermediate perovskite precursor In-doped $BaCeO_3$ is a potential proton conductor for solid oxide fuel cells. Preliminary insights into the high temperature behavior of this phase have been provided. The structural investigation as a function of temperature is extremely important for any materials that could be used in commercialized devices. The temperature dependent in-situ powder neutron diffraction data have been collected and further research regarding this is ongoing in the Bieringer research group.

Simple model systems were used for the understanding of structure-reactivity relationship during this work. A variety of interesting observations/challenges including the surface sensitivity during bulk synthesis (for $InVO_{3.5}$) and particle size influence (transition from $AVO_{3.5}$ to AVO_{4-y}) were encountered during this course. Further work should focus on applying the knowledge and research methodologies to other extended structures including layered materials such as Ruddlesden-Popper, Dion-Jacobson and Aurivillius phases. The optimization of synthesis conditions of phase pure higher members (n=2, 3) of layered materials should be more successful through in-situ methods. Further work should focus on the topotactic reduction of these materials which could potentially result in the formation of oxide defect structures with interesting physical properties (e.g., magnetic). Vanadium or manganese based layered materials are good candidates owing to the multiple oxidation states. A systematic study by varying the

reducing atmospheres (reduction potential) will be highly beneficial to the solid state community.

References

1. White, M. A. Properties of materials; Oxford University Press: New York, 1999.

2. Science for Energy Technology: Strengthening the Link between Basic Research and Industry – The Full Report, U.S. Department of Energy, Office of Science, August 2010.

3. New Science for a Secure and Sustainable Energy Future: A Report from the Basic Energy Sciences Advisory Committee, U.S. Department of Energy, December 2008.

4. Vining, C. B. *Nature* **2001**, *413*, 577-578.

5. Nolas, G. S.; Sharp, J.; Goldsmid, H. J. Thermoelectrics: Basic Principles and New Materials Developments; Springer-Verlag: Berlin, 2001.

6. Cox, P. A. Transition Metal Oxides: An Introduction to Their Electronic Structure and Properties; Clarendon Press: Oxford, 1992.

7. Goodenough, J. B. *Prog. Solid State Chem.* **1971**, *5*, 145-399.

8. Rao, C. N. R.; Raveau, B. Transition Metal Oxides: Structure, Properties and Synthesis of Ceramic Oxides; John Wiley & Sons, USA, 1998.

9. Thomas, J. M.; Zamaraev, K. I. (Eds.), Perspectives in Catalysis; Blackwell, Oxford, 1991.

10. Pena, M. A.; Fierro, J. L. G. *Chem. Rev.* **2001**, *101*, 1981-2017.

11. Goodenough, J. B. *Annu. Rev. Mater. Res.* **2003**, *33*, 91-128.

12. Stein, A.; Keller, S. W.; Mallouk, T. E. *Science*, **1993**, *259*, 1558-1564.

13. Goodenough, J. B.; Hong, H. Y. P.; Kafalas, J. A. *Mater. Res. Bull.* **1976**, *11*, 203-220.

14. Gopalakrishnan, J. *Chem. Mater.* **1995**, *7*, 1265-1275.

15. Fister, L.; Johsnson, D. C. *J. Am. Chem. Soc.* **1992**, *114*, 4639-4644.

16. Fukuto, M.; Hornbostel, M. D.; Johsnson, D. C. *J. Am. Chem. Soc.* **1994**, *116*, 9136-9140.

17. Novet, T.; Johsnson, D. C. *J. Am. Chem. Soc.* **1991**, *113*, 3398-3403.

18. Lotgering, F. K. *J. Inorg. Nucl. Chem.* **1959**, *9*, 133-123.

19. Bernal, J. D.; Dasgupta, D. R.; Mackay, A. L. *Clay Miner. Bull.* **1959**, *4*, 15-30.

20. Thomas, J. M. *Phil. Trans. R. Soc. A* **1974**, *277*, 251-287.

21. Rouxel, J.; Tournoux, M. *Solid State Ionics* **1996**, *84*, 141-149.

22. Rüdorff, W. *Chimia* **1965**, *19*, 489-499.

23. Weiss, A.; Ruthardt, R. Z. Naturforsch. **1969**, *24B*, 1056.

24. Dines, M. B. *Science* **1975**, *188*, 1210-1211.

25. Murphy, D.; DiSalvo, F.; Corides, J. N.; Waszczak, J. V. *Mater. Res. Bull.* **1978**, *13*, 1395-1402.

26. Ranmohotti, K. G. S.; Josepha, E.; Choi, J.; Zhang, J.; Wiley, J. B. *Adv. Mater.* **2011**, *23*, 442-460.

27. Dion, M.; Piffard, Y.; Tournoux, M. *J. Inorg. Nucl. Chem.* **1978**, *40*, 917-918.

28. Aikens, L. D.; Li, R. K.; Greaves, C. *Chem. Commun.* **2000**, *21*, 2129-2130.

29. Mizushima, K.; Jones, P. C.; Wiseman, P. J.; Goodenough, J. B. *Mater. Res. Bull.* **1980**, *15*, 783-789.

30. Ménétrier, M.; Saadoune, I.; Levasseur, S.; Delmas, C. *J. Mater. Chem.* **1999**, *9*, 1135-1140.

31. Poeppelmeier, K. R.; Linowicz, M. E.; Scanlon, J. C.; Longo, J. M.; Yelon, W. B. *J. Solid State Chem.* **1982**, *45*, 71-79.

32. Gönen, Z. S.; Paluchowski, D.; Zavalij, P.; Eichhorn, B. W.; Gopalakrishnan, J. *Inorg. Chem.* **2006**, *45*, 8736-8742.

33. Reller, A.; Jefferson, D. A.; Thomas, J. M.; Beyerlein, R. A.; Poeppelmeier, K. R. *Chem. Commun.* **1982**, 24, 1378-1380.

34. Poeppelmeier, K. R.; Lenowicz, M. E.; Longo, J. M. *J. Solid State Chem.* **1982**, *44*, 89-98.

35. Hayward, M. A.; Green, M. A.; Rosseinsky, M. J.; Sloan, J. *J. Am. Chem. Soc.* **1999**, *121*, 8843-8854.

36. Hayward, M. A.; Cusse, E. J.; Claridge, J. B.; Bieringer, M.; Rosseinsky, M. J.; Kiely, C. J.; Blundell, S. J.; Marshall, I. M.; Pratt, F. L. *Science* **2002**, *295*, 1882-1884.

37. Tsujimoto, Y.; Tassel, C. Hayashi, N. Watanabe, T.; Kageyama, H.; Yoshimura, K.; Takano, M.; Ceretti, M.; Ritter, C.; Paulus, W. *Nature* **2007**, *450*, 1062-1065.

38. Well, A. F. Structural Inorganic Chemistry, 5th ed.; Oxford University Press: Oxford, U. K., 1984.

39. Dorogova, M; Navrotsky, A; Boatner, L. A. *J. Solid State Chem.* **2007**, *180*, 847-851.

40. Rapaport, A.; Moteau, O.; Bass, M.; Boatner, L.A.; Deka, C. *J. Opt. Soc. Am. B* **1999**, 16, 911-916.

41. Boatner, L.A.; Beall, G.W.; Abraham, M.M.; Finch, C.B.; Huray, P.G.; Rappaz, M. in: C.J. Northrup (Ed.), Scientific Basis for Nuclear Waste Management; Plenum Press: New York, 1980, p. 289.

42. Wojtowicz, A. J.; Wisniewski, D.; Lempicki, A.; Boatner, L. A. in: J.P.Biersack (Ed.), Radiation Effects and Defects in Solids, vol. 135, Overseas Publishers Association: Amsterdam BV, 1995, p. 305.

43. Fang, Z. M.; Hong, Q.; Zhou, Z. H.; Dai, S. J.; Weng, W. Z.; Wan, H. L. *Catal. Lett.* **1999**, *61*, 39-44.

44. Agunaou, M.; Mernari, B.; Tatibouët, J. M. *Appl. Catal. A* **2000**, *196*, 87-92.

45. Zhang, L.; Fu, H.; Zhang, C.; Zhu, Y. *J. Solid State Chem.* **2006**, *179*, 804-811.

46. Lin, H.-Y., Chen, Y.-F., Chen, Y.-W., *I. J. Hydrogen Energy*, **32**, (2007), 86-92.

47. Aoki, Y.; Konno, H. *J. Mater. Chem.* **2001**, *11*, 1458-1464.

48. Chakoumakos, B. C.; Abraham, M. M.; Boatner, L. A. *J. Solid State Chem.* **1994**, *109*, 197-202.

49. Wang. Y, Cao. G, *J. Mater. Chem.*, **17**, (2007), 894-899.

50. Touboul, M.; Toledano, P. *Acta Crystallogr., Sect. B: Struct. Crystallogr. Cryst. Chem.* **1980**, *36*, 240-245.

51. Touboul, M.; Melghit, K.; Beńard, P.; Louer, D. *J. Solid State Chem.* **1995**, *118*, 93-98.

52. Denis, S.; Baudrin, E. ; Touboul, M. ; Tarascon, J.-M. *J. Electrochem. Soc.*, **144**, (1997), 4099-4109.

53. Oshikiri, M.; Seitsonen, A. P.; Parrinello, M.; Boero, M.; Ye, J.; Zou, Z. *Mat. Res. Soc. Symp. Proc.* **2002**, *730*, 137-142.

54. Zou, Z. ; Ye, J.; Sayama, K.; Arakawa, H. *Nature* **2001**, *414*, 625-627.

55. Ye, J.; Zou, Z. ; Arakawa, H.; Oshikiri, M. ; Shimoda, M. ; Matsushita, A. ; Shishido, T. *J. Photochem. Photobiol. A: Chem.*, 2002 *148*, 79-83.

56. Ge, L.; Xu, M. ; Fang, H. *J. Mol. Catal. A: Chem*. **2006,** *258*, 68-76

57. Orel, B.; Vuk, A. S.; Krašovec, U. O.; Dražič, G. *Electrochim. Acta* **2001**, *46*, 2059-2068.

58. Nguyn, H. C.; Goodenough, J. B. *Phys. Rev. B* **1995**, *52*, 324-334.

59. Mizokawa, T.; Khomskii, D. I.; Sawatzky, G. A. *Phys. Rev. B* **1999,** *60*, 7309-7313.

60. Ren, Y.; Palstra, T.T. M.; Khomskii, D.I.; Pellegrin, E.; Nugroho, A. A.; Menovsky, A. A.; Sawatzky, G.A. *Nature*, **1998**, *396*, 441-444.

61. Miyasaka, S.; Okimoto, Y.; Iwama, M.; Tokura, Y. *Phys. Rev. B.***2003**, *68*, 100406/1-100406/4.

62. Yan, J. -Q.; Zhou, J. -S.; Goodenough , J. B. *Phys. Rev. B.***2005**, *72*, 094412/1-094412/6.

63. Megaw, H. D. *Proc. Phys. Soc.* **1946,** 58, 133-152.

64. Woodward, P. M. *Acta Cryst.* **1997**, B53, 32-43.

65. Goldschmidt, V. M. *Die Gesetze der Krystallochemie.* **1926**, 14, 477-485.

66. Randall, C. A.; Bhalla, A. S.; Shrout, T. R.; Cross, L. E. *J. Mater. Res.* **1990**, *5*, 829-834.

67. Shirane, G.; Danner, H.; Pepinski, R. *Phys. Rev.* **1957**, *105*, 856-860.

68. Reid, A. F.; Sienko, M. J. *Inorg. Chem.* **1967**, *6*, 521-524.

69. Alonso, J. A.; Casais, M. T.; Martinez-Lope, M. J. *Dalton Trans.* **2004**, *9*, 1294-1297.

70. Lundgren, R. J.; Cranswick, L. M. D.; Bieringer, M. *J. Solid State Chem.* **2006**, *179*, 3599-3606.

71. Virkar, A. N.; Maiti, H. S. *J. Power Sources* **1985**, *14*, 295-303.

72. Knight, K. S. *Solid State Ionics* **2001**, *145*, 275-294.

73. Knight, K. S. *Solid State Ionics* **1994**, *74*, 109-117.

74. Hofmann, P. Solid State Physics: an introduction; WILEY-VCH Verlag GmbH & Co. KGaA: Weinham, 2008.

75. Pecharsky, V. K.; Zavalij, P. Y. Fundamentals of Powder Diffraction and Structural Characterization of Materials; Springer: New York, 2005.

76. Furree, A.; Mesot, J.; Strässle, T. Neutron Scattering in Condensed Matter Physics; World Scientific: Singapore, 2009.

77. Bacon, G. E. Neutron Diffraction; Clarendon: Oxford, 1975.

78. Caglioti, G.; Paoletti, A.; Ricci, F. P. *Nucl. Instrum.* **1958**, *3*, 223.

79. Brown, I. D. *Acta Cryst.* **1992**, *B48*, 553-572.

80. O'Keeffe, M. *Structure and Bonding*, **1989**, *71*, 161-190.

81. Brown, I. D.; Altermatt, D. *Acta Cryst.* **1985**, *B41*, 244-247.

82. Wills, A. S. VaList, UCL London, 1998-2010, Program available from www.ccp14.ac.uk

83. Salinaz-Sanchez, A.; Garcia-Monoz, J. L.; Rodrigues-Carvajal, J.; Saez-Puche, R. *J. Solid State Chem.* **1992**, *100*, 201-211.

84. Skowron, A.; Brown, I. D. *Acta Cryst.* **1990**, *C46*, 527-531.

85. West, A. R. Basic Solid State Chemistry, 2nd Ed.; John Wiley & Sons Ltd: UK, 1999.

86. Smart, J. S. Effective Field Theories of Magnetism; Saunders: Philadelphia, 1966.

87. Mabbs, F. E.; Machin, D. J. Magnetism and Transition Metal Complexes; Chapman and Hall, 1973.

88. Goodenough, J. B. Magnetism and Chemical Bond; Interscience: New York, 1963.

89. Kramers, H. A. *Physica* **1934**, *1*, 182-192.

90. Kanamori, J. *J. Phys. Chem. Solids* **1959**, *10*, 87-98.

91. Zener, C. *Phys. Rev.* **1951**, *81*, 440-444.

92. Zener, C. *Phys. Rev.* **1951**, *82*, 403-405.

93. de Gennes, P. G. *Phys. Rev.* **1960**, *118*, 141-154.

94. Anderson, P. W. *Phys. Rev.* **1950**, *79*, 350-356.

95. Anderson, P. W. *Phys. Rev.* **1959**, *115*, 2-13.

96. Giaquinta, D. M.; zur Loye, H.-C. *Chem. Mater.* **1994**, *6*, 365 – 372.

97. Shafi, S. P.; Lundgren, R. J.; Cranswick, L. M. D.; Bieringer, M. *J. Solid State Chem.* **2007**, *180*, 3333-3340.

98. Shafi, S. P.; Kotyk, M. W.; Cranswick, L. M. D.; Michaelis, V. K.; Kroeker, S.; Bieringer, M. *Inorg. Chem.* **2009**, *48*, 10553-10559.

99. Kim, N.; Hsieh, C.-H.; Stebbins, J. F. *Chem. Mater.* **2006**, *18*, 3855-3859.

100. Bhalla, A. S.; Guo, R.; Roy, R. *Mater. Res. Innovations.* **2000**, *4*, 3-26.

101. Stolen, S.; Bakken, E.; Mohn, C. E. *Phys. Chem. Chem. Phys.* **2006**, *8*, 429-447.

102. Woodward, P. M. *Acta Crystallogr., B* **1997**, *53*, 44-66 and references therein.

103. Goodenough, J. B. *Reports on Progress in Physics* **2004**, *67*, 1915-1993.

104. Ren, Y.; Nugroho, A. A.; Menovsky, A. A.; Strempfer, J.; Rütt, U.; Iga, F.; Takabatake, T.; Kimball, C. W. *Phys. Rev. B* **2003**, *67*, 014107/1-014107/6.

105. Muñoz, A.; Alonso, J. A.; Casais, M. T.; Martinez-Lope, M. J.; Martinez, J. L.; Fernández-Diaz, M. T. *Chem. Mater.* **2004**, *16*, 1544-1550.

106. Lundgren, R. J.; Cranswick, L. M. D.; Bieringer, M. *Chem. Mater.* **2007**, *19*, 3945-3955.

107. Castillo-Martinez, E.; Bieringer, M.; Shafi, S. P.; Cranswick, L. M. D.; Alario-Franco, M. A. *J. Am. Chem. Soc.* **2011**, *133*, 8552-8563.

108. Lin, J. F.; Degtyareva, O.; Prewitt, C. T.; Dera, P.; Sata, N.; Gregoryanz, E.; Mao, H. K.; Hemley, R. J. *Nat. Mater.* **2004**, *3*, 389-393.

109. Oganov, A. R.; Ono, S. *Proc. Nat. Acad. Sci.* **2005**, *102*, 10828-10831.

110. Pasternak, M. P.; Rozenberg, G. K.; Machavariani, G. Y.; Naaman, O.; Taylor, R. D.; Jeanloz, R. *Phys. Rev. Lett.* **1999**, *82*, 4663-4666.

111. Olsen, J. S.; Cousins, C. S. G.; Gerward, L.; Jhans, H.; Shelson, B. J. *Phys. Scr.* **1991**, *43*, 327-330.

112. Ono, S.; Ohishi, Y. *J. Phys. Chem. Solids* **2005**, *66*, 1714-1720.

113. Kolitsch, U.; Tillmanns, E. *Acta Cryst.* **2003**, *E59*, i36-i39.

114. Rice, C. E.; Robinson, W. R. *J. Solid State Chem.* **1977**, *21*, 155-160.

115. Rossell, H. J. *J. Solid State Chem.* **1976**, *19*, 103-111.

116. Lyashenko, L. P.; Shcherbakova, L. G.; Belov, D. A.; Knotko, A. V. *Inorg. Mater.* **2009**, *45*, 543-549.

117. Pokrovskii, B.; Isaeva. E. V. *Zhurnal Neorganicheskoi Khimii* **1977**, *22*, 2035-2049.

118. Knop, O.; Brisse, F.; Castelliz, L. *Can. J. Chem.* **1969**, *47*, 971-990.

119. Brixner, L. H. *Inorg. Chem.* **1964**, *3*, 1065-1067.

120. Komissarova, L. N.; Shatskii, V. M. *Zhurnal Prikladnoi Khimii* **1966**, *39*, 2211-2216.

121. Shafi, S. P.; Hernden, B. C.; Cranswick, L. M. D.; Hansen, T. C.; Bieringer, M. *Inorg. Chem.* **2012**, *51*, 1269-1277.

122. Goodenough, J. B. *Nature* **2000**, *404*, 821.

123. Weber, A.; Tiffee, E. I. *J. Power Sources* **2004**, *127*, 272-283.

124. Kharton, V. V.; Marques, F. M. B.; Atkinson, A. *Solid State Ionics* **2004**, *174*, 135-149.

125. Wincewicz, K. C.; Cooper, J. S. *J. Power Sources* **2005**; *140*, 280-296.

126. Fergus, J. W. *J. Power Sources* **2006**, *162*, 30-40.

127. Lashtabeg, A.; Skinner, S. J. *J. Mater. Chem*. **2006**, *16*, 3161-3170.

128. Steele, B. C. H. *Solid State Ionics* **2000**, *129*, 95-110.

129. Huang, W.; Shuk, P.; Greenblatt, M. *Chem. Mater*. **1997**, *9*, 2240-2245.

130. Huang, W.; Greenblatt, M. *Solid State Ionics* **1997**, *100*, 23-27.

131. Huang, K.; Feng, M.; Goodenough, J. B. *J. Am. Ceram. Soc*. **1998**, *81*, 357-362.

132. Eguchi, K. *J. Alloys and Compounds* **1997,** *250*, 486-491.

133. Eguchi, K.; Setoguchi, T.; Inoue, T.; Arai, H. *Solid State Ionics* **1992**, *52*, 165-172.

134. Yahiro, H.; Eguchi, Y.; Eguchi, K.; Arai, H. *J. Applied Electrochemistry*. **1988**, *18*, 527-531.

135. Matsui, T.; Inaba, M.; Mineshige, A.; Ogumi, Z. *Solid State Ionics* **2005**, *176*, 647-654.

136. Kilner, J. A.; Waters, C. D. *Solid State Ionics* **1982**, *6*, 252-259.

137. Sneha, B. R.; Thangadurai, V. *J. Solid State Chem*. **2007**, *180*, 2661-2669.

138. Trobec, F.; Thangadurai,V. *Inorg. Chem.* **2008**, *47*, 8972-8984.

139. Pearce, M. C.; Thangadurai, V. *Asia-Pac. J. Chem. Eng.* **2009***, 4*, 33–44.

140. Gerlach, R. G.; Bhella, S. S.; Thangadurai, V. *Inorg. Chem.* **2009**, *48*, 257-266.

141. Shannon, R. D. *Acta Cryst*. **1976**, *A32*, 751-767.

142. Bhella, S.S.; Shafi, S. P.; Trobec, F.; Bieringer, M.; Thangadurai, V. *Inorg. Chem.* **2010**, *49*, 1699-1704.

143. Lussier, J. Structure Evolution of Cerium (IV) Perovskites, University of Manitoba, April 2012.

144. Ouchetto, K.; Archaimbault, F.; Pineau, A.; Choisnet, J. *J. Mater. Sci. Lett.* **1991**, *10*, 1277-1279.

145. Patnaik, A. S.; Virkar, A. V. *J. Electrochem. Soc.* **2006**, *153*, A1397-A1405.